

University of Alabama in Huntsville

LOUIS

Dissertations

UAH Electronic Theses and Dissertations

2019

Solar energetic particles transport in meandering magnetic field

Ashraf Moradi

Follow this and additional works at: <https://louis.uah.edu/uah-dissertations>

Recommended Citation

Moradi, Ashraf, "Solar energetic particles transport in meandering magnetic field" (2019). *Dissertations*. 388.

<https://louis.uah.edu/uah-dissertations/388>

This Dissertation is brought to you for free and open access by the UAH Electronic Theses and Dissertations at LOUIS. It has been accepted for inclusion in Dissertations by an authorized administrator of LOUIS.

**SOLAR ENERGETIC PARTICLES TRANSPORT IN
MEANDERING MAGNETIC FIELD**

by

ASHRAF MORADI

A DISSERTATION

Submitted in partial fulfillment of the requirements
for the degree of Doctor of Philosophy
in
The Department of Space Science
to
The School of Graduate Studies
of
The University of Alabama in Huntsville

HUNTSVILLE, ALABAMA

2019

In presenting this dissertation in partial fulfillment of the requirements for a doctoral degree from The University of Alabama in Huntsville, I agree that the Library of this University shall make it freely available for inspection. I further agree that permission for extensive copying for scholarly purposes may be granted by my advisor or, in his/her absence, by the Chair of the Department or the Dean of the School of Graduate Studies. It is also understood that due recognition shall be given to me and to The University of Alabama in Huntsville in any scholarly use which may be made of any material in this dissertation.

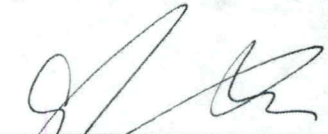
Ashraf Moradi
Ashraf Moradi

11.05.2019
(date)

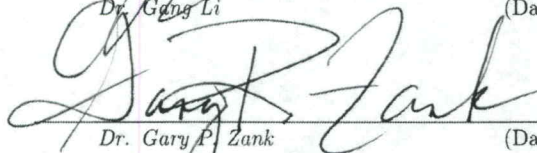
DISSERTATION APPROVAL FORM

Submitted by Ashraf Moradi in partial fulfillment of the requirements for the degree of Doctor of Philosophy in Space Science and accepted on behalf of the Faculty of the School of Graduate Studies by the dissertation committee.

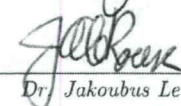
We, the undersigned members of the Graduate Faculty of The University of Alabama in Huntsville, certify that we have advised and/or supervised the candidate of the work described in this dissertation. We further certify that we have reviewed the dissertation manuscript and approve it in partial fulfillment of the requirements for the degree of Doctor of Philosophy in Space Science.



Dr. Gang Li 11/05/2019 Committee Chair
(Date)




Dr. Gary P. Zank 11/5/19
(Date)



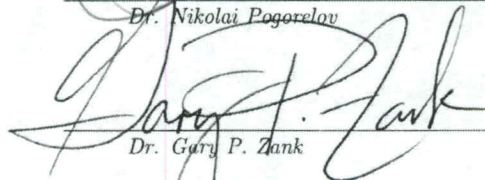
Dr. Jakoubus Le Roux 11/05/2019
(Date)



Dr. Qiang Hu 11/05/2019
(Date)



Dr. Nikolai Pogorelov 11/05/2019
(Date)



Dr. Gary P. Zank 11/5/19 Department Chair
(Date)



Dr. John Christy 11/6/19 College Dean
(Date)



Dr. David Berkowitz 11/12/19 Graduate Dean
(Date)

ABSTRACT


School of Graduate Studies
The University of Alabama in Huntsville

Degree Doctor of Philosophy College/Dept. Science/Space Science
Name of Candidate Ashraf Moradi
Title Solar Energetic Particles Transport in Meandering Interplanetary Magnetic Field

The transport of solar energetic particles (SEPs) in a meandering interplanetary magnetic field (IMF) is investigated in the scatter-free regime. The IMF in average has a Parker spiral shape. However, it can deviate from the Parker field due to fluctuating flows at the source surface. We adopt a meandering magnetic field from the Giacalone 2001 model in which a single parameter V_{rms} is used to characterize how the interplanetary magnetic field deviates from the Parker field. The trajectories of energetic protons and electrons are followed in this meandering field using test particle simulations. Ten thousand particles are injected in the ecliptic plane and the path length distributions are obtained at several distances, 0.2 to 3.0 AU from the Sun for various V_{rms} (from 0.3 to 2.5 km/s). By generating ten thousand different realizations of the meandering field line, we also obtain the path length distribution of the field lines. We introduce four models for the meandering interplanetary magnetic field with various V_{rms} on the source surface. In all models, the properties of the IMF and trajectories of the particles are investigated. Our simulations show that particles can jump to the adjacent magnetic field line regularly and are not tied to a single field line. We also show that the path length distributions of the particles and

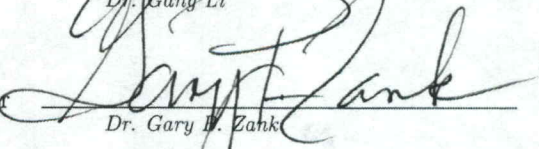
that of the field lines are different and the difference increases as V_{rms} increases. Our results can be compared to the observations of ACE, WIND and Ulysses spacecraft to set constraints on V_{rms} . We calculate both the longitudinal and latitudinal displacements from the source when particles arrive at 1 AU. This provides some basis for understanding simultaneous observations of impulsive events made at multiple spacecraft.

Abstract Approval: Committee Chair




Dr. Gang Li

Department Chair



Dr. Gary E. Zank

Graduate Dean



Dr. David Berkowitz

ACKNOWLEDGMENTS

I would like first acknowledge God, because, without His love, none of this would be possible. During this journey, many people helped me and gave me strength to follow my dream and pursue my degree. I am thankful for all the support I got during my long journey. I would like to express my deepest gratitude to my adviser, Professor Gang Li, for his patience, support over the years. Without his guidance, patience, and persistent help, this dissertation would not be possible.

I would like to thank my committee members, Professor G. P. Zank, Professor N. Pogorelov, Dr. Le Roux, and Dr. Q. Hu for their support and encouragement. I have a high respect for every one of them. I am also thankful for the support of Dr. J. Heerikhuisen and Dr. V. Florinski for valuable advices in parallel computing. I also would like to thank Dr. P. Bitzer for his valuable computing advices.

I deeply appreciate the love and support of my parents who made this PhD possible. I also thank Nooshin Moradi, Christine Howard, Celia, Azadeh Ashoori, Soudabeh Karegar, Leila Nourazar, Hamideh Salehi, Farzaneh Hazrati, Doga Ozturk, Zivar Hallaji, Mojgan Setayesh, Nasrin Salehi, Stephanie and Alan Taylor, Jerusha Emmanuel and Sussan Einakian for their friendship and help through this journey. I am extremely thankful for my teacher, I owe my life to him. I also thank my siblings for their love and support. God bless each and every one of you.

TABLE OF CONTENTS

	PAGE
List of Figures	xi
List of Tables	xviii
List of Symbols	xix
Chapter	
1 Introduction	1
1.1 The solar atmosphere	1
1.1.1 Photosphere	1
1.1.2 Chromosphere	1
1.1.3 The transition region	2
1.1.4 Corona	2
1.1.5 Solar wind	2
1.2 Surface flows on the photosphere	3
1.2.1 Small-scale photospheric flows	3
1.2.1.1 Granules	3
1.2.2 Large-scale surface flows	4
1.2.2.1 Mesogranules	4
1.2.2.2 Supergranules	5

1.2.2.3	Giant Cells	6
1.2.2.4	Meriodinal Flows	7
1.2.3	Differential Rotation	7
1.3	Magnetic field	7
1.3.1	Interplanetary Magnetic Field - IMF	8
1.3.1.1	Parker Spiral	17
1.3.2	The Effect of Surface Flows in the IMF, Large scale Turbulence	19
1.4	Solar Energetic Particles - SEPs	21
1.5	Single Particle Motion	22
1.6	Simulation of test particles	23
1.6.0.1	Boris Particle Tracking Method	23
1.6.0.2	Wirz's Method or Modified Boris Method	24
2	Preliminary Results	27
2.1	Propagation of solar energetic particles in the Parker field	27
2.1.1	Parker Spiral	27
2.1.2	Trajectory of solar energetic particles in Parker magnetic field	29
2.2	Fluctuating magnetic field based on Granular flows	30
3	Giacalone's Model for Interplanetary Magnetic Field	36
3.1	Introduction	36
3.2	Model Description	39
3.2.1	Interplanetary Magnetic Field	39
3.2.2	Simulation of test particles	42

3.3	Results and Discussion	43
3.3.1	Flow pattern on the source surface	43
3.3.2	Magnetic Field	44
3.3.3	Trajectory of Electrons	45
3.3.4	Footpoint's trajectory on the source surface	45
3.3.5	Path Length Distributions	46
3.3.5.1	Path length distribution of electrons in Parker field	46
3.3.5.2	Path length distribution of electrons in the meandering field	47
3.3.6	Angular Displacement of electrons	59
3.4	Conclusion	60
4	Hathaway's Model	78
4.1	Introduction	78
4.2	Model Description	79
4.3	Results and Discussion	86
4.3.1	Flow Pattern on the source surface	86
4.3.2	Footpoint motion on the source surface	87
4.3.3	Interplanetary Magnetic Field	90
4.3.4	Trajectory of solar energetic protons	92
4.3.5	Conclusion	94
5	Meandering Magnetic field developed from the expansion of open magnetic flux tubes emerging from the borders of the supergranules	104

5.1	Extrapolating the borders of the supergranules to the surface	105
5.1.1	Model	105
5.1.2	Results and Discussion	111
5.1.2.1	Flow pattern on the source surface	111
5.1.2.2	Footpoint motion on the source surface	111
5.1.3	Interplanetary Magnetic Field	113
5.1.3.1	Trajectory of the solar energetic protons	117
5.1.3.2	Conclusion	117
5.2	Adding memory to the footpoints motion	118
5.2.1	Model Description	118
5.2.2	Results and Discussion	121
5.2.2.1	Footpoints motion on the source surface	121
5.2.2.2	Interplanetary Magnetic Field	124
5.2.3	Conclusion	126
5.3	Comparison of all three models of footpoint motion	127
6	Conclusion	130

LIST OF FIGURES

FIGURE	PAGE
1.1 (a) Granule cells, (b) convective flows inside granules.	4
1.2 (a) Supergranule cells, (b) giant cells, (c) Meridional flows (d) differential rotation.	5
1.3 Parker Spiral, Marsh 2013	18
1.4 The dynamic of Parker spiral	19
1.5 Random walk of footpoint	20
1.6 Boris Method	24
1.7 Wirz Method	25
2.1 The Parker magnetic field line as dragged out by the radial solar wind.	28
2.2 (a) XY and (b) XZ projection of four Parker spiral line that originated from latitude 45° . Colors represents the field lines that emerged from the footpoints at the same latitude 45° and multiple longitudes. The dashed lines in (b) show the locus of same latitude, 45°	32
2.3 The (a) XY and (b) XZ projection of final position of a thousand 100 MeV protons which are injected in the area of latitude $(-4^\circ, 4^\circ)$ and longitude $(-4^\circ, 4^\circ)$ on the source surface. The green solid lines are the Parker field lines originated from the borders of injection area. The light green line is the Parker field line emerge from the center of injection area.	33
2.4 The same as Figure 2.3 for 100 MeV electrons. The travel time is 5 hours.	34
2.5 3D plot of a single magnetic field in (a) latitude 45° and (b) ecliptic plane. The red solid line shows the meandering field and the blue solid line is the Parker field line from the same starting point.	35

3.1	The source surface flows (a) V_θ , (b) V_ϕ and (c) $V_g = \sqrt{V_\theta^2 + V_\phi^2}$. Color bar for panels (a) and (b) are from -1000 to 1000 m/s. Color bar for panel (c) is from 0 to 1400 m/s. $V_{rms} = 0.6$ km/s, $T_c = 2$ days and $N = 50$	62
3.2	The vector surface flow map. The arrows show the flow direction. And the color bar shows the magnitude of the speed. $V_{rms} = 0.6$ km/s, $T_c = 2$ days and $N = 50$	63
3.3	The meandering magnetic field lines in the Giacalone (2001) model. $V_{rms} = 0.6$ km/s, $T_c = 2$ days and $N = 50$. Solid lines are the meandering field lines and dashed lines are the Parker field lines. Panel (a) and (b) are projections in the XY, and XZ planes when the field lines are traced to $R = 10$ AU; Panels (c) and (d) are close ups of (a) and (b) where the field lines are only traced to $R = 1$ AU. In all figures, the same color field lines (Parker or the meandering field lines) start from the same locations.	64
3.4	Two examples of electron trajectories in the meandering field. (a) and (d): trajectories in 3D, (b) and (e): projection of the trajectories in the XY plane; (c) and (f): projection of the trajectories in the XZ plane. In all panels, the solid Red lines are the electrons trajectories; the dashed green lines are the Parker field lines the electrons initially tie to; and the dashed blue lines are the Parker field lines the electrons tie to at 1 AU. $V_{rms} = 0.6$ km/s, $T_c = 2$ days and $N = 50$. The angular displacement between the initial and the final Parker field lines are $\sim 10^\circ$	65
3.5	The footpoint trajectory of two electrons from two different starting points, multi-colored solid line. The color bar is corresponding to the surface flow vectors magnitude. Purple in the solid line is the footpoint at $t = 0$ sec and red is the footpoint at the end of the trajectory.	66
3.6	Histogram of path length distribution of $10,000$ electrons in a Parker field. $V_{SW} = 400$ km/s is assumed. The path length of Parker field is 1.163 AU, shown here as the blue vertical line, which represent a δ -function type distribution. The Red lines show the electron path lengths. It has a small range from slightly smaller than 1.163 AU to 1.170 AU. This small range is due to curvature drift and difference in initial pitch angle. The y-axis unit is arbitrary.	67

3.7	Histogram of path length distribution of 10,000 electrons in a meandering field for three different kinetic energy, 1, 10 and 100 MeV at 1 AU. The blue, red and green lines are path length distributions of 1, 10, 100 MeV electrons, respectively. The rms speed of fluctuations are chosen as Giacalone (2001), $V_{rms} = 0.6$ km/s. Note that in this figure source surface is put at 10 solar radii.	68
3.8	Path length distributions for both the field line (in blue) and electrons (in red) when $R = 0.2$ AU: (a) $V_{rms} = 0.3$ km/s, (b) $V_{rms} = 0.6$ km/s, (c) $V_{rms} = 1.0$ km/s, (d) $V_{rms} = 2.5$ km/s. The curves are fitted by a Gaussian functional form.	69
3.9	Same as Figure 3.8 but for $R = 1$ AU	70
3.10	Path length distributions for both the field line (in blue) and electrons (in red) when $R = 0.2$ AU: (a) $V_{rms} = 0.3km/s$, (b) $V_{rms} = 0.6km/s$, (c) $V_{rms} = 1.0km/s$, (d) $V_{rms} = 1.5km/s$, (e) $V_{rms} = 2.0km/s$, (f) $V_{rms} = 2.5km/s$. The curves are fitted by a Gaussian functional form and shown in the legends are the p -value obtained from the Shapiro-Wilk test. Distributions with p -values higher than 0.05 are Gaussian.	71
3.11	Same as Figure 3.10, but for $R = 0.5$ AU.	72
3.12	Same as Figure 3.10, but for $R = 1.0$ AU.	73
3.13	Same as Figure 3.10, but for $R = 2.0$ AU.	74
3.14	Same as Figure 3.10, but for $R = 3.0$ AU.	75
3.15	The distribution of the angular displacement of electron in Parker field.	76
3.16	Same as Figure 3.15, but for electrons in meandering fields. (a) $R = 0.2$, (b) $R = 0.5$, (c) $R = 1.0$, (d) $R = 2.0$, (e) $R = 3.0$ AU. Example of electron trajectories are shown in Figure 3.4.	77
4.1	The power spectrum of (a) the observed by MDI data, (b) the simulated power spectrum by the extracted spectral coefficients.	82
4.2	The Doppler image of the line of sight. Right: The simulated Doppler image from updated spectral coefficients. Left: The observed Doppler image by MDI, Hathaway et al. (2010)	83
4.3	(a) V_{θ}	87

4.3	(b) V_ϕ	88
4.3	(c) V_g . The magnitude of the horizontal velocities on the source surface: (a) V_θ , (b) V_ϕ and (c) $V_g = \sqrt{V_\theta^2 + V_\phi^2}$. The color bar for panel (a) and (b) are from -500 to 500 m/s and 0 to 1000 m/s for panel (c). . .	89
4.4	The random walk of the footpoints in Hathaway in (a) latitude 45° and (b) ecliptic plane. Different colors are corresponding to different longitudes that are rotated to start from $\phi = 0$	95
4.5	(a)	96
4.5	(b)	96
4.5	(c)	97
4.5	(d)	97
4.5	The meandering magnetic field lines obtained by adopting the Hath- away 2016 velocity spectrum. The field lines are followed from the source surface to 6 AU in panel (a) and (b) and 15 AU in panel (c) and (d). In panel (a) and (c), the field lines start from latitude 45° and in panel (b) and (d) from the ecliptic plane. Solid lines are the meandering field lines. In panel (a) and (b), the dashed lines are the Parker field lines originated from the same starting point of the same color meandering field line. In Panel (c) and (d), all magnetic field lines are rotated azimuthally to start from the $\phi = 0$ and the green dashed line is the Parker field line starts from $\phi = 0$	97
4.6	$\psi = \frac{B_\phi}{B_r}$ in GSE coordinates, Li et al. (2016).	98
4.7	Sunspot activity from 1996 - 2010. 2000 is the solar maximum and 2009 is the solar minimum. Xu et al. (2015)	98
4.8	The histogram of the ψ , the angle between the B_r and B_ϕ in GSE co- ordinates at the ecliptic plane at 1 AU: (a) Simulated by Hathaway's Model. The blue is the ψ angle of the meandering field and the green corresponds to Parker. (b) The one-second average data solar maxi- mum from ACE spacecraft for cycle January 22 to February 17 of 2000 (c) The one-second average data solar minimum from ACE spacecraft for cycle January 1 to January 27, 2009. Solar wind velocity in (a) is chosen to be 500 km/s.	99
4.9	(a)	100

4.9	(b)	100
4.9	(c)	101
4.9	(d)	101
4.9	Two examples of the 100 MeV protons 3D trajectories in the meandering magnetic field in latitude 45, panel (a) and (b), and ecliptic plane, panel (c) and (d). The protons are followed for 4 days. The red solid line is the trajectory of the solar energetic protons and the green dashed line is the original Parker field line.	101
4.10	The variation of the cosine of pitch angle, μ , in 25 minutes, panel (a) and (b), and 2 hours, panel (c) and (d). The proton in (a) and (c) is injected in latitude 45 and the proton in (b) and (d) is injected in the ecliptic plane. The red line is the cosine of pitch angle w.r.t. to the local meandering field and the blue line is w.r.t. the local Parker field.	102
4.11	The variation of the kinetic energy of two individual protons in a meandering field for 4 days. The top panel is injected at latitude 45 and bottom panel in the ecliptic plane. The initial energy 100 MeV.	103
5.1	The open magnetic field lines coming from the boundaries of supergranules only, Judge (2006)	105
5.2	The horizontal flow velocity map, $V_g = \text{sqrt}(V_\theta^2 + V_\phi^2)$, on the photosphere. The color bar is changed to show estimated boundaries of the supergranules. The dark blue areas can be considered as the borders of supergranules or magnetic concentrations on the surface of the photosphere.	107
5.3	Comparison of the (b) simulated supergranule boundaries to (a) observed magnetic flux tube concentration on the supergranules border. The color bars on the left side of (b) and (c) show the magnitude of V_g . The dark blue areas present supergranules boundaries. (c) zoomed in on the of the border on the left bottom of (b). (d) shows the flow velocity direction on the border. The colors of the vectors present the magnitude of V_g . The resolution of the simulated maps is 0.001° .	108
5.4	A zoomed-in image of Figure 5.3. The dark blue areas can be regarded as the supergranules boundaries. The black circles are the typical size of the supergranules. The figure is not to scale.	109

5.5	The average minimum number and maximum number of the grid points that are located on top of the supergranules boundaries, enclosed in R_{SG} , (1.25° , a typical size of supergranule). Minimum (red) and maximum (blue) number of the grid points enclosed in one supergranule's border out of 30 location on each map. The average of maximum number of the grid points on 300 maps are 265 and average minimum is 65 points.	110
5.6	The horizontal flow velocity map on the source surface in extrapolated model. $V_g = \sqrt{V_\theta^2 + V_\phi^2}$. Color bar for panel is from 0 to 41 m/s. . .	112
5.7	Motion of the footpoints in the interpolated map in (a): latitude 45° and (b): the ecliptic plane. Each color corresponds to different longitude that is rotated to start from the same ϕ	114
5.8	(c) The magnetic field in the interpolated map. The meandering magnetic field lines in the interpolated model. $V_{limit} = 40.0m/s$ which is the equivalent that the borders are covering 1%. Solid lines are the meandering field lines and dashed lines are the Parker field lines. Panel (a) and (d) are 3D field lines, panel (b) and (e) projection in the XY projection and panel (c) and (f) are the projections in XZ plane. The field lines are traced to $R = 8.5$ AU. In all figures, the same color field lines (Parker or the meandering field lines) start from the same locations.	115
5.9	Comparison of the trajectory of solar energetic protons in Parker magnetic field, blue solid line, and the meandering magnetic field, red solid line. (a) Latitude 5° . (b) The ecliptic Plane.	116
5.10	The distribution of the horizontal flow velocity in Hathaway 2016 map.	119
5.11	The model to select the footpoint's next velocity. α_0 is the initial direction of the footpoint velocity, randomly chosen, V_0 is the magnitude of the initial footpoint velocity. Next step, we choose an angle α_1 w.r.t. \mathbf{V}_0 from a normal distribution and decides \mathbf{V}_1 and the same goes for \mathbf{V}_2	120
5.12	(a)	122
5.12	(b)	122
5.12	(c)	123
5.12	(d)	123

5.12	Footpoints motion on the source surface in latitude 45° , (a) and (b), and ecliptic plane, (c) and (d). Colors correspond to various σ that originates from the same footpoint (a) and (c): $V_{limit} = 40 m/s$. (b) and (d): $V_{limit} = 100 m/s$	123
5.13	(a)	124
5.13	(b)	124
5.13	(c)	125
5.13	(d)	125
5.13	Magnetic field lines originates from latitude 45° , (a) and (b), and ecliptic plane, (c) and (d). Colors correspond to various σ that originates from the same footpoint (a) and (c): $V_{limit} = 40 m/s$. (b) and (d): $V_{limit} = 100 m/s$. Dashed green line is the Parker field line emerges from the same footpoint.	125
5.14	Comparison of the motion of the footpoints in all three new method introduced in this study.	128
5.15	Comparing the magnetic field lines in all three models in (a)latitude 45° and (b) ecliptic plane.	129

LIST OF TABLES

TABLE	PAGE
3.1 Path length of Parker field line and the range of path length for 10,000 scatter-free electrons (100 MeV) in the Parker field.	47
3.2 The mean and standard deviations of path length distributions of energetic electrons (μ_e, σ_e) and energetic protons (μ_p, σ_p). Energy of the electrons and protons are 100 MeV.	51
3.3 The mean and standard deviations of path length distributions for the meandering field (μ_B, σ_B) and energetic electrons (μ_e, σ_e). Energy of the electron is 100 MeV.	54

LIST OF SYMBOLS

SYMBOL	DEFINITION
ψ	The angle between magnetic field vector and the radial magnetic field component
Θ	The angular displacement of the particles due to fluctuating field
B_0	Radial magnetic field in R_{sun}
σ	The standard deviation
μ	mean value
μ	cosine of the pitch angle
E	Electric field
c	Speed of light
r_0	Radius of the Sun
R_{sun}	Radius of the Sun
r	Radial distance from the Sun
V_{sw}	Solar wind Speed
V_θ	Latitudinal fluctuation velocity
V_ϕ	Longitudinal fluctuation velocity
V_r	Radial fluctuation velocity

R_l^m	Radial Spectral Coefficient
S_l^m	Poloidal Spectral Coefficient
T_l^m	Toroidal Spectral Coefficient
θ	Colatitude
ϕ	Longitude
ω	Angular frequency of the Sun
MeV	Unit of energy
$K.E.$	Kinetic Energy
α	footpoint's new velocity angle w.r.t. previous velocity vector
δB	Fluctuating field
B_r	Radial component of the magnetic field
B_ϕ	Azimuthal component of the magnetic field
θ	Polar component of the magnetic field
V_g	Horizontal velocity on the source surface and photosphere
δB_θ	Latitudinal fluctuating field
δB_ϕ	Azimuthal fluctuating field
t'	the delayed time
a_n^m	Amplitude of mode (n,m)
C_n^m	Constant coefficient in the amplitude of mode (n,m)

ω_n^m	Frequency of mode (n,m)
N_c	$= V_{rms} T_g / \pi r_0$
β_n^m	random phase
V_{rms}	rms velocity on the source surface
ϕ'	Footpoint's longitude on the source surface
q	Electric charge
m_0	Rest mass
P	Momentum
γ	Lorentz factor
N	Number of modes
Y_n^m	Spherical harmonic function
τ_n^m	Characteristic period of of mode (n,m)
AU	The astronomical unit

To my parents and to him I owe my life

CHAPTER 1

INTRODUCTION

1.1 The solar atmosphere

1.1.1 Photosphere

The photosphere is the lowest layer of the Sun's atmosphere which is located above the convection zone. It is the bright solar surface that can be observed. It emits 99% of the light and heat. The flows on the photosphere are convecting flows. The hot gas goes up in the photosphere, radiates the heat and the cooled gas sinks into the photosphere. The photosphere is a very dense plasma, with the temperature of about 6000 °K. The width of the layer is 500 km, (Gombosi, 2004).

1.1.2 Chromosphere

The chromosphere is a transparent thick layer of the gas (~ 5 Mm) above the photosphere. The density drops and the temperature increase to 10,000 °K, (Gombosi, 2004). The mechanism of the temperature raise is not clear.

1.1.3 The transition region

The transition region is a very narrow layer with a very high temperature gradient; raises up to 10^6 °k. The mechanism of temperature rise is also not unknown.

1.1.4 Corona

The corona is the crown around the Sun that can be seen during solar eclipse. The excessive brightness of the solar disk do not let the corona to be seen without covering it. The temperature of the solar corona goes up to millions of °K and the plasma is fully ionized. The mechanism of the heating is still unknown as well.

1.1.5 Solar wind

The solar corona expands into the interplanetary space which is called solar wind. The high pressure gradient between the inner corona and interstellar medium lead to formation of the solar wind. In the corona, plasma reaches to supersonic velocity. After that, the solar wind starts to expand adiabatically outward. The distance that the solar wind is assumed to be radially outward with a constant velocity is called source surface, see Section 1.3.1. There is a debate over the validity of the adiabatic expansion of the solar wind, however, in the scope of this study, we still assume that it is valid.

1.2 Surface flows on the photosphere

Photosphere shows a variety of surface flows from fast small-scale flows to slow large-scale flows. In this section, we introduce the photospheric flows which can influence the footpoints motion of the interplanetary magnetic field.

1.2.1 Small-scale photospheric flows

1.2.1.1 Granules

Granules are the smallest, most distinct cells in the intensity images, covering the entire photosphere. The bright areas in Figure 1.1a are granule cells and dark areas are granule's boundaries referred to as intergranular network. Granular cells are formed by convecting flows, with upflows in the center, center to borders horizontal flows and downflows in the intergranular network, Figure 1.1b. The size of granules varies from 0.5 to 2 Mm, Rieutord and Rincon (2010), and typical size of 1Mm. The lifetime of granules is the shortest, 5 to 10 minutes, Rincon and Rieutord (2018). The horizontal velocity is reported to be 0.5 to 1.5 km/s, Title et al. (1986), and 1 to 2 km/s and even as high as 7 km/s, <https://solarscience.msfc.nasa.gov/feature1.shtml>. Due to the short lifespan and high velocity advection flow, the granules do not have a steady flow and simply hot gas moves upward, cools, goes down and rise in another location. There is no agreement over the magnitude of the vertical flows. Beckers and Morrison (1970) reported that the vertical flows are higher than the horizontal flows, however, Hathaway et al. (2002) observed that the vertical velocities are lower

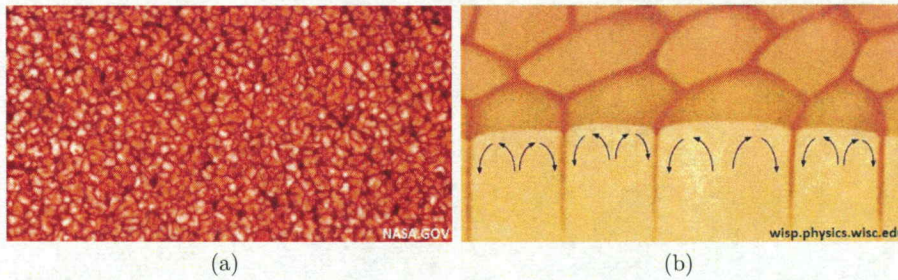


Figure 1.1: (a) Granule cells, (b) convective flows inside granules.

than the horizontal velocities and in the higher wave-number in the spectrum become comparable.

1.2.2 Large-scale surface flows

Granules only cover the outer layer of the photosphere. There are other convective structures that are categorized as large-scale flows that are significantly slower than granular flows.

1.2.2.1 Mesogranules

Mesogranules are convective cells that have the typical size of 5 to 10 Mm, Hathaway et al. (2000). Their characteristics lays between supergranules and granules, however, their existence are still debated and some studies such as Wang (1989) considered them as the ghost cells since there is not a peak responding the mesogranules, see Section 4.2. Hathaway et al. (2000) also didn't find a peak in the expected place in the spectrum which concluded that they still exist, see Section 4.2.

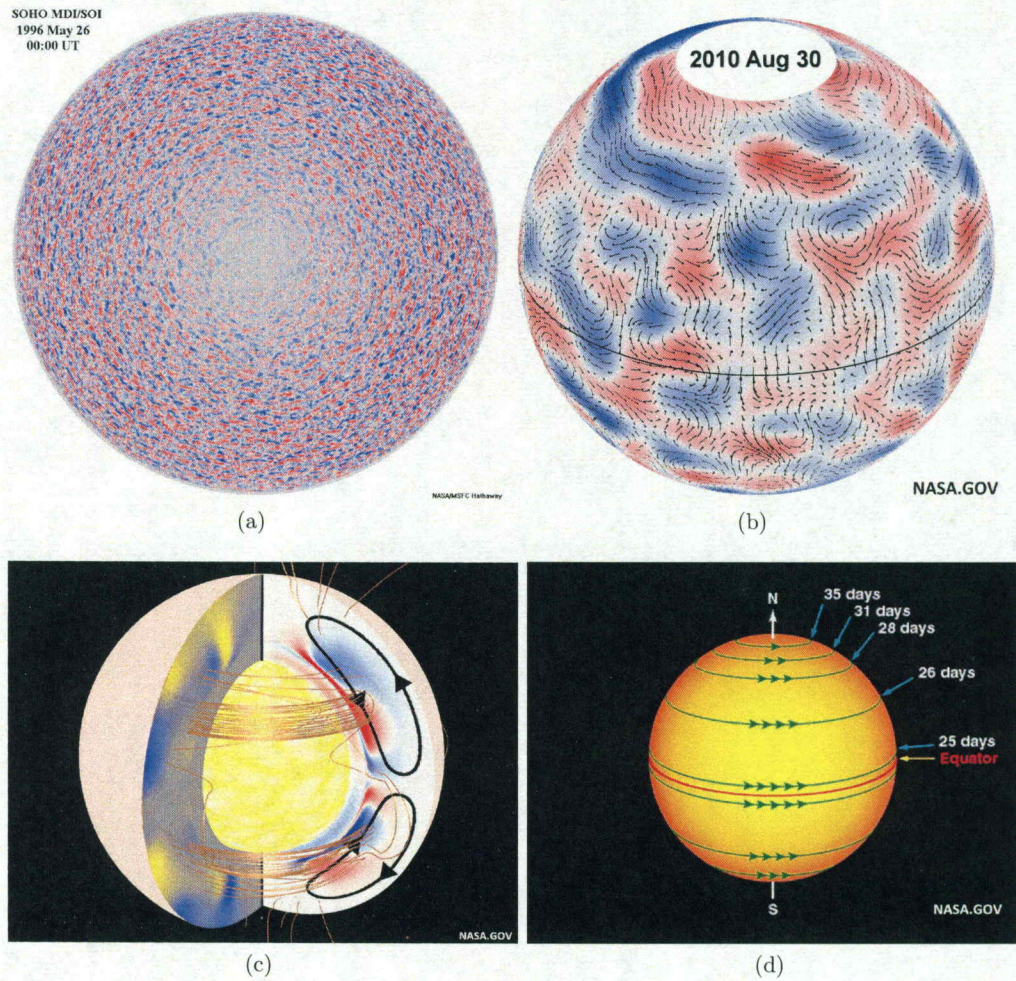


Figure 1.2: (a) Supergranule cells, (b) giant cells, (c) Meridional flows (d) differential rotation.

1.2.2.2 Supergranules

Supergranule cells are convective cells. The same mechanism as granules and mesogranules rules for supergranules, however, supergranules are in deeper layer in the convection zone, 50 Mm, below the granules and mesogranules. The typical size

of the supergranules are 30 to 35 Mm and the lifetime of 24 to 48 hours, Rincon and Rieutord (2018).

Supergranule cells are convecting cells that have the exact physics as granules and mesogranules; are generated by thermal convection. They are located inside convection zone in a layer below mesogranules and above the giant cells in depth of 50 Mm, Hathaway (2012). The typical size is about 30 to 35 Mm, Rincon (2018), that varies from 10 to 100 Mm, Hathaway (2012). The horizontal flow is approximately 300 m/s, Rieutord and Rincon (2010). The maximum horizontal speed, detected in the Doppler velocity images is 500 m/s, Hathaway (2012). The average lifetime is about 1 day, varies from 24 to 48 hours, Rincon and Rieutord (2018). The lifetime of the supergranules depends on the solar cycle, dropped 20% from 1996 to 2002, Gizon and Duvall (2004). There is a north-south symmetry in the lifetime of the supergranules, decreases as we move poleward from ecliptic plane to higher latitudes, Gizon and Duvall (2004). Supergranules are the most important structure in investigating the expansion of open magnetic flux tubes. The magnetic field flux tubes migrate to the boundaries of the supergranules due to the horizontal velocity inside supergranules, form the magnetic concentrations on the boundaries of the supergranules.

1.2.2.3 Giant Cells

The existence of the giant cells are proposed by Bumba and Howard (1965). Giant cells are also convecting cells in the convection zone below the supergranular layer. They are the largest cells in the convection region, the depth of 200 Mm below supergranules cells. The typical size of the giant cells is 200 Mm (cell sizes ≥ 200 Mm)

and the lifetime of 1 to 3 month, Hathaway (2013). The typical horizontal velocity of the giant cells are 10 m/s, Beck et al. (1998).

1.2.2.4 Meridional Flows

Meridional flows are also convective circulations in the depth of the photosphere, Figure 1.2 c. In the upper layer of the photosphere, meridional flow is poleward from the equator to latitude 70° and equatorward from poles to latitude 70° , Hathaway et al. (2010). Meridional flows are slow, in the lower layer, the meridional flows are in the opposite direction, Hathaway et al. (2010). The peak of the meridional flows are slow stable flows with a very long lifetime.

1.2.3 Differential Rotation

Sun is a fluid ball which rotates around north-south axis with a tilt angle of 7.25° . One solar rotation in the equator takes 24.4 days, however, the angular rotation velocity is not the same in the higher latitudes and considerably slower, 30 days in polar region, Figure 1.2 d.

1.3 Magnetic field

Magnetic field plays an important role in the space physics plasma. All other quantities such as electric field, \mathbf{E} , can be derived from the magnetic field. In physics, magnetic field lines do not really exist, however, in space physics, they are treated as physical objects, (Hel, 2009). Magnetic field line is a curve that is always tangential

to the magnetic field vector. they can be generated by starting from an initial point in space, integrate $\hat{\mathbf{b}}(\mathbf{r}(l)) d\mathbf{l}$ where $\hat{\mathbf{b}}(\mathbf{r}(l)) = \mathbf{B}/B$.

In the absence of other forces except EM forces and in case of slow varying magnetic field lines, the drifts (∇B and curvature), can displace energetic particles, however, they jump to a new field line and gyrate around them. In single particle motion, the magnetic field line, often, regarded as trajectory of the solar energetic particles (SEPs). Specially in the absence of Coulomb collisions, they are considered as trajectory of charged particles.

Magnetic field lines are carried away by the magnetized plasma that leave the photosphere. The field lines are either open or closed field lines. The closed field lines have two footpoints and open field lines have one footpoint. Moreover, some of the closed field lines rip apart and form open field lines. In fact, the open field lines are closed field lines that extend to infinity. As mentioned above, the magnetic field lines emerge from the photosphere, magnetized plasma carries the magnetic field into the solar corona, magnetic field lines are open and solar wind is approximately radially outward with a constant speed. The field lines can have both positive and negative polarity.

1.3.1 Interplanetary Magnetic Field - IMF

Solar wind is the expansion of solar corona into the interplanetary space. In the solar corona, the magnetic reconnection accelerate solar wind to the supersonic speed. As mentioned in the previous section, solar wind carries the magnetic field lines into the interplanetary space. Since in the space physics plasma, the conductivity

is very high, $\sigma \rightarrow \infty$, to a very good approximation, the magnetic field is frozen into the plasma, therefore, the solar wind determines the magnetic field. By these assumptions, the MHD model can be used to model the interplanetary magnetic field. The magnetic field also does not affect the plasma flow in a supersonic solar wind $\frac{B^2}{2\mu_0} / \frac{1}{2}\rho u^2 \ll 1$. In a highly conductive plasma, the induction equation can be written as:

$$\frac{\partial \mathbf{B}}{\partial t} = \nabla \times (\mathbf{u} \times \mathbf{B}) \quad (1.1)$$

Note that the solar wind has a very low density, therefore the effect of collision can be ignored and the diffusion term in the induction equation can be dropped. In the co-rotating frame, the frame which is rotating with the same angular speed of solar rotation Ω , the time derivative of vector \mathbf{v} is expressed as:

$$\frac{\partial \mathbf{v}}{\partial t} |_{inertial} = \frac{\partial \mathbf{v}}{\partial t} |_{rotating} + \Omega \times \mathbf{v} \quad (1.2)$$

where Ω is the solar rotation angular velocity. The plasma flow velocity and magnetic field in the co-rotating frame, primed frame, will be:

$$\frac{\partial \mathbf{B}}{\partial t} = \frac{\partial \mathbf{B}}{\partial t} + \Omega \times \mathbf{B} \quad (1.3)$$

$$\mathbf{u}' = \mathbf{u} - \Omega \times \mathbf{r} \quad (1.4)$$

where $\mathbf{u} = \frac{\partial \mathbf{r}}{\partial t}$, \mathbf{r} is the position vector. In non-relativistic coordinate transformation, the magnetic field is invariant to the first order, $\frac{|\boldsymbol{\Omega} \times \mathbf{r}|}{c} \ll 1$, so $\mathbf{B} \simeq \mathbf{B}'$.

By substituting Equation 1.4, Equation 1.3 and invariancy of magnetic field, the induction Equation 1.1 becomes

$$\frac{\partial \mathbf{B}}{\partial t} + \boldsymbol{\Omega} \times \mathbf{B} = \nabla \times [(\mathbf{u}' + \boldsymbol{\Omega} \times \mathbf{r}) \times \mathbf{B}] \quad (1.5)$$

By using the vector identities and $\nabla \cdot \mathbf{B} = 0$, the second term on the right hand side of above equation becomes

$$\nabla \times [(\boldsymbol{\Omega} \times \mathbf{r}) \times \mathbf{B}] = -\mathbf{B}(\nabla \cdot [\boldsymbol{\Omega} \times \mathbf{r}]) + (\mathbf{B} \cdot \nabla)(\boldsymbol{\Omega} \times \mathbf{r}) - [(\boldsymbol{\Omega} \times \mathbf{r}) \cdot \nabla] \mathbf{B} \quad (1.6)$$

On the other hand,

$$\nabla \cdot [\boldsymbol{\Omega} \times \mathbf{r}] = \mathbf{r} \cdot (\nabla \times \boldsymbol{\Omega}) - \boldsymbol{\Omega} \cdot (\nabla \times \mathbf{r}) \quad (1.7)$$

By neglecting differential rotation, $\nabla \times \boldsymbol{\Omega}$ vanishes and $\nabla \times \mathbf{r}$ is always zero which means that the first term in the right hand side of the Equation 1.6 goes to zero.

For the second term in Equation 1.6:

$$(\mathbf{B} \cdot \nabla)(\boldsymbol{\Omega} \times \mathbf{r}) = B_i \frac{\partial}{\partial x_i} \epsilon_{jkl} \Omega_k x_l = B_l \epsilon_{jkl} \Omega_k = \epsilon_{jkl} \Omega_k B_l = \boldsymbol{\Omega} \times \mathbf{B} \quad (1.8)$$

The Equation 1.5 can be rewritten as below:

$$[\nabla \times (\boldsymbol{\Omega} \times \mathbf{r}) \times \mathbf{B}] = \boldsymbol{\Omega} \times \mathbf{B} - [(\boldsymbol{\Omega} \times \mathbf{r}) \cdot \nabla] \mathbf{B} \quad (1.9)$$

which simplifies Equation 1.5 to

$$\frac{\partial \mathbf{B}}{\partial t} + [(\boldsymbol{\Omega} \times \mathbf{r}) \cdot \nabla] \mathbf{B} = \nabla \times [\mathbf{u}' \times \mathbf{B}] \quad (1.10)$$

In the left hand side of above equation,

$$\frac{\partial}{\partial t} + (\boldsymbol{\Omega} \times \mathbf{r}) \cdot \nabla \quad (1.11)$$

is the convective derivative in the co-rotating frame, denoted as $D/Dt =$ which rewrites the Equation 1.10 as

$$\frac{D\mathbf{B}}{Dt} = \nabla \times [\mathbf{u}' \times \mathbf{B}] \quad (1.12)$$

By considering the steady state axial symmetric magnetic field in the co-rotating frame, $\frac{D\mathbf{B}}{Dt} = 0$. We have

$$\nabla \times [\mathbf{u}' \times \mathbf{B}] = 0 \quad (1.13)$$

$\mathbf{u}' \times \mathbf{B}$ is curl-free which means that it can be a gradient of a scalar function:

$$\mathbf{u}' \times \mathbf{B} = \nabla \Phi' \quad (1.14)$$

In space physics, the plasma is highly conductive, $\sigma \rightarrow \infty$, so in the Ohm's law

$$\mathbf{E}' = \frac{1}{\sigma} \mathbf{J} - \mathbf{u}' \times \mathbf{B} \quad (1.15)$$

the first term on the right hand side of above equation vanishes and we have

$$\mathbf{E}' = -\mathbf{u}' \times \mathbf{B} \quad (1.16)$$

On the other hand,

$$\mathbf{E}' = -\nabla\Phi' \quad (1.17)$$

which Φ' is potential in the corotating frame. By multiplying the scalar product of \mathbf{u}' to the both sides of the Equation 1.17 and Equation 1.14 we get

$$\mathbf{u}' \cdot \nabla\Phi' = \mathbf{u}' \cdot (\mathbf{u}' \times \mathbf{B}) \quad (1.18)$$

$$\mathbf{B} \cdot \nabla\Phi' = \mathbf{B} \cdot (\mathbf{u}' \times \mathbf{B}) \quad (1.19)$$

Right hand side of Equation 1.18a and Equation 1.18b vanishes

$$\mathbf{u}' \cdot \nabla \Phi' = 0 \quad (1.20)$$

$$\mathbf{B} \cdot \nabla \Phi' = 0 \quad (1.21)$$

Therefore, in the solar co-rotating frame, Φ' is constant along the magnetic field line and plasma flow (stream) lines.

Let's assume a sphere close to the Sun. In the non-rotating frame, we can assume that the solar wind is almost radially outward and the speed is already increased to its supersonic value. We can approximate the magnetic field value to be close the Sun's surface and the magnetic field in this sphere is also radial, $\mathbf{B} = B_r \mathbf{r}$. This sphere is called the source surface of the interplanetary magnetic field (typically considered at $10R_{sun}$).

On the source surface:

$$\mathbf{u}' = u' \hat{\mathbf{r}} \quad (1.22)$$

$$\mathbf{B} = B_r \hat{\mathbf{r}} \quad (1.23)$$

which means that at the source surface, $\nabla \Phi' = \mathbf{u}' \times \mathbf{B} = 0$. As it is mentioned above, magnetic field lines and plasma flow lines, u' , are equipotential which means that $\nabla \Phi' = 0$ in all space [or in the solar wind or everywhere].

$$\Rightarrow \mathbf{u}' \times \mathbf{B} = 0 \quad (1.24)$$

which shows that if the magnetic field is in the steady state and axisymmetric around solar rotation axis, in the co-rotating frame, \mathbf{u}' and \mathbf{B} are parallel everywhere at all times.

As mentioned above, the \mathbf{B} and \mathbf{u}' are radial on the source surface. Since in the corotating frame (as well as inertial frame), in the spherical coordinates, the solar rotation is only on the azimuthal direction then u'_θ and B_θ are always zero.

$$\mathbf{u}' = u'_r \hat{\mathbf{r}}' + u'_\phi \hat{\boldsymbol{\phi}}' \quad (1.25)$$

$$\mathbf{B} = B_r \hat{\mathbf{r}}' + B_\phi \hat{\boldsymbol{\phi}}' \quad (1.26)$$

Next, we need to find the plasma flow line in the co-rotating frame. In order to find the magnetic field lines, we only need to determine plasma flow lines in the co-rotating frame. Let's assume that solar wind is emerging from the source surface, $r = R_s$. As mentioned in Equation 1.4, $u' = \mathbf{u} - \boldsymbol{\Omega} \times \mathbf{r}$ where u' is the plasma flow velocity in the co-rotating frame, u is the flow velocity in the fixed frame (non-rotating frame). Since $\boldsymbol{\Omega}$ is in the $\hat{\mathbf{z}}$ -direction,

$$u'_r = u_r \quad (1.27a)$$

$$u'_\theta = 0 \quad (1.27b)$$

$$u'_\phi = -\Omega (r - R_s) \sin\theta \quad (1.27c)$$

On the other hand,

$$u'_r = u_r = \frac{dr}{dt} \quad (1.28a)$$

$$u'_\phi = -\Omega r \sin\theta = \frac{d\phi}{dt} r \sin\theta \quad (r \gg R_s) \quad (1.28b)$$

Since we assumed that $u_r = V_{sw}$ is constant,

$$r(t) - r(t_0) = V_{sw} (t - t_0) \quad (1.29a)$$

$$\phi(t) - \phi(t_0) = -\Omega (t - t_0) \quad (1.29b)$$

By omitting t in Equation 1.29 a and b, it turns out to

$$\phi - \phi_{t_0} = \frac{\Omega}{V_{sw}} (r - r(t_0)) \quad (1.30)$$

As mentioned above, $\mathbf{B} \parallel \mathbf{u}'$. Let's assume that the solar wind parcel at $r = R_s$,

$$\frac{B_\phi}{B_r} = \frac{u'_\phi}{u'_r} = \frac{\Omega(r - R_s)\sin\theta}{V_{sw}} \quad (1.31)$$

$$B_\phi = B_r \frac{\Omega(r - R_s)\sin\theta}{V_{sw}} \quad (1.32)$$

Next, $\nabla \cdot \mathbf{B} = 0$,

$$\frac{1}{r^2} \frac{\partial}{\partial r}(r^2 B_r) + \frac{1}{r \sin\theta} \frac{\partial}{\partial \phi}(B_\phi) = 0 \quad (1.33)$$

The second term vanishes since we previously we assumed that B_r only depends on r .

$$\frac{1}{r^2} \frac{\partial}{\partial r}(r^2 B_r) = 0 \quad (1.34)$$

$$B_r = \frac{R_s^2}{r^2} \quad (1.35)$$

where $B_0 = B_r$ at source surface.

$$B_\phi = -B_0 \frac{R_s^2}{r^2} \frac{\Omega(r - R_s)\sin\theta}{V_{sw}} \quad (1.36)$$

In addition, the angle between \mathbf{B}_r and \mathbf{B} are called spiral angle, ψ .

$$\tan \psi = \frac{B_\phi}{B_r} \quad (1.37)$$

which is a quantity that will be used in Chapter 4 to compare the simulation and observation. Note that $\tan \psi$ depends on the solar wind speed. For $V_{sw} = 400$ and 500 km/s, $\psi = 47^\circ$ and 41° respectively.

Solar wind emerges from the Sun and after a certain distance, accelerates to supersonic speed. At this distances, the magnetic field is still close to the Sun's magnetic field. The sphere at this distance (typically $r = 10R_{sun}$) is called "source surface" of the interplanetary magnetic field. By assuming that the solar wind is expanding radially outward in the fixed non-rotating frame; in the co-rotating frame, the plasma co-rotates with the source surface which means that Φ' is constant along the field line.

1.3.1.1 Parker Spiral

Parker (1958) introduced a model for open magnetic field lines in the interplanetary magnetic field

$$\begin{aligned}
 B_r &= B_0 \frac{r_0^2}{r^2} \\
 B_\theta &= 0 \\
 B_\phi &= -B_0 \frac{r_0}{r} \frac{r_0 \Omega \sin \theta}{V_{sw}}
 \end{aligned} \tag{1.38}$$

where Ω is solar rotation and r_0 is sun's radius. For simplicity, the interplanetary magnetic field was unipolar and did not include current sheet.

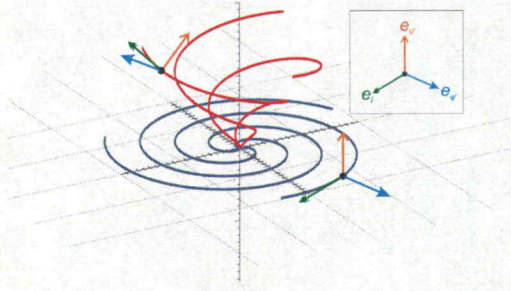


Figure 1.3: Parker Spiral, Marsh 2013

Solar wind is expanding radially outward. Since the conductivity is high, magnetic field is frozen in the plasma. The parcels leaving the photosphere have the constant velocity, V_{sw} . In the Sun's corotating frame, the magnetic field is dragged by azimuthal velocity, sun was assumed a rigid rotator with $\Omega = 2.86 \times 10^{-6}$, shape the Parker spiral field lines, Figure 1.3.

Since magnetic field is invariant in the non-relativistic frame transformation, the spiral shape will remain the same in the stationary frame. By conservation of magnetic flux and frozen-in field assumption Parker magnetic field becomes

$$B_r = B_0 \frac{r_0^2}{r^2} \quad (1.39a)$$

$$B_\theta = 0 \quad (1.39b)$$

$$B_\phi = B_0 \frac{r_0 - r_0 \Omega \sin \theta}{r V_{sw}} \quad (1.39c)$$

To plot Parker spiral, we follow all the parcels left from the same footpoint and consider the solar rotation and connect all the parcels to get the Parker Spiral,

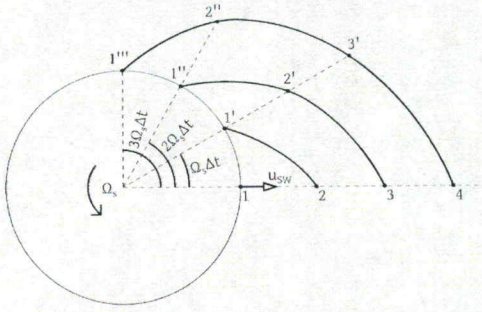


Figure 1.4: The dynamic of Parker spiral

Figure 1.4. In Section 2.1 we present XY and XZ projection of Parker spiral in latitude 45° .

Observation confirmed that the large scale average magnetic field is Parker. Although near ecliptic plane, observations matches the Parker model but in higher latitudes, it is less wounded and field lines inclined towards equator, Forsyth et al. (1996).

1.3.2 The Effect of Surface Flows in the IMF, Large scale Turbulence

As mentioned in Section 1.3.1, Parker (1958) introduced a spiral model for the average interplanetary magnetic field. The Parker field lines stay on the same latitude, Figure 2.2. Forsyth et al. (1996) analyzed the Ulysses spacecraft observations and concluded that in latitudes below $\pm 60^\circ$, the average interplanetary magnetic field is close to Parker Spiral. In higher latitudes, magnetic field lines are less wounded and bent to the ecliptic plane.

Ulysses observations also showed that the density of the solar energetic particles did not drop meaningfully from low latitudes to high latitudes. In the time of

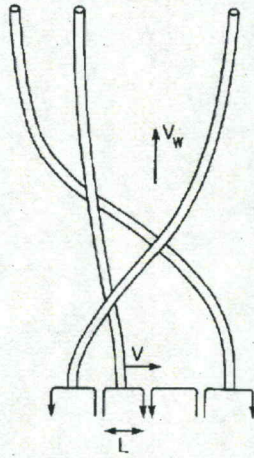


Figure 1.5: Random walk of footpoint

the Ulysses observations, only a CIR accelerate occurred in latitude 40° , which implies that the energetic particles somehow propagated into the higher latitudes from lower latitudes.

Two possibilities are suggested to justify the Ulysses observations. First, there is a cross-field diffusion due to the meandering of the magnetic field from lower to higher latitude, Jokipii and Parker (1968), or the direct connection from the lower to the higher latitudes, Fisk and Jokipii (1999). The meandering magnetic field can be due to the fluctuation of the footpoints, can be written as $\mathbf{B} = \mathbf{B}_{\text{average}} + \delta\mathbf{B}$ where $\mathbf{B}_{\text{average}}$ is the Parker spiral field. Jokipii et al. (1995) suggested that the supergranular flows on the photosphere can cause the random walk of the footpoints that lead to twisting and the braiding of the interplanetary magnetic field, Figure 1.5.

Fisk and Jokipii (1999) considered that there are direct magnetic field lines that connect the lower latitude to higher latitudes. Solar wind that emerges from the

polar coronal holes is assumed to be non-radial, adding the effect of the differential rotation and an offset between the rotation axis of the solar rotation and the expansion of the solar wind. In this study, we adopt the first paradigm that assumes that IMF meanders along the average Parker field.

1.4 Solar Energetic Particles - SEPs

Solar flares and coronal mass ejections (CME) are two sources of the solar energetic particles. Solar flares are frequent solar storms, sometimes accompanied by coronal mass ejections. Cane et al. (1986), categorized SEP events as impulsive and gradual events. In gradual events, SEPs are accelerated by CME-driven shocks. On the other hand, in the impulsive SEP events, energetic particles are accelerated in solar flares. The energy range of SEPs can vary from 10 keV to a few GeV. Solar energetic particles are often electrons, protons and heavier ions from He to Fe that can be accelerated from keV to GeV energies, Kallenrode (1998). Impulsive SEP events are usually He-rich and electron-rich events that last about a few hours, Kallenrode (1998). Impulsive events propagate and expand into interplanetary space in a small cone, $\leq 30^\circ$. In summary, impulsive events occur in a localized region (active region), they accelerate along a few open field lines into the interplanetary space. By assuming that the average magnetic field is Parker Spiral, the SEPs should stay in the same latitude, (Kallenrode, 1998).

1.5 Single Particle Motion

Space physics Plasma is a low density plasma which the Coulomb collisions are rare and can be neglected. As mentioned in Section 1.3.1, the IMF is a large-scale slowly varying magnetic field and the density of the solar energetic particles are significantly low compared to the ambient plasma, solar wind, that the effect of solar energetic particles can be neglected and SEPs can be treated as test particles. SEPs gyrate around the magnetic field lines. They experience drifts that can be significant for higher energetic particles, Marsh et al. (2013). The drifts can occur due to the spatial variation of magnetic field whenever the characteristic length scale of the magnetic field is larger than the particles gyro-radius. The drifts due to spatial variation of magnetic field drift, $V_{\nabla B}$, or curvature drift, V_c .

$$V_{\nabla B} = \frac{c W_{\perp}}{q B^2} \mathbf{b} \times \nabla \mathbf{B} \quad (1.40a)$$

$$V_c = \frac{2 c W_{\parallel}}{q B^2} \mathbf{b} \times \nabla \mathbf{B} \quad (1.40b)$$

where $W_{\perp} = \frac{1}{2} m v_{\perp}^2$ and $W_{\parallel} = \frac{1}{2} m v_{\parallel}^2$ for non-relativistic case.

In this study, the fully relativistic Lorentz equation has been solved that has already included the drifts so we do not need to calculate the drifts separately.

The trajectory of the particles are integrated using the Wirz method, Chabert et al. (2009). We solve the Lorentz equation of motion in a fixed non-rotating frame,

$$\frac{d\mathbf{P}}{dt} = q(\mathbf{E} + \frac{1}{\gamma m_0} \mathbf{P} \times \mathbf{B}) \quad (1.41)$$

where γ is the Lorentz factor and m_0 is the rest mass of the particle. In the fixed frame, the electric field is determined by $\mathbf{E} = -\mathbf{V}_{\text{sw}} \times \mathbf{B}$.

1.6 Simulation of test particles

We have developed a fully relativistic full-orbit test particle simulation code. We solve the Lorentz equation in the fixed non-rotating frame.

In our first attempt, we tried RK45 but this method needed a very small time step ($dt \simeq 10^{-7} \text{sec}$) to yield stable results. We have examined other methods that will be discussed below.

1.6.0.1 Boris Particle Tracking Method

Boris particle tracker, takes the velocity and apply half of the electric field impulse, then going through gyromotion from magnetic field and finally apply the other half of the electric field impulse. Advantage of Boris method is getting additional accuracy by using the average velocity for magnetic impulse.

This method is second order which was specially developed for charged particles and adding initial accuracy to the magnetic field, Chabert et al. (2009).

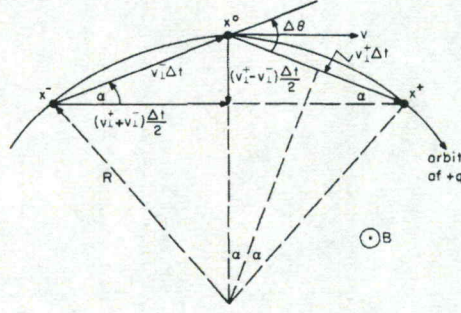


Figure 1.6: Boris Method

$$\mathbf{v}_- = \mathbf{v}_{n-\Delta t/2} + \left(\frac{q\Delta t}{2m}\right)\mathbf{E} \quad (1.42a)$$

$$\frac{\mathbf{v}_+ - \mathbf{v}_-}{\Delta t} = \frac{q}{m} \left(\frac{q\mathbf{v}_+ + \mathbf{v}_-}{2} \times \mathbf{B} \right) \quad (1.42b)$$

$$\mathbf{v}_{n+\Delta t/2} = \mathbf{v}_+ + \left(\frac{q\Delta t}{2m}\right)\mathbf{E} \quad (1.42c)$$

$$\frac{\mathbf{x}_{n+1} - \mathbf{x}_n}{\Delta t} = \mathbf{v}_{n+\Delta t/2} \quad (1.42d)$$

$$(1.42e)$$

1.6.0.2 Wirz's Method or Modified Boris Method

Wirz method is based on obtaining better approximation of magnetic field at the midpoint in each time step, Figure 1.7.

In this method a new coordinates system is defined, Equation 1.43(a). The radial unit vector \hat{h}_r is multiplied by the particle sign to be the gyromotion's direction. Predicted position is calculated by Equation 1.43(b). By initial velocity \mathbf{v}_n we can calculate the first intermediate velocity \mathbf{v}_- . \mathbf{v}_- determines a predicted midpoint by

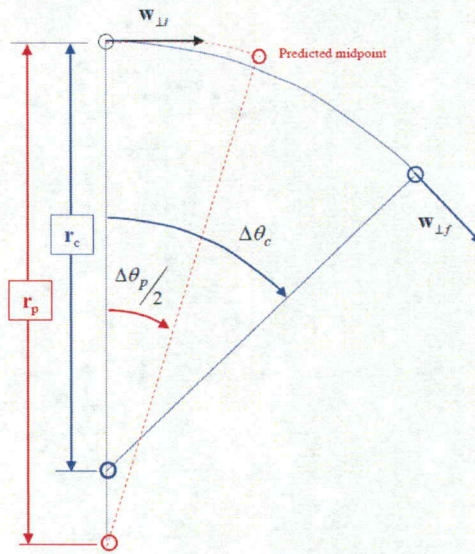


Figure 1.7: Wirz Method

applying half of the electric impulse, Equation 1.43(c). Then the corrected B can be used to calculate corrected coordinate system and $\Delta\theta$ to update the velocity v_+ and finally v_{n+1} by applying the other half of electric impulse, Equation 1.43(e), Chabert et al. (2009).

$$\hat{h}_{\parallel} = \frac{\mathbf{B}}{B}, \hat{h}_{\perp} = \frac{\mathbf{v} - (\mathbf{v} \cdot \hat{h}_{\parallel})\hat{h}_{\parallel}}{|\mathbf{v} - (\mathbf{v} \cdot \hat{h}_{\parallel})\hat{h}_{\parallel}|}, \hat{h}_r = \frac{q}{|q|}(\hat{h}_{\parallel} \times \hat{h}_{\perp}) \quad (1.43a)$$

$$\Delta x_{\parallel} = \Delta(\mathbf{v} \cdot \hat{\mathbf{h}}_{\parallel})\hat{h}_{\parallel}, \Delta x_{\perp} = r_L \sin(\Delta\theta)\hat{h}_{\perp}, \Delta x_r = -r_L[1 - \cos(\Delta\theta)]\hat{h}_r \quad (1.43b)$$

$$\mathbf{v}_- = \mathbf{v}_{n-\Delta t/2} + \left(\frac{q\Delta t}{2m}\right)\mathbf{E} \quad (1.43c)$$

$$\frac{\mathbf{v}_+ - \mathbf{v}_-}{\Delta t} = \frac{q}{m}\left(\frac{\mathbf{v}_+ + \mathbf{v}_-}{2} \times \mathbf{B}\right) \quad (1.43d)$$

$$\mathbf{v}_{n+\Delta t/2} = \mathbf{v}_+ + \left(\frac{q\Delta t}{2m}\right)\mathbf{E} \quad (1.43e)$$

$$\frac{\mathbf{x}_{n+1} - \mathbf{x}_n}{\Delta t} = \mathbf{v}_{n+\Delta t/2} \quad (1.43f)$$

CHAPTER 2

PRELIMINARY RESULTS

In this chapter, we discuss the preliminary models that we apply to investigate the propagation of the solar energetic particles. We first review the propagation of the solar energetic particles in the Parker magnetic field and compare it to Marsh et al. (2013). Next, we assume that the interplanetary magnetic field consists of an average Parker field and a fluctuation field, $\mathbf{B} = \mathbf{B}_{\text{Parker}} + \delta\mathbf{B}$. The footpoints' velocity is specified to have an amplitude in the range of (0 , 2 km/s), granular speed, in both the latitudinal and longitudinal direction.

2.1 Propagation of solar energetic particles in the Parker field

2.1.1 Parker Spiral

Parker (1958) introduced a spiral interplanetary magnetic field model. The magnetic field lines can be constructed as follows: We select a fixed footpoint on the source surface. We follow all the solar wind parcels that emerged from the same footpoint in time. The parcel that left the source surface at $t = 0$ is still close to the source surface. The parcel n that left the source surface at $t = -n\Delta t$, is currently at

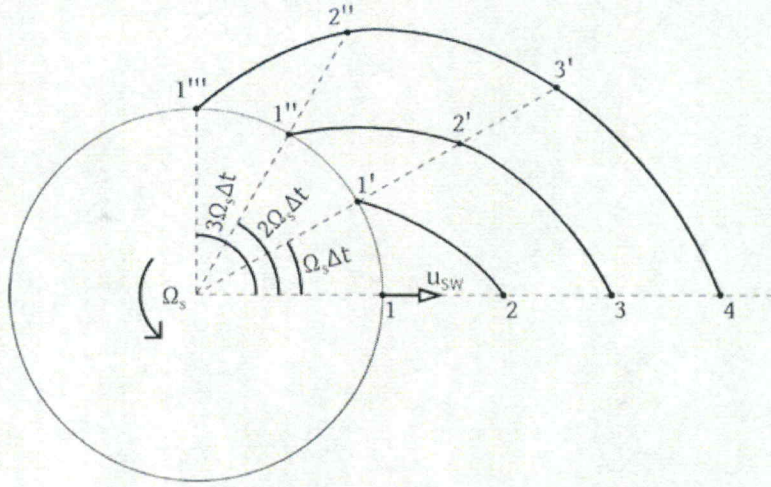


Figure 2.1: The Parker magnetic field line as dragged out by the radial solar wind.

$(r, \theta, \phi) = (V_{sw}n\Delta t, 0, -\Omega n\Delta t)$. By connecting all these parcels that emerged from the same footpoint, we find the Parker Spiral field line, as indicated in Figure 2.1.

In this section, we choose the field parameters according to Marsh et al. (2013) to compare the results of propagating of the solar energetic particles. The Parker field is given by

$$B_r = B_0 \frac{r_0^2}{r^2} \quad (2.1a)$$

$$B_\theta = 0 \quad (2.1b)$$

$$B_\phi = -B_0 \frac{r_0}{r} \frac{r_0 \Omega \sin(\theta)}{V_{sw}} \quad (2.1c)$$

where $V_{sw} = 500$ km/s, $B_0 = 1.78 \times 10^{-4}$ T at the source surface, $\Omega = 2.86 \times 10^{-6}$ rad/s, r_0 is the heliocentric distance of the source surface and r .

2.1.2 Trajectory of solar energetic particles in Parker magnetic field

We inject solar energetic protons and electrons in an energy range of 1 to 100 MeV with random pitch angles at several latitudes, to investigate their trajectories and how they deviate from the Parker field lines. The particles are quickly focused, however, the effect of drifts are significant in case of high energy protons which immediately leave their original Parker field line and jump on to another line. This jump has a significant impact in chapters 3, 4 and 5.

We also inject a 1000 protons near the ecliptic plane in order to confirm the result of Dalla et al. (2013) and Marsh et al. (2013). They showed that the drift in the higher energy end of SEP spectrum is significant which we confirm. Figure 2.3, shows final position of one thousand 100 MeV protons. The protons are injected in an area confined between co-latitude $90^\circ \pm 4^\circ$ and longitude $\pm 4^\circ$ with a random initial pitch angle. We follow them for 12 hours. The green lines are the Parker fields at the borders of the injection area and the scattered red dots are protons final position at $t = 12$ hours. We do not include co-rotation as done in Marsh et al. (2013) to indicate the SEPs leave the original field lines.

The 100 MeV protons travel to 9 AU in 12 hours. We also follow one thousand 100 MeV electrons to 9 AU which takes 5 hours to reach 9 AU. This will let us to compare the drifts of electrons and protons in the similar condition such as initial kinetic energy. In case of electrons, the drifts are expected to be smaller since the curvature and gradient drifts depends on the charge to mass ratio, Dalla et al. (2013) and Marsh et al. (2013), which we confirm in Figure 2.4.

2.2 Fluctuating magnetic field based on Granular flows

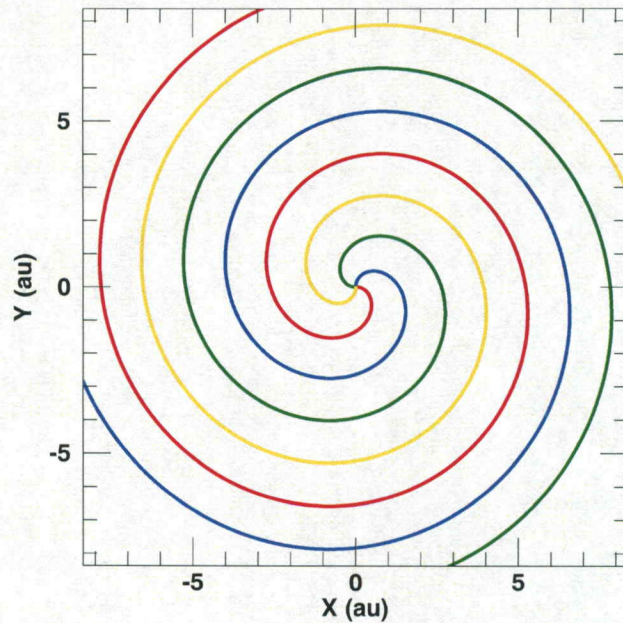
As is mentioned above, in the Parker spiral, the footpoints co-rotate with the Sun. We investigate all photospheric flows and choose the largest flows velocity i.e. granular speed. As mentioned in chapter 1, the granule is the hot gas that rises and moves to the sides, cools and falls down on the borders of the cells. The horizontal speed is about 2 km/s. The horizontal speed of granules are comparable with the linear speed of solar rotation on the surface of photosphere (2.1 km/s at the ecliptic plane). Granules' last about 8 to 10 minutes, born again in neighboring locations.

To identify an individual magnetic field line, we choose a single footpoint. First, we generate the average Parker field line numerically. We then assign some random horizontal speed, V_θ and V_ϕ , with the amplitude of horizontal granular speed and after every lifetime of granules, the horizontal speed is changing to another random value. The random values are chosen from a normal distribution in the range of -2000 to 2000 km/s, centered at zero. Figure 2.5a and Figure 2.5b show the 3D plot of a single magnetic field line at latitude 45° and in the ecliptic plane, respectively. The red solid curve is the meandering field line and the blue curve is the Parker field line originating from the same starting footpoint. As can be seen, the meandering field fluctuates enormously, deviating strongly from the initial Parker field. However, on large-scales, it still keeps its spiral shape.

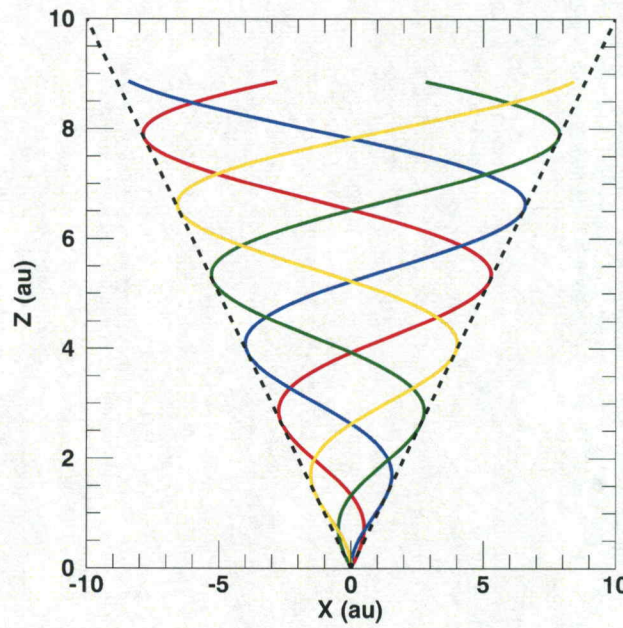
$$\delta B_\theta = B_0 \frac{r_0}{r} \frac{V_\theta}{V_{sw}} \quad (2.2a)$$

$$\delta B_\phi = B_0 \frac{r_0}{r} \frac{V_\phi}{V_{sw}} \quad (2.2b)$$

In order to inject the particles in the numerically generated meandering magnetic field, many assumptions need to be made. First, the field is generated numerically on a 3D spherical mesh. The mesh points on the surface of the photosphere were equally spaced in both latitudinal and longitudinal directions. The other layers of the mesh are in equidistant in the radial direction but it is irregular in the other directions. The magnetic field lines are initiated on the source surface and are followed in the interplanetary space and the values are recorded in each layer in a file. It is necessary to have irregular mesh point since the field lines are meandering and we can not predict the next location of the mesh points. The magnetic field in each point are decided by linear interpolation of the eight vertices of the cell. 100 MeV protons are injected in this meandering field. They stay near the Sun and do not propagate into the interplanetary space. Most of them even reverse and go back to the Sun. The fluctuations are too strong for particles to propagate far. The results show that the model needs significant modifications.



(a)



(b)

Figure 2.2: (a) XY and (b) XZ projection of four Parker spiral line that originated from latitude 45° . Colors represents the field lines that emerged from the footpoints at the same latitude 45° and multiple longitudes. The dashed lines in (b) show the locus of same latitude, 45° .

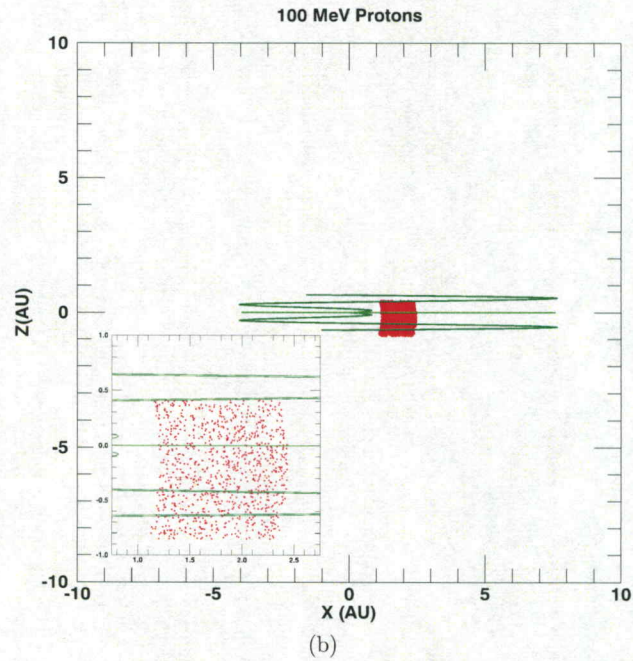
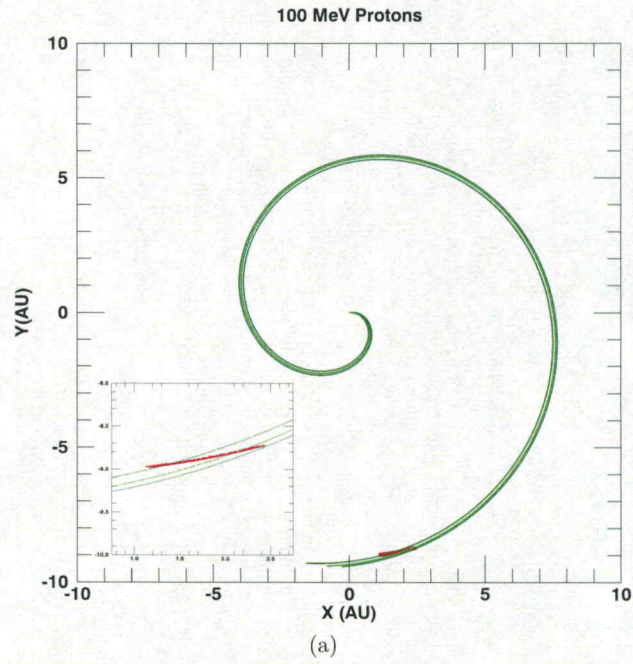


Figure 2.3: The (a) XY and (b) XZ projection of final position of a thousand 100 MeV protons which are injected in the area of latitude $(-4^\circ, 4^\circ)$ and longitude $(-4^\circ, 4^\circ)$ on the source surface. The green solid lines are the Parker field lines originated from the borders of injection area. The light green line is the Parker field line emerge from the center of injection area.

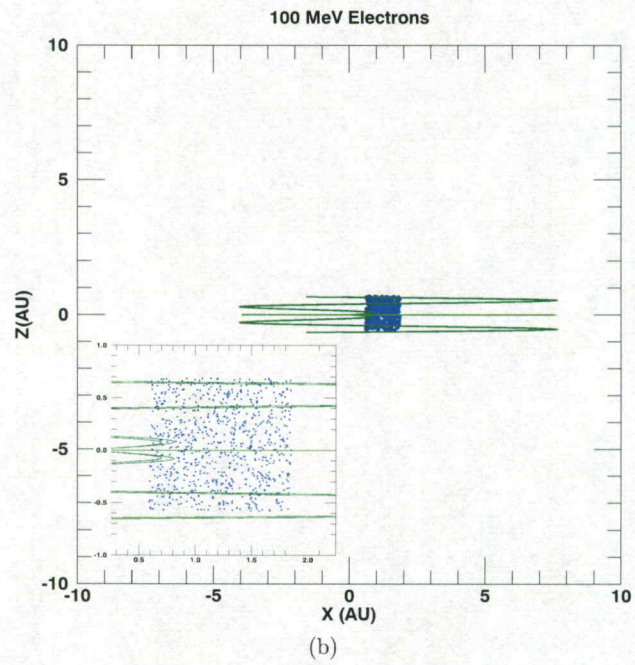
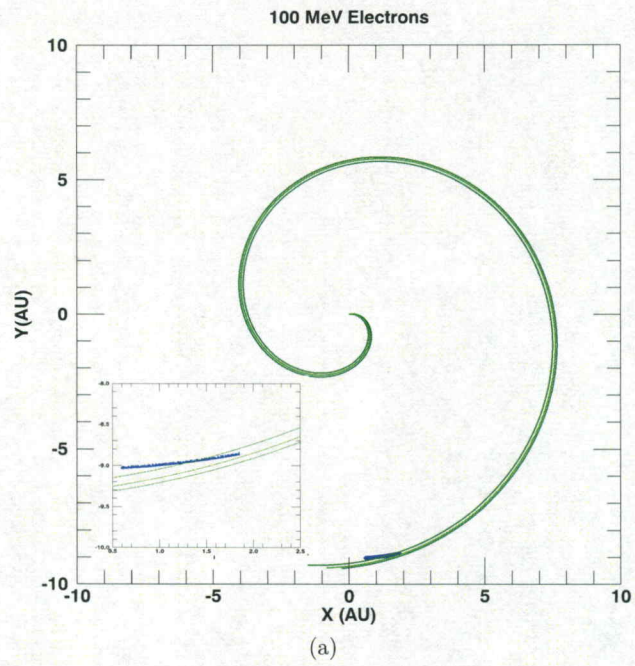


Figure 2.4: The same as Figure 2.3 for 100 MeV electrons. The travel time is 5 hours.

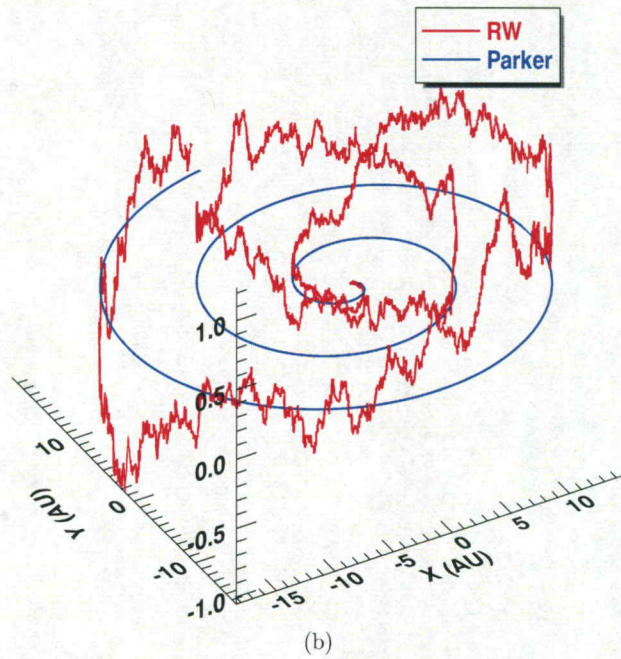
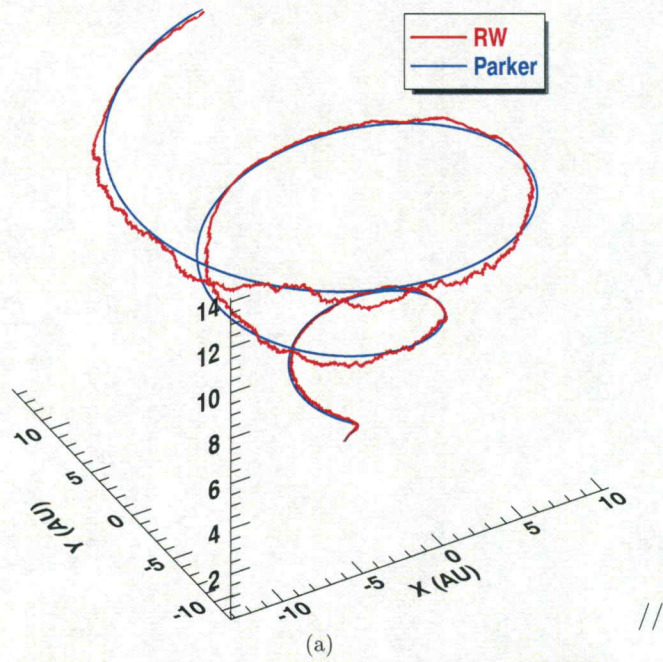


Figure 2.5: 3D plot of a single magnetic field in (a) latitude 45° and (b) ecliptic plane. The red solid line shows the meandering field and the blue solid line is the Parker field line from the same starting point.

CHAPTER 3

GIACALONE'S MODEL FOR INTERPLANETARY MAGNETIC FIELD

3.1 Introduction

As it is mentioned in Section 1.2, the footpoints are not fixed points on the source surface which co-rotates with the Sun. The advecting flows on the source surface can displace footpoints in random directions. Jokipii and Parker (1968) suggested that supergranular fluctuations on the photosphere can result in random walk of the footpoint of solar magnetic field in the corona, which further lead to the braiding of the magnetic field lines.

Giacalone (2001) proposed a solar wind magnetic field model which explicitly examines the effect of random walk of footpoint on the source surface. Note that Giacalone (2001) assumed that the solar wind is radially outward at the inner boundary. By using a divergence-free flow pattern with a parameter V_{rms} that determines the amplitude of the random motion, Giacalone (2001) obtained meandering field lines for which large longitudinal and latitudinal excursions are possible. Such meandering field lines can lead to, e.g., significant latitudinal transport of energetic particles ac-

celerated by the Corotation Interaction Region (CIR) that was observed by Ulysses, (Giacalone, 2001).

Pei et al. (2006) adopted the Giacalone (2001) model with a V_{rms} of 2.0 and 4.0 km/sec. They pointed out that with these values of V_{rms} , a field line can differ from the Parker field in such a way that its length, at 1 AU, can be shorter than the nominal Parker value of ~ 1.2 AU. Pei et al. (2006) suggested that values of V_{rms} larger than 4.0 km/sec are not impossible as the horizontal speeds in the active region can go as high as 10.0 km/sec. However, a large horizontal speed in the active region does not necessarily correspond to a large horizontal speed at the source surface. To accurately obtain the velocity profile at the source surface from the photosphere, a MHD calculation is needed.

Kelly et al. (2012) also adopted the approach of Giacalone (2001) and examined the propagation of energetic protons (with energies 500 keV to 1 GeV) in a meandering field. They considered a value of $V_{rms} = 2.0$ km/sec and argue that in the scatter-free case, protons follow the meandering field lines closely and cross-field diffusion is entirely due to the meandering of the field. Particles only jump to another field line when pitch angle scattering is introduced. In later work, Dalla et al. (2013) analytically and Marsh et al. (2013) numerically investigated the cross-field displacement of very high energy protons and heavy ions, and showed that even in the pure Parker field, drifts (curvature and gradient) can not be ignored. These results differ from that of Kelly et al. (2012). One possible cause of this discrepancy may be because Kelly et al. (2012) followed protons for a shorter time. As we will show in this work, we find that energetic electrons (and protons too) do not follow field

lines (whether the field line is Parker or non-Parker) even in the scatter-free regime. As the field line meanders more, the cross-field displacement gets larger. Our results agree with that of Dalla et al. (2013) and Marsh et al. (2013). Dalla et al. (2013) further illustrated that the drifts strongly depends on the charge to mass ratio and can be much higher for partially ionized heavier ions.

Recently, Zhao et al. (2019) developed a fraction velocity dispersion analysis (FVDA) method to obtain electron path length in impulsive electron events. The traditional VDA method is subject to large uncertainties due to the fact that the onset time can not be determined precisely. The FVDA method, uses of the rapid rising phase, yield more accurate results than the traditional VDA analysis.

An interesting finding of the Zhao et al. (2019) work is that the path lengths of many electron events are very close to the Parker value, suggesting that the parameter V_{rms} that describes the field line meandering can not be too large. Clearly, to better construe the results of Zhao et al. (2019), numerical experiments that study the dependence of the path length of particles and field lines on V_{rms} is necessary.

In this chapter, we adopt the Giacalone (2001) description of the meandering magnetic field. In particular, we examine, how the path length of a random magnetic field line, and the path length of energetic electrons depend on the rms speed V_{rms} . We consider “scatter-free” propagation in this work as this will single out the effect of meandering field on the propagation of SEPs. The effect of solar wind turbulence, which leads to pitch angle scattering of electrons, will be reported in a future study. The presence of curvature drift assures that electrons do not stay on the same field line. Such is the case even for the Parker field, where analytical expression of the drift can

be obtained. In a meandering field, the curvature of field can not be described by any analytical expression. Nevertheless, we can still investigate its motion numerically. As we will see, the path length for meandering field and the path length for energetic electrons are different.

In this chapter, we describe the IMF model and the numerical simulation method in section Section 3.2. In section Section 3.3, we show how the field line path length and particle path length depend on V_{rms} ; we also show the footpoints motion in the adopted model; finally, we compute the angular displacement between the initial and the final Parker field line that particles reside. This angle, putting into the context of impulsive solar electron events, can be regarded as a measure of how spreading the event is in longitude and latitude. The conclusions are presented in Section 3.4.

3.2 Model Description

3.2.1 Interplanetary Magnetic Field

We follow closely the approach of Giacalone (2001) in describing the interplanetary magnetic field (IMF). The sun is assumed to have a constant rotation speed Ω . In the co-rotating frame, the solar wind is radially outward at the inner boundary, $\mathbf{V}_{sw} = V_{sw}\mathbf{r}$, at the constant speed. The magnetic field is frozen into the plasma and therefore no magnetic reconnection is included. The interplanetary magnetic field consist of two terms, the average Parker field and a random field due to the footpoint motion, $\mathbf{B} = \mathbf{B}_{parker} + \delta\mathbf{B}$.

The average Parker field is:

$$B_r = B_0 \frac{r_0^2}{r^2} \quad (3.1a)$$

$$B_\theta = 0 \quad (3.1b)$$

$$B_\phi = -B_0 \frac{r_0}{r} \frac{r_0 \Omega \sin \theta}{V_{sw}} \quad (3.1c)$$

where Ω is solar rotation and r_0 is the Sun's radius. The fluctuating field describes the effect due to the footpoint motion, (V_θ, V_ϕ) :

$$\delta B_\theta = B_0 \frac{r_0}{r} \frac{V_\theta}{V_{sw}} \quad (3.2a)$$

$$\delta B_\phi = B_0 \frac{r_0}{r} \frac{V_\phi}{V_{sw}} \quad (3.2b)$$

where

$$V_\theta(\theta, \phi', t') = \frac{1}{\sin \theta} \frac{\partial \psi(\theta, \phi', t')}{\partial \phi} \quad (3.3a)$$

$$V_\phi(\theta, \phi', t') = -\frac{\partial \psi(\theta, \phi', t')}{\partial \theta} \quad (3.3b)$$

In the above, V_θ and V_ϕ are the velocity of the footpoint at the time when the solar wind left the Sun,

$$t' = t - \frac{r - r_0}{V_{sw}} \quad (3.4a)$$

$$\phi' = \phi - \Omega t' \quad (3.4b)$$

where (r_0, θ, ϕ') is the position of the footpoint at t' , and ψ is a stream function. In Giacalone (2001), ψ is given by a sum of N modes of spherical harmonics, with the coefficients both time dependent and containing a random phase, β_n^m .

$$\psi(\theta, \phi', t') = \sum_{n=0}^N \sum_{m=-n}^n a_n^m \exp(i\omega_n^m t' + \beta_n^m) Y_n^m(\theta, \phi') \quad (3.5)$$

where the amplitude a_n^m depends on the rms speed of the random motion V_{rms} through,

$$a_n^m = 6V_{rms} G_n^m \left(\sum_{n=0}^N \sum_{m=-n}^n G_n^m \right)^{-1} \quad (3.6)$$

$$G_n^m = \left[\left(1 + \left(\frac{n}{N_c} \right)^{\frac{10}{3}} \right) \left(1 + (\omega_n^m T_c)^{\frac{5}{3}} \right) \right]^{-\frac{1}{2}} \quad (3.7)$$

where T_c is the characteristic lifetime scale of supergranule, which were taken to be 1 or 2 days in Giacalone (2001), and $N_c = V_{rms} T_c / \pi r_0$. The frequency $\omega_n^m = 1/\tau_n^m$ is related to a period τ_n^m given by $\tau_n^m = \frac{\pi r_0}{V_{rms}} \left(\frac{1}{n} + \frac{1}{m} \right)$. Even though the surface flow, in particular the supergranules motion is on the photosphere, we have adopted the random motion of the footpoint at the source surface. The evolution of the solar magnetic field between the photosphere and the source surface is complicated. However,

it is conceivable that the random footpoint motion at the source surface is caused by the random motion of plasma on the photosphere on the scale of supergranule. In the next section, we plot the trajectory of the footpoint which is described by equation Equation 3.3.

3.2.2 Simulation of test particles

As it is discussed in chapter 1, we solve the Lorentz equation of motion in a fixed and non-rotating frame. We inject the electrons with different energies at the source surface and follow the trajectories into interplanetary space and calculate the path lengths of individual electrons. We emphasize that our study is an ensemble study in which the magnetic field contains a random component. Electrons injected at different locations at the source surface and with different random initial pitch angles will experience different magnetic fields. When the rms speed V_{rms} is set to zero, our electron trajectories become trajectories in a Parker field.

Since our study is an ensemble study, our results of the path length of electrons and field lines are shown as distributions. In some cases, these distributions are very Gaussian-like. To claim the distributions are Gaussian, however, normality tests have to be done. We adopt the Shapiro-Wilk test Shapiro and Wilk (1965) in this work and perform it on all distributions.

3.3 Results and Discussion

3.3.1 Flow pattern on the source surface

We first examine the flow pattern on the source surface where the footpoint of the solar wind resides. In the work of Giacalone (2001), the source surface is assumed to be at the photosphere. The footpoint random motion on the source surface consists of two components: \mathbf{V}_θ , \mathbf{V}_ϕ and the strength of the random motion is given by $|\mathbf{V}_g| = \sqrt{|\mathbf{V}_\theta|^2 + |\mathbf{V}_\phi|^2}$. With \mathbf{V}_θ and \mathbf{V}_ϕ given, we can trace the footpoint of solar wind on the source surface.

Figure 3.1 plots the magnitude of the source surface flow field. The parameters we use are: $V_{rms} = 0.6$ km/sec, $N = 50$ and $T_c = 2$ days. The parameter T_c is related to the supergranules lifetimes. For different sets of parameters, the flow field does not vary significantly. In the following, we focus on the case of $N = 50$ modes and a lifetime $T_c = 2$ days. The top panel is for V_θ ; the middle panel is for V_ϕ ; and the bottom panel is for $|V_g|$. The color bar in the top and middle panels range from -1000 m/s to $+1000$ m/s and the color bar in the bottom panel ranges from 0 to 1400 m/s. As can be seen from the figure, the flow speed can attain extremely high values near the poles because $\sin \theta$ approaches zero over there. This does not affect our simulation since we limit our simulation to latitudes below ± 80 and focus on particles propagating near the ecliptic plane only. The vector flow velocity map is also shown in Figure 3.2.

3.3.2 Magnetic Field

We next examine the magnetic field topology when the footpoints undergo a random walk process. In Figure 3.3, we generate four magnetic field lines, solid lines, at the ecliptic plane from the Sun to 10 AU in panel a and b and the same field lines from the Sun to 1 AU in panel c and d. The dashed lines are the corresponding Parker field lines with the same color. The XY and XZ projection of the fields is presented. The colored lines are four different field lines with equal separation in longitude. In all four sub-figures, same color denotes the same field line. From (c) and (d), we can see that the solid field lines, inside 1 AU are mostly Parker-like with small deviations in the XZ plane even though it is not close to the actual Parker field, dashed lines.

3.3.3 Trajectory of Electrons

We first examine trajectories of electrons and protons in the Parker field. Our results for 100 MeV protons (not shown here) agree with Marsh et al. (2013) and we get the same amount of curvature drift. Next, the fluctuating magnetic field was added to the simulation of electrons and the changes of the trajectories were inspected. Figure 3.4 shows trajectories of some example electrons. These electrons are injected at different latitudes with random pitch angles. In each subfigure, the red solid line is the trajectory of the electron, the green dashed line is the Parker field line the electron initially ties to, and the blue dashed line is the Parker field line the electron ties to when it is at 1 AU. The 3D graph as well as the projections on the XY and XZ plane are shown.

3.3.4 Footpoint's trajectory on the source surface

Denote $\mathbf{x}(t)$ as the trajectory of each electron. At each point on the trajectory, the solar wind parcel left the Sun at t' , given by equation Equation 3.4. We trace back the parcels to the source surface (in this chapter, photosphere), omitting the displacement due to the solar rotation, and define that as the footpoint's trajectory. This footpoint's trajectory is only due to fluctuating velocities, and is shown in Figure 3.5. The background in Figure 3.5 is the horizontal surface flow field, $\mathbf{V}_{\mathbf{g}} = V_{\theta}\hat{\theta} + V_{\phi}\hat{\phi}$ at $t' = 0$. The colored solid curve is the footpoint's trajectory. The starting point, corresponds to $t = 0$, is colored with purple and the ending point is colored with red. The ending point corresponds to electron's position at one AU. The parcel at this end

point, left the Sun four days earlier, having $t' \sim -4$ days. The color bar represents the magnitude of the surface flow on the source surface and it is not related to the color of the footpoint's trajectory. From the figure we can see that in regions where the surface flow does not change significantly in four days, the footpoints move along the flow as we expected.

3.3.5 Path Length Distributions

Next we investigate the distribution of path length of ten thousands electrons. We inject ten thousand electrons with random pitch angles at random longitudes in the ecliptic plane, colatitude 90° , at the inner boundary with $r_{in} = \alpha r_0$. Since we set the location of the source surface at the photosphere in this chapter, $\alpha = 1$.

3.3.5.1 Path length distribution of electrons in Parker field

We first calculate Parker field's path length and the path length of ten thousand electrons in a Parker field for different solar wind speeds. The results are shown in Table 3.1 and Figure 3.6.

In Figure 3.6, the blue line is the path length of a Parker field and the red line is the distribution of electron path length at the distance of one AU in the Parker field. As expected, the Parker field length is a δ -function. The distributions of electron path length is caused by the differences in the initial pitch angles for these electrons. It is interesting to note that due to drift, some electrons have smaller path length than the Parker field line. This is possible because the Parker field is the most curved (and therefore the longest path length) at the ecliptic plane and with drift particles can

Table 3.1: Path length of Parker field line and the range of path length for 10,000 scatter-free electrons (100 MeV) in the Parker field.

V_{rms} km/s	Parker Field Path (AU)	Electrons' Path in Parker (AU)
350	1.207	1.207 - 1.214
400	1.163	1.163 - 1.170
450	1.131	1.130 - 1.138
500	1.107	1.106 - 1.113
600	1.075	1.074 - 1.082
700	1.055	1.054 - 1.062
800	1.041	1.041 - 1.048

move off the ecliptic plane. The range of electron path lengths is about ± 0.1 AU. For different solar wind speeds, the Parker field length and the range of electron paths are slightly different. These are summarized in table Table 3.1. This table shows that by changing the solar wind speed from 350 to 800 km/s, the Parker field path length decreases from 1.207 to 1.041 AU. The change is about 0.17 AU and is more than 0.1 AU, the spreading of the electron path length.

3.3.5.2 Path length distribution of electrons in the meandering field

Next, we examine how the random footpoint flow velocity affects Figure 3.6. As discussed above, the path length depends on the solar wind velocity. We set the solar wind speed to 400 km/s. In each case, we then obtain the path length distribution of ten thousand electrons and protons that have different initial pitch

angles. We also obtain the path length distributions of ten thousand magnetic field lines. To ensure that each simulation is independent, we change the surface flow map for each electron, proton or field line. We fit all distributions by a Gaussian distribution except those in Figure 3.7. To examine the validity of approximating the distributions by a Gaussian distribution, we perform the Shapiro-Wilk test, and examine the p -values with a α -level = 0.05, to check if the Null Hypothesis can be rejected or not. Even in the cases where the Shapiro-Wilk test rejects the Null Hypotheses, a Gaussian fit is still presented. All distributions are normalized.

Energy dependency of electrons path length distribution

We examine first the energy dependency of the electron path length distributions at 1 AU. Ten thousands of electrons with three different kinetic energies, 1, 10 and 100 MeV are considered, Figure 3.7. The blue, red and green solid lines are the path length distributions of 1, 10, 100 MeV electrons, respectively. The rms speed of fluctuations, $V_{rms} = 0.6$ km/s, Giacalone (2001). All electrons are injected in the ecliptic plane at random longitudes with random initial pitch-angles. Figure 3.7 clearly shows that path length distributions for these three cases are almost identical. We conclude that the path length distribution of electrons has weak dependency on electron's kinetic energy. Zhao et al. (2019) also reported that the path length distributions are independent of the kinetic energy in the 81 impulsive electron events investigated.

Comparison of the path length distributions of different species

Next, we compare the path length distribution of different species at distances 0.2 and 1 AU. We actually calculated the path length distribution for 4 distances, namely 0.2, 0.3, 0.5 and 1 AU but only the results for 0.2 and 1 AU are presented. Ten thousands electrons and protons are injected in the ecliptic plane with initial random pitch angles and 10,000 field lines that originated on the ecliptic plane are also followed. Both electrons and protons have the same initial kinetic energies, $K.E. = 100$ MeV. Furthermore, we fitted Gaussian curve to each distribution.

Figure 3.8 and Figure 3.9 present the calculated path length distributions of 10,000 magnetic field lines, blue, 10,000 electrons, red, and 10,000 protons, green, at 0.2 and 1 AU, respectively. Table Table 3.2 compares the mean, μ , and standard deviation, σ , values of electrons and protons at 0.2 and 1 AU. The mean and standard deviation values of the non-Gaussian distributions are not included.

Figure 3.8 and Figure 3.9 and table Table 3.2 clearly show that:

At distance 0.2 AU (< 0.5 AU), for all $V_{rms} < 1.0$ km/s, both electrons and protons distributions are non-Gaussian and slightly different but the peak is exactly the same. For $V_{rms} \geq 1.0$ km/s, both particles distributions are Gaussian and very close to each other. Moreover, the μ values are exactly the same and the difference in the σ values are < 0.01 AU.

At distance 1 AU (≥ 0.5 AU), for all rms speeds the distributions are Gaussian and almost identical. Moreover, the μ are exactly the same and the difference in the σ s are < 0.01 AU.

At these high energies, curvature and gradient drifts are significant and energetic particles leave the original field line instantly. However, the drifts depends on

charge-mass ratio, Dalla et al. (2013) and Marsh et al. (2013), which means that the protons experience more displacement due to drifts than the electrons. Even though, we expect to see a substantial difference in the path length distributions because of different charge-mass ratio and different gyro-radius, the distribution remains the same for distances 0.5 AU and more. Even for 0.2 AU where there was a small change in the distribution, the standard deviation and mean values are the same which means the path length distribution is also independent of species.

Table 3.2: The mean and standard deviations of path length distributions of energetic electrons (μ_e, σ_e) and energetic protons (μ_p, σ_p). Energy of the electrons and protons are 100 MeV.

R(AU)	V_{rms} (km/s)	μ_e (AU)	σ_e (AU)	μ_p (AU)	σ_p (AU)
0.2	0.3	—	—	—	—
0.2	0.6	—	—	—	—
0.2	1.0	0.199	0.051	0.199	0.044
0.2	2.5	0.201	0.061	0.200	0.056
1.0	0.3	1.171	0.106	1.170	0.105
1.0	0.6	1.186	0.153	1.185	0.157
1.0	1.0	1.216	0.202	1.214	0.202
1.0	2.5	1.343	0.361	1.336	0.355

Variation of the path length distribution of the electrons with V_{rms} at different distance from the Sun

It was noted in Pei et al. (2006) that V_{rms} can be as large as 10 km/s. If V_{rms} is large, it will affect the path length of the field and the electrons. By comparing to observations from Zhao et al. (2019), one can obtain constraints on V_{rms} . Six different V_{rms} values are tested. These are 0.3, 0.6, 1.0, 1.5, 2.0, and 2.5 km/s. For each V_{rms} , we consider five distances 0.2, 0.5, 1.0, 2.0 and 3.0 AU from the Sun for electrons and magnetic field lines. We have therefore a total of 30 cases. The results are shown in Figure 3.10 to Figure 3.14. Blue curves in these figures correspond to the distribution of magnetic field line path length and the red curves correspond to distributions of electron path length. The dashed black lines in all panels are the

Gaussian fits. The mean, μ , and the standard deviation, σ , of the fitted Gaussian distributions can be found in Table 3.3. The mean and standard deviations of the non-Gaussian distributions are left empty in the table.

Below we discuss these results:

Figure 3.10 corresponding to $R = 0.2$ AU.

Field line path length distribution: For cases with $V_{rms} \leq 1.0$ km/s, the Gaussian fits are valid as can be seen from the Shapiro-Wilk test: the p -values in these cases are larger than 0.05, indicating that the Gaussian fit are acceptable. For cases where $V_{rms} \geq 1.5$ km/s, the p -values are less than 0.05 so that the Null Hypothesis is rejected and the distributions are non-Gaussian. The mean values for the three cases where $V_{rms} \leq 1.0$ km/s are the same, 0.197, but the standard deviations show that as the V_{rms} increases, the distributions get broader. In these distributions, the mean path length values are less than 0.2 AU. This is because our starting point is at $r = r_0 \approx 0.046$ AU. Note that close to the Sun, field lines are almost radial.

Electron path length distribution: Shapiro-Wilk test rejects the Null Hypothesis for the cases with $V_{rms} \leq 0.6$ km/s but for cases with $V_{rms} > 0.6$ km/s, the Shapiro-Wilk test suggest that the Gaussian fits are acceptable and as can be seen from the figure, the Gaussian fits agrees better with the data as V_{rms} increases. For $V_{rms} \geq 1.0$ km/s, the mean values are roughly the same but the standard deviations increase with V_{rms} , a manifestation of the fact that the distributions become broader.

Table 3.3: The mean and standard deviations of path length distributions for the meandering field (μ_B, σ_B) and energetic electrons (μ_e, σ_e). Energy of the electron is 100 MeV.

R(AU)	V_{rms} (km/s)	μ_e (AU)	σ_e (AU)	μ_p (AU)	σ_p (AU)
0.2	0.3	0.197	0.016	—	—
0.2	0.6	0.197	0.023	—	—
0.2	1.0	0.197	0.030	0.199	0.051
0.2	1.5	—	—	0.200	0.054
0.2	2.0	—	—	0.200	0.057
0.2	2.5	—	—	0.200	0.061
0.5	0.3	0.519	0.062	0.521	0.057
0.5	0.6	0.519	0.087	0.523	0.072
0.5	1.0	0.520	0.112	0.528	0.093
0.5	1.5	—	—	0.533	0.120
0.5	2.0	—	—	0.540	0.145
0.5	2.5	—	—	0.545	0.167
1.0	0.3	1.165	0.163	1.171	0.106
1.0	0.6	1.169	0.224	1.186	0.153
1.0	1.0	1.175	0.279	1.214	0.202
1.0	1.5	1.189	0.330	1.257	0.257
1.0	2.0	1.201	0.375	1.301	0.308
1.0	2.5	1.224	0.414	1.342	0.355
2.0	0.3	3.072	0.369	3.096	0.193
2.0	0.6	3.084	0.494	3.183	0.288
2.0	1.0	3.118	0.620	3.340	0.380
2.0	1.5	3.187	0.740	3.571	0.485
2.0	2.0	3.260	0.803	3.786	0.572
2.0	2.5	3.438	0.869	4.038	0.657
3.0	0.3	5.939	0.563	5.988	0.246
3.0	0.6	5.949	0.744	6.185	0.378
3.0	1.0	5.975	0.915	6.541	0.514
3.0	1.5	6.108	1.084	7.103	0.667
3.0	2.0	6.310	1.123	7.659	0.773
3.0	2.5	6.623	1.184	—	—

Figure 3.11 corresponding to $R = 0.5$ AU.

Field lines path length distribution: The Null Hypothesis is rejected for $V_{rms} \geq 2.0$ km/s. For $V_{rms} = 0.3$ km/s, the distribution is very well fitted by Gaussian distribution but as V_{rms} increases, the distributions departs from Gaussian.

Electron path length distribution: The Null Hypothesis can not be rejected in any of the distributions except $V_{rms} = 2.5$ km/s but the p -value is decreasing as V_{rms} is increasing. It can be also seen that the difference between fitted curves and data, increases with increase in V_{rms} .

Figure 3.12 corresponding to $R = 1.0$ AU.

Field lines path length distribution: None of the p -values are below 0.05 but the curve fitting shows that as the V_{rms} increases, the distribution deviates from a Gaussian.

Electron path length distribution: Both Shapiro-Wilk test and curve fitting shows that the electrons distributions are nicely Gaussian. Their p -values are higher which means that probability of rejecting Gaussian distribution is really low at 1 AU.

Figure 3.13 and Figure 3.14 corresponding to $R = 2.0$ and 3.0 AU.

Field lines path length distribution: The distributions behave exactly the same as the distributions at 1 AU. Again, the Shapiro-Wilk test does not reject the normality of the distributions, but as seen from the fitted curves, as V_{rms} increases, the distributions depart from a Gaussian distribution.

Electrons path length distribution: The distributions are also the same as those at 1 AU and as the V_{rms} decreases, the distributions are getting closer to Gaussian. The p -values are increasing as well. The only exception is for the case of $R = 3.0$ AU and $V_{rms} = 2.5$ km/s where the Null hypothesis is rejected.

From Table Table 3.3 and Figure 3.10 to Figure 3.14, we find that:

1. At constant R , as V_{rms} increases the means and the standard deviations increase and the distributions are getting significantly wider.
2. At $R \geq 1.0$ AU, the magnetic field distributions are broader than the electrons.
3. At $R = 0.2$ AU, the magnetic field distributions are much narrower than the electron distributions whether they are Gaussian or not.
4. At $R = 0.5$ AU, the mean and standard deviations of magnetic field distributions and electron distributions are close to each other.

The fact that the distributions of the magnetic field path length and the electron path length are quite different (in particular the standard deviation) suggests that the effect of drift is important. Due to drifts, the particle must sample multiple field lines as it propagates out. However, for many cases we consider here, especially those cases with $V_{rms} \leq 1$ km/s, the mean values of the path length for electrons and that for the field lines are close. One may conclude regard that electrons tend to follow field lines.

Zhao et al. (2019) have examined 81 events of which the path length uncertainties < 0.1 AU. The distribution of the electron path length for these events are also reasonably fitted by a Gaussian and the mean and standard deviations of the path length for these events were (1.17 AU, 0.17 AU), (1.11 AU, 0.14 AU), and (1.06 AU, 0.15 AU) when the fraction parameter η were chosen to be 3/4, 1/2, and 1/3 respectively.

By ignoring the variation of V_{sw} in those events and assuming that the solar wind speed was on average 400 km/s, we can compare our simulation results with the observations of Zhao et al. (2019) to put an upper limit on the value of V_{rms} . Take the case of $\eta = \frac{3}{4}$ where the value of the electron path length is 1.17 ± 0.1 AU. This is comparable to our simulation results for the cases of $V_{rms} = 0.3, 0.6,$ and 1.0 km/s. The standard deviation of our simulation results is however, smaller than that obtained in Zhao et al. (2019). One possible reason for this could be that the solar wind speeds in the events considered in Zhao et al. (2019) were within some range while our simulation assumes a fixed $V_{sw} = 400$ km/s.

For a Parker field, i.e., $V_{rms} = 0.0$ km/s, the path length of electrons varies between 1.163 and 1.170 AU, which is also comparable to the results of Zhao et al. (2019). However, the path length distribution of the electrons in a Parker field is not Gaussian-like, as can be seen from Table Table 3.1. Therefore by comparing our results with that of Zhao et al. (2019), we conclude that the range of V_{rms} is likely between 0.3 km/s and 1.0 km/s. Larger values of V_{rms} such as 4.0 or 10.0 km/s as suggested by Pei et al. (2006) can be likely ruled out.

3.3.6 Angular Displacement of electrons

Finally, by tracing field lines back to the source surface, we compute the displacement angle, Θ , between the Parker field line that the electrons are tied to at the beginning and the Parker field line that the electrons follow when they arrive at 1 AU or some other heliocentric distances. Solar rotation effect is removed so that the displacement angle is only due to random footpoint motion. We perform the same

analysis to electron trajectories in a Parker field as well. As can be seen in Figure 3.15, in the case of a Parker field, this displacement is quite small but non-zero because of the curvature drift. As mentioned before, the drifts depend on $m_0\gamma/q$, so the drift for electrons are substantially less than that of the protons of the same kinetic energy. Figure 3.16 compares the distribution of Θ at constant R and different V_{rms} . From panels (a) to (e), we find that as V_{rms} increases, Θ also increases as expected. It is interesting to note that Θ can be as large as 150° for some electrons if $V_g = 2.5$ km/s.

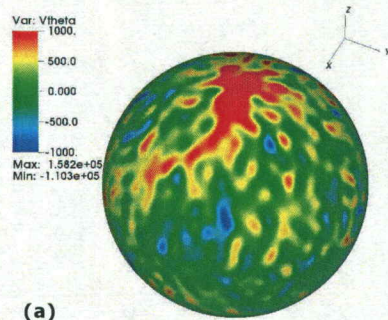
3.4 Conclusion

We examine electron transport in a meandering interplanetary magnetic field. We adopt the framework of Giacalone (2001) in describing the meandering magnetic field. In this formalism, the motion of the footpoint of the interplanetary magnetic field on the source surface is described by a velocity field. The rms speed of the fluctuating surface flow, V_{rms} , characterizes the randomness of the footpoint motion. In examining electron propagation, we ignore pitch angle scattering and thus stay within the regime of the “scattering-free” Wang et al. (2006) scenario. By directly solving the Lorentz equation, we follow single particle motion in a meandering field. We inject ten thousand electrons in both a pure Parker field and the meandering field for six different rms speed, $V_{rms} = 0.3, 0.6, 1.0, 1.5, 2.0$ and 2.5 km/s and obtain the electron path length distributions at five different distances, $R = 0.2, 0.5, 1.0, 2.0$ and 3.0 AU. These distributions are compared with the distributions of path length for ten thousand field lines in each case. Our results can be summarized as follows:

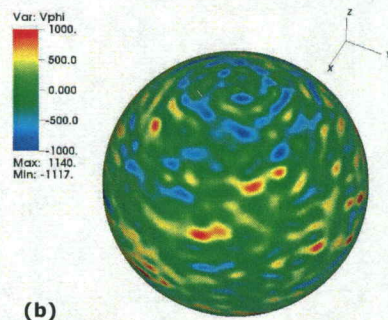
1. The current hypothesis in understanding the propagation of energetic electrons in the solar wind is to assume that electrons are tied to the IMF. Consequently the particle path length should be very similar to that of the magnetic field line path length. However our simulations clearly show that the path length distributions of the fields and electrons are different. In particular, the standard deviations can differ significantly. While the path length distributions for field and electrons are different, the path length distributions for electrons of different energies are almost identical.

2. Depending on the heliocentric distance R and the value of V_{rms} , the path length distributions of electrons and magnetic field lines sometimes can be approximated by a Gaussian distribution. In particular, at 1 AU, a Gaussian distribution describes well both for the field line path length and the electron path length distributions. The mean and standard deviations increase with V_{rms} . Our results for the electron path length distribution at $R < 1$ AU can be useful in understanding future Parker Solar Probe observations. We note that for smaller R , the “scatter-free” approximation is more accurate.

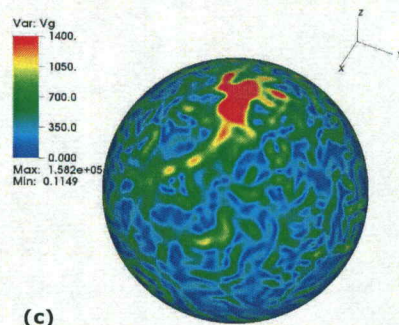
3. By comparing the mean and the standard deviation of the electron path length distributions from our simulation to that from observations Zhao et al. (2019), we suggest that the upper limit of V_{rms} is ~ 1.0 km/s. Higher values as 4 km/s or larger as discussed in Pei et al. (2006) will lead to very large electron path length, inconsistent with observations by Zhao et al. (2019). Note that the presence of scattering will lead to a larger path lengths. Therefore, our upper limit of V_{rms} of ~ 1.0 km/s is likely conservative. In a future paper, we will investigate how including pitch angle scattering will affect the path length distribution.



(a)



(b)



(c)

Figure 3.1: The source surface flows (a) V_θ , (b) V_ϕ and (c) $V_g = \sqrt{V_\theta^2 + V_\phi^2}$. Color bar for panels (a) and (b) are from -1000 to 1000 m/s. Color bar for panel (c) is from 0 to 1400 m/s. $V_{rms} = 0.6$ km/s, $T_c = 2$ days and $N = 50$.

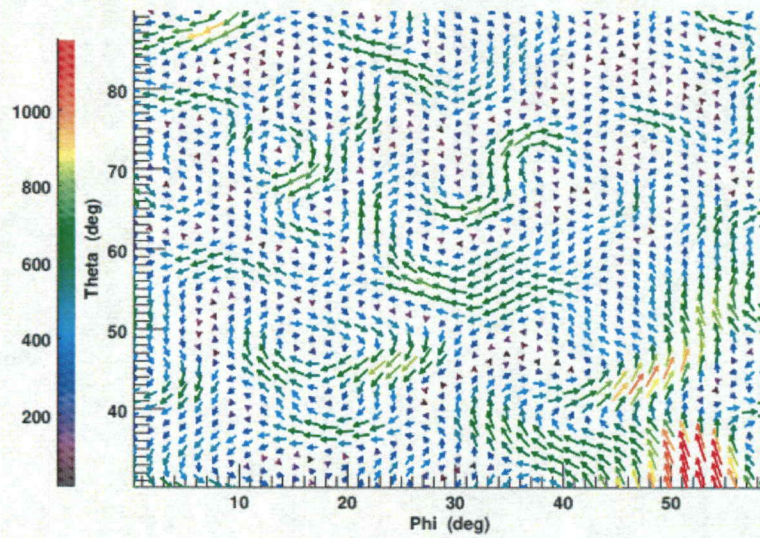


Figure 3.2: The vector surface flow map. The arrows show the flow direction. And the color bar shows the magnitude of the speed. $V_{rms} = 0.6$ km/s, $T_c = 2$ days and $N = 50$.

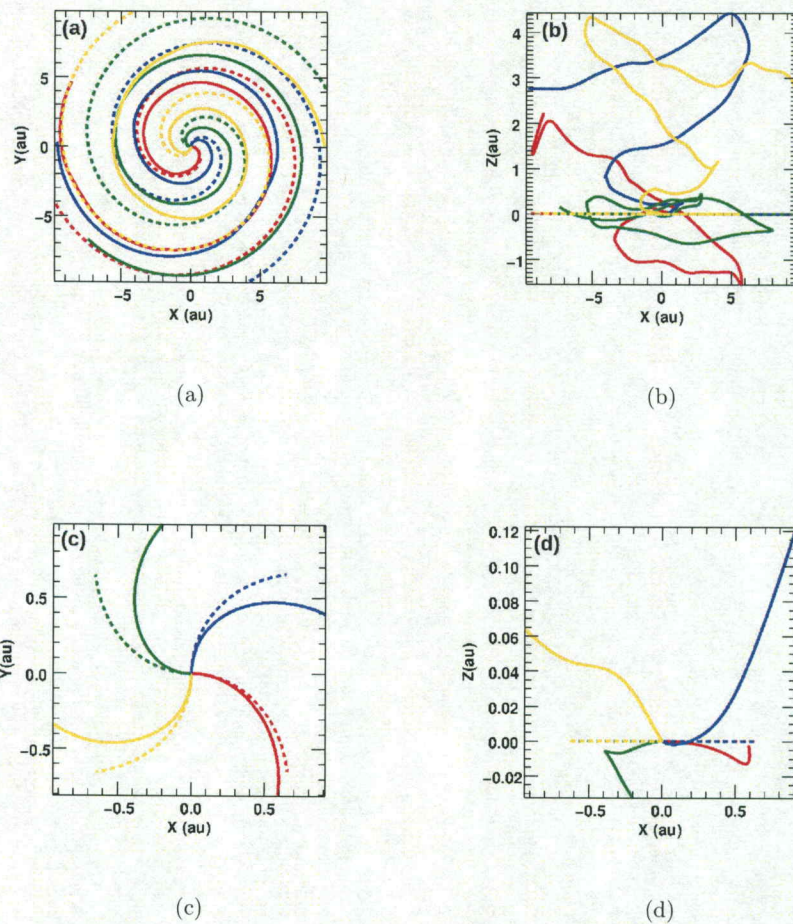


Figure 3.3: The meandering magnetic field lines in the Giacalone (2001) model. $V_{rms} = 0.6$ km/s, $T_c = 2$ days and $N = 50$. Solid lines are the meandering field lines and dashed lines are the Parker field lines. Panel (a) and (b) are projections in the XY, and XZ planes when the field lines are traced to $R = 10$ AU; Panels (c) and (d) are close ups of (a) and (b) where the field lines are only traced to $R = 1$ AU. In all figures, the same color field lines (Parker or the meandering field lines) start from the same locations.

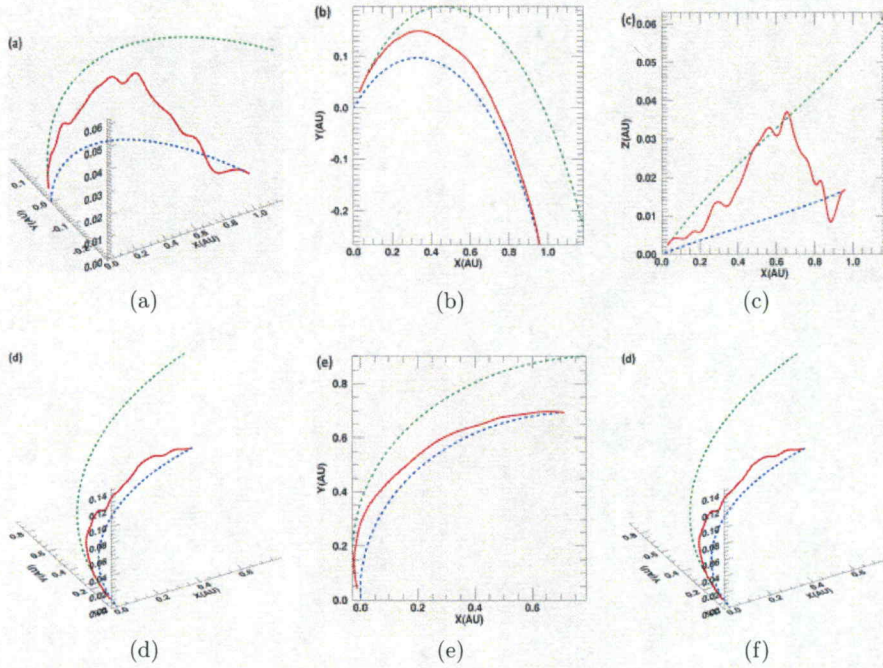
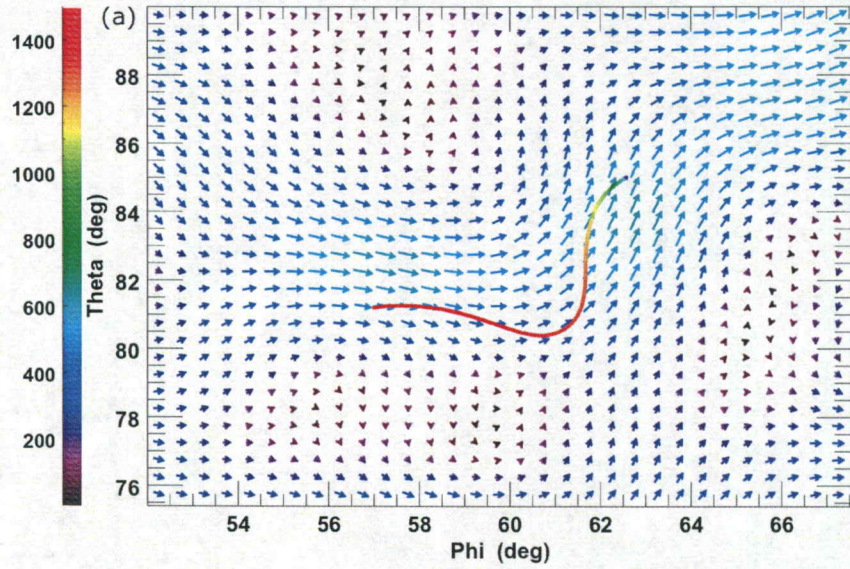
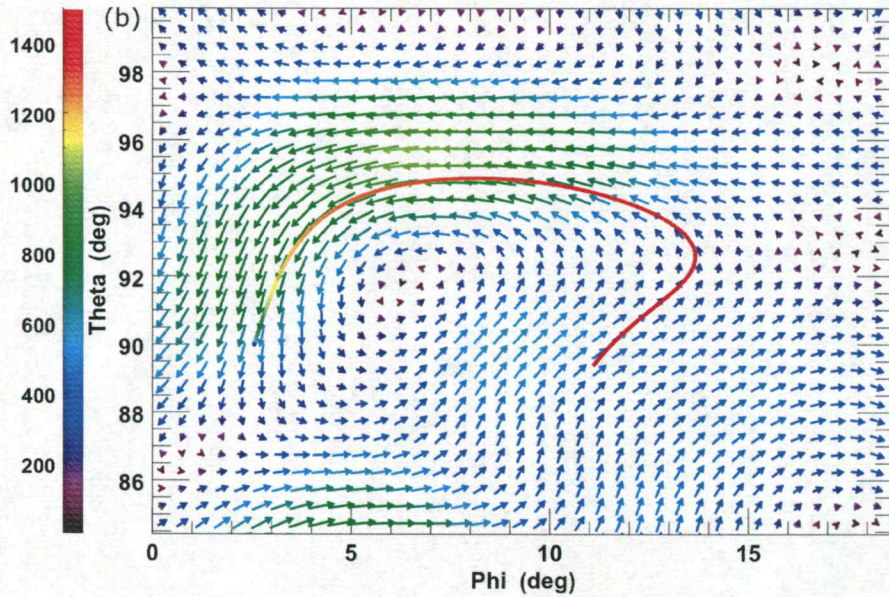


Figure 3.4: Two examples of electron trajectories in the meandering field. (a) and (d): trajectories in 3D, (b) and (e): projection of the trajectories in the XY plane; (c) and (f): projection of the trajectories in the XZ plane. In all panels, the solid Red lines are the electrons trajectories; the dashed green lines are the Parker field lines the electrons initially tie to; and the dashed blue lines are the Parker field lines the electrons tie to at 1 AU. $V_{rms} = 0.6$ km/s, $T_c = 2$ days and $N = 50$. The angular displacement between the initial and the final Parker field lines are $\sim 10^\circ$.



(a)



(b)

Figure 3.5: The footpoint trajectory of two electrons from two different starting points, multi-colored solid line. The color bar is corresponding to the surface flow vectors magnitude. Purple in the solid line is the footpoint at $t = 0$ sec and red is the footpoint at the end of the trajectory.

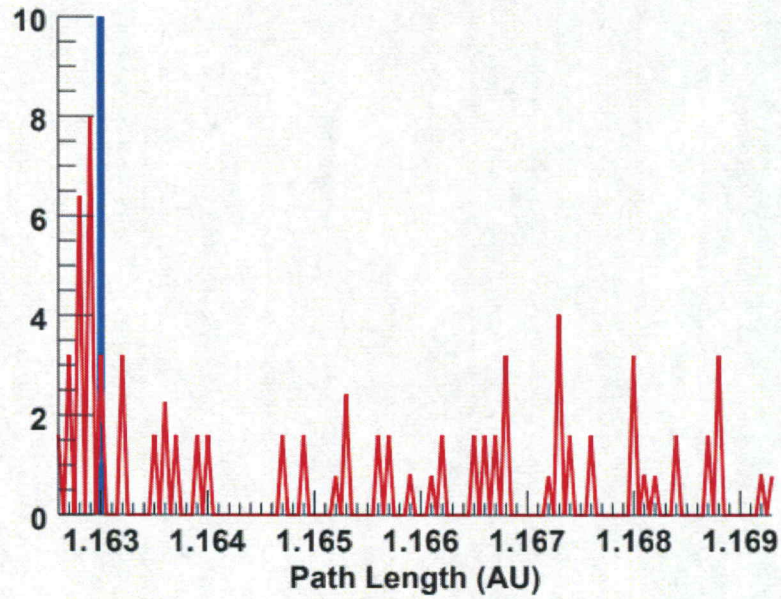


Figure 3.6: Histogram of path length distribution of 10,000 electrons in a Parker field. $V_{SW} = 400$ km/s is assumed. The path length of Parker field is 1.163 AU, shown here as the blue vertical line, which represent a δ -function type distribution. The Red lines show the electron path lengths. It has a small range from slightly smaller than 1.163 AU to 1.170 AU. This small range is due to curvature drift and difference in initial pitch angle. The y-axis unit is arbitrary.

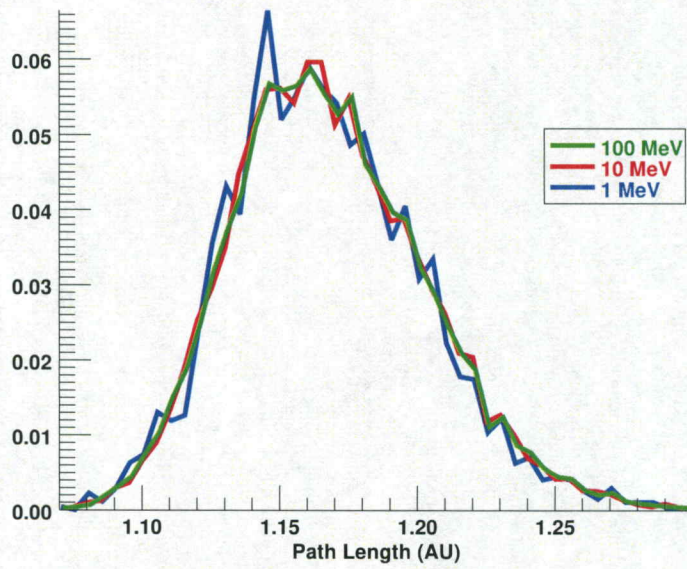


Figure 3.7: Histogram of path length distribution of 10,000 electrons in a meandering field for three different kinetic energy, 1, 10 and 100 MeV at 1 AU. The blue, red and green lines are path length distributions of 1, 10, 100 MeV electrons, respectively. The rms speed of fluctuations are chosen as Giacalone (2001), $V_{rms} = 0.6$ km/s. Note that in this figure source surface is put at 10 solar radii.

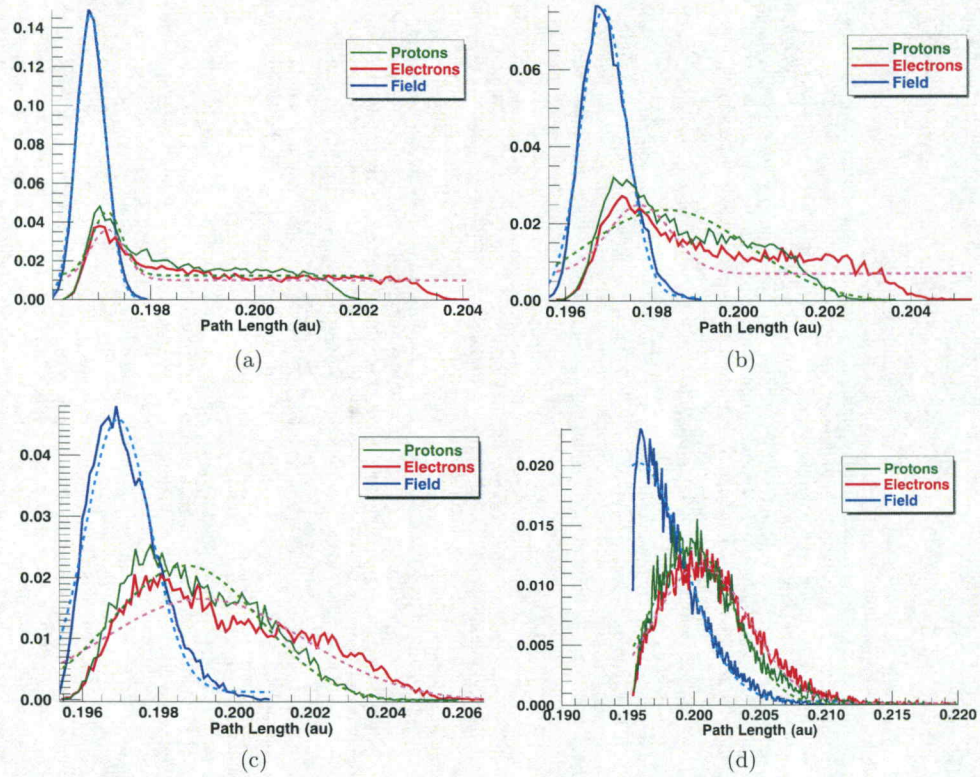


Figure 3.8: Path length distributions for both the field line (in blue) and electrons (in red) when $R = 0.2$ AU: (a) $V_{rms} = 0.3$ km/s, (b) $V_{rms} = 0.6$ km/s, (c) $V_{rms} = 1.0$ km/s, (d) $V_{rms} = 2.5$ km/s. The curves are fitted by a Gaussian functional form.

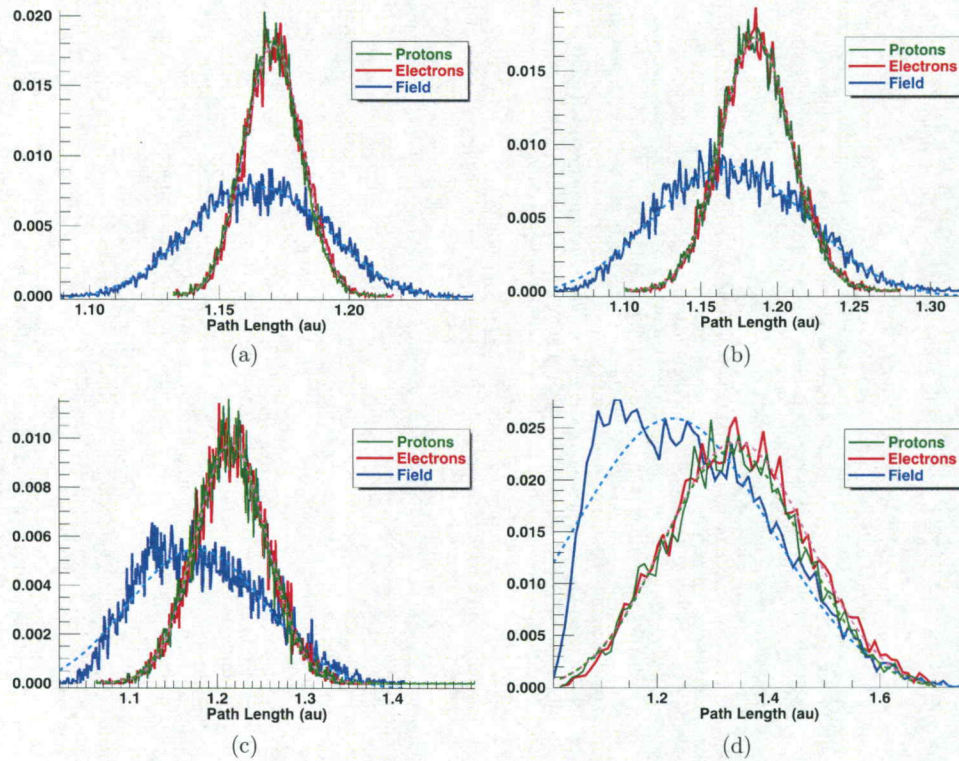


Figure 3.9: Same as Figure 3.8 but for $R = 1$ AU

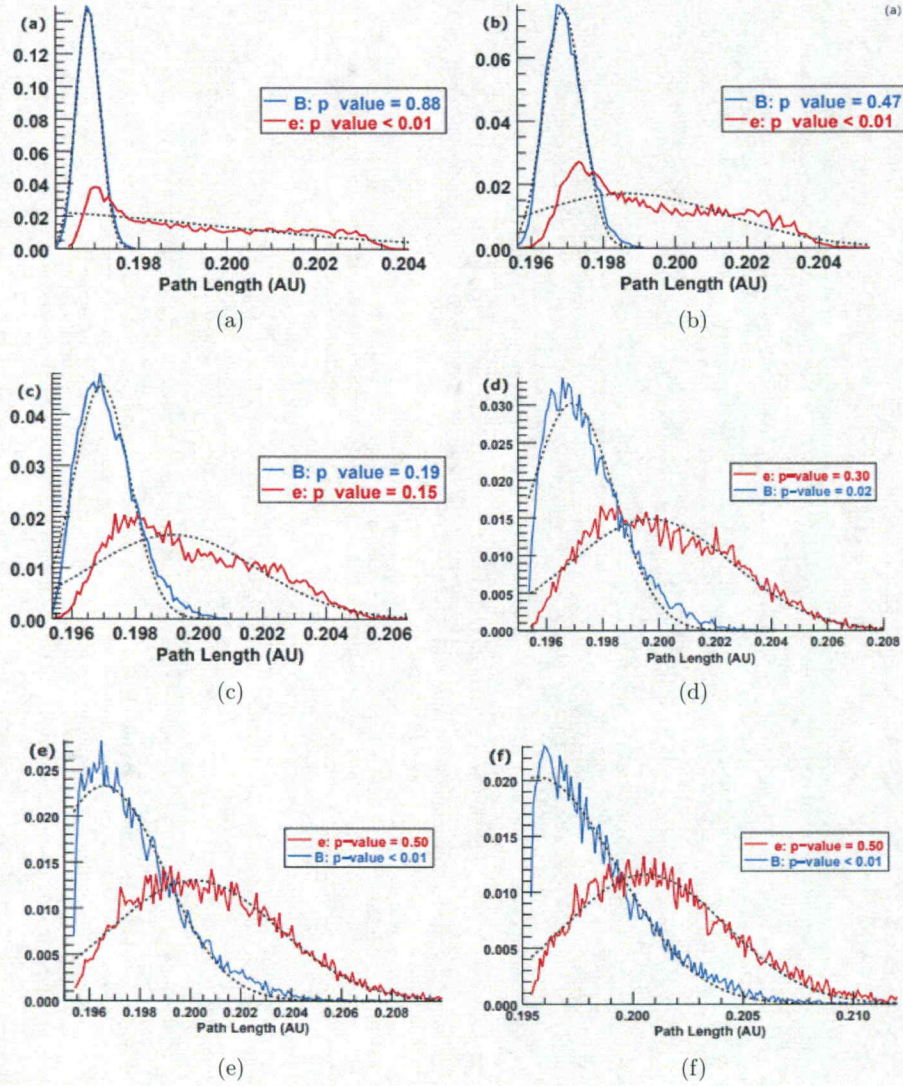


Figure 3.10: Path length distributions for both the field line (in blue) and electrons (in red) when $R = 0.2$ AU: (a) $V_{rms} = 0.3$ km/s, (b) $V_{rms} = 0.6$ km/s, (c) $V_{rms} = 1.0$ km/s, (d) $V_{rms} = 1.5$ km/s, (e) $V_{rms} = 2.0$ km/s, (f) $V_{rms} = 2.5$ km/s. The curves are fitted by a Gaussian functional form and shown in the legends are the p -value obtained from the Shapiro-Wilk test. Distributions with p -values higher than 0.05 are Gaussian.

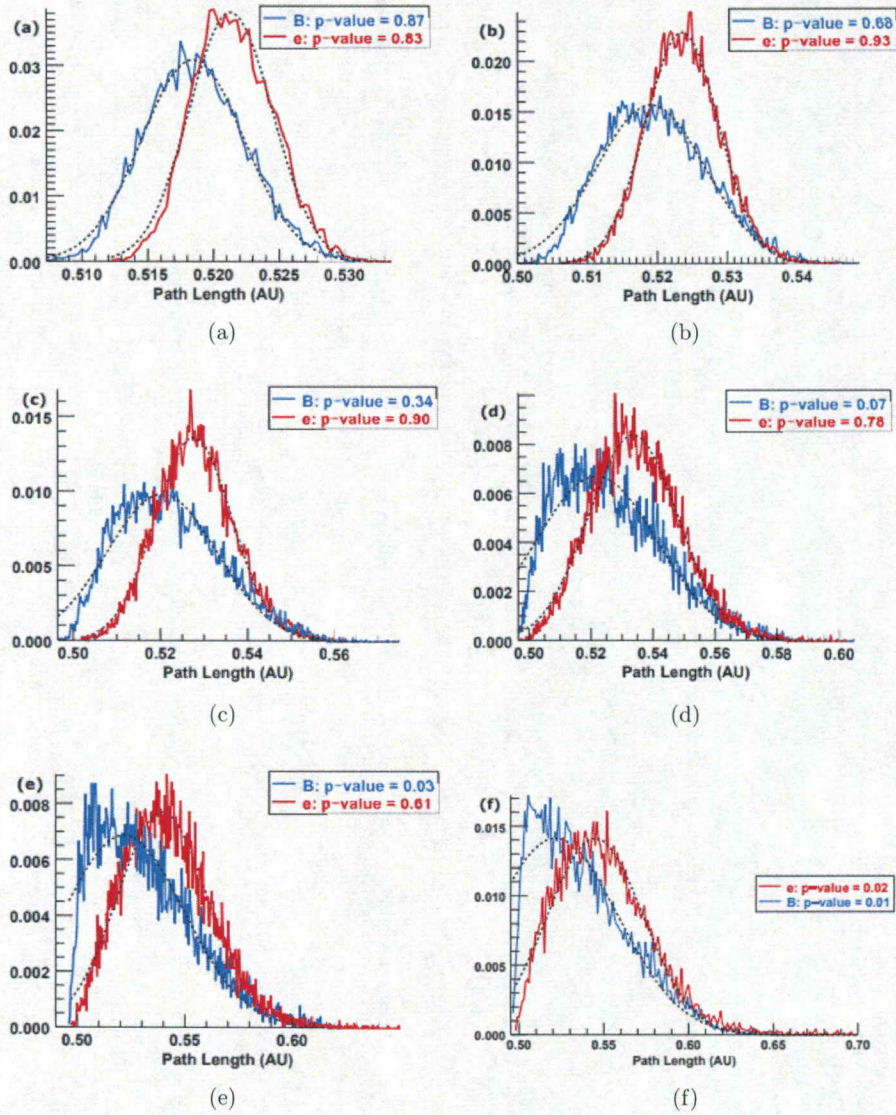


Figure 3.11: Same as Figure 3.10, but for $R = 0.5$ AU.

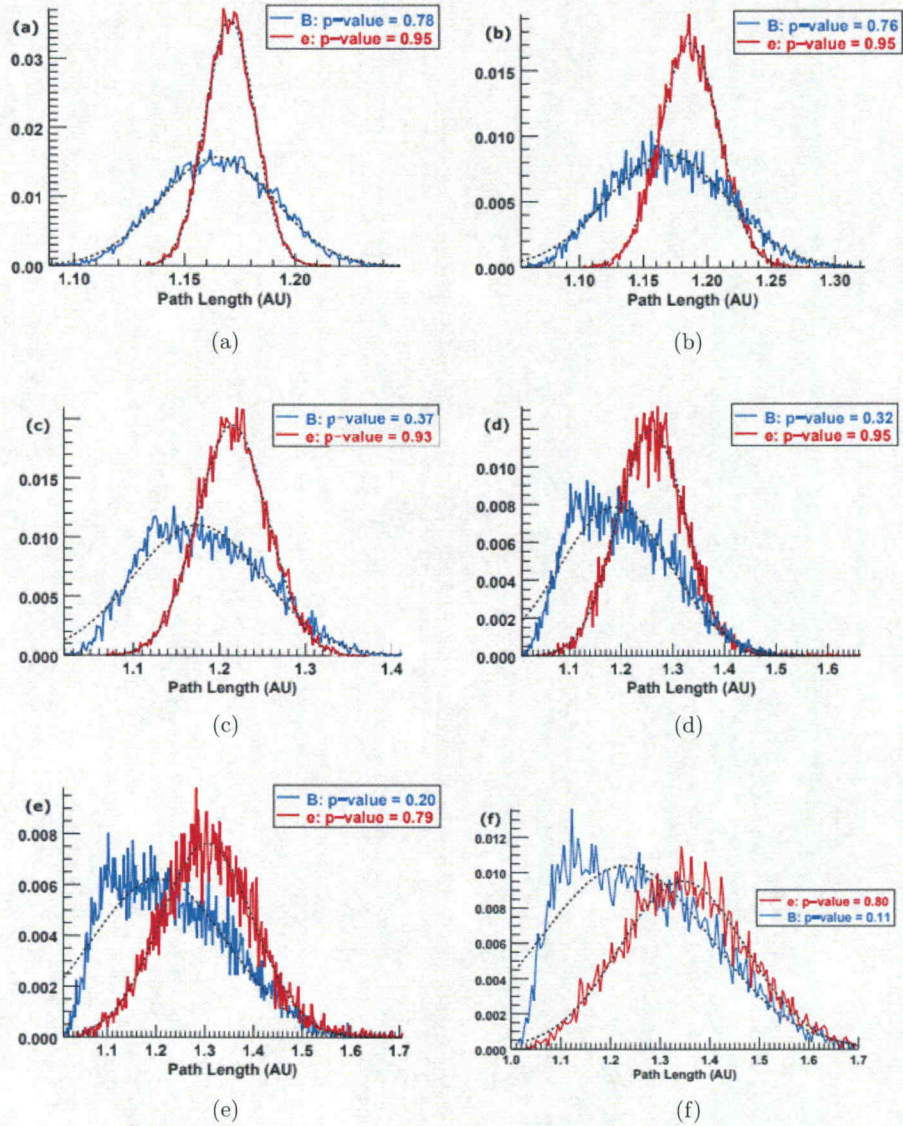


Figure 3.12: Same as Figure 3.10, but for $R = 1.0$ AU.

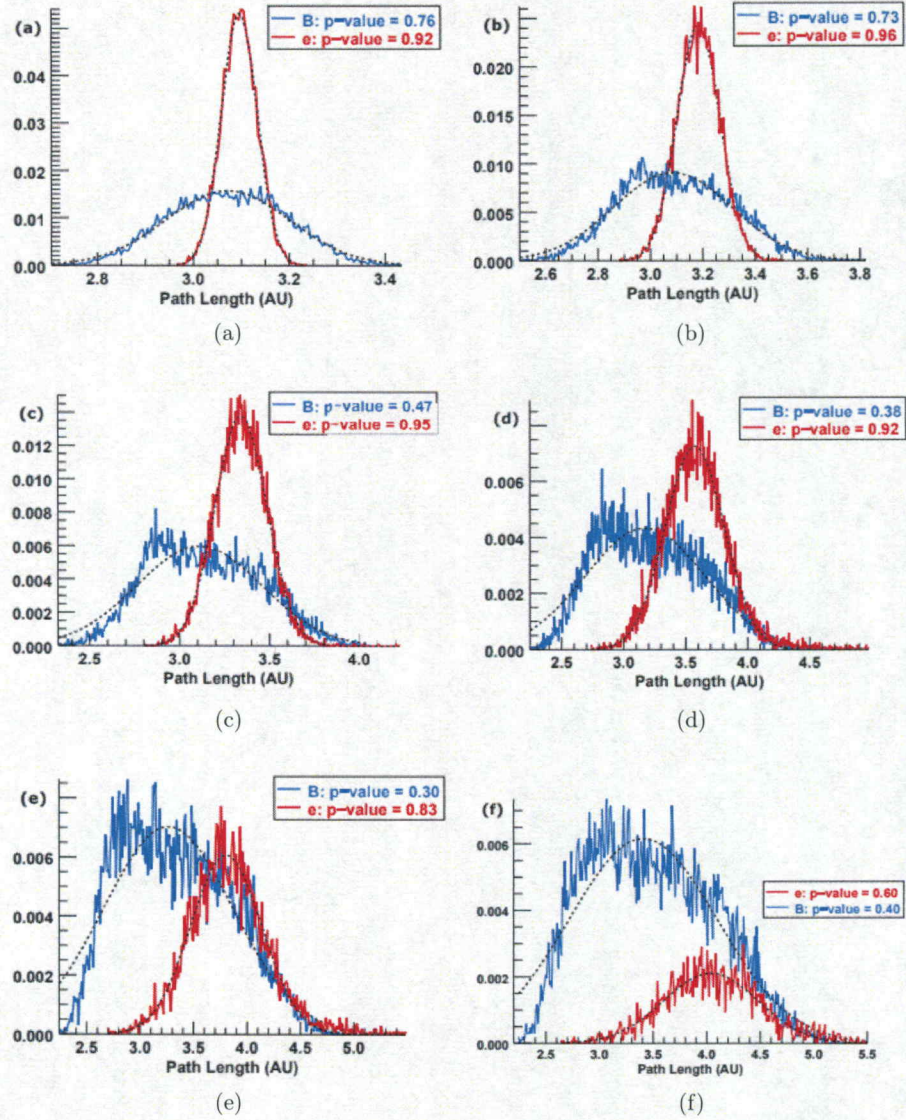


Figure 3.13: Same as Figure 3.10, but for $R = 2.0$ AU.

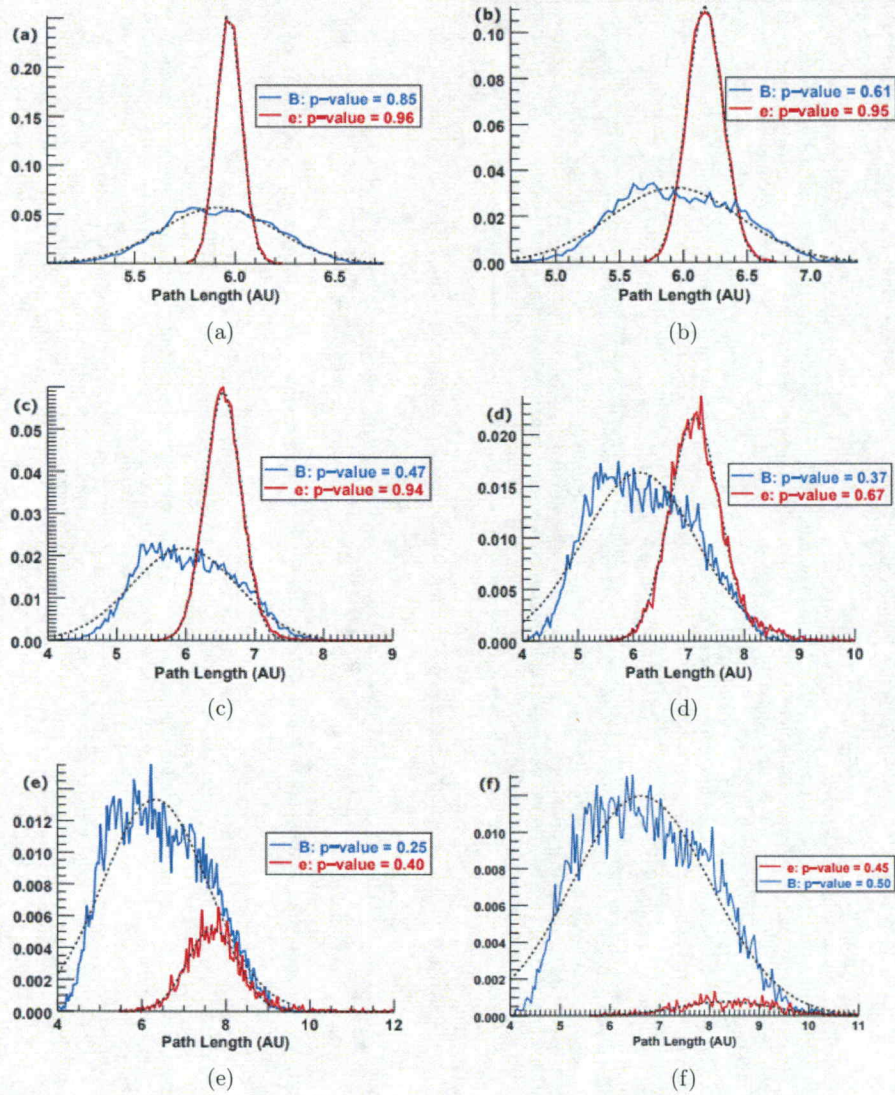


Figure 3.14: Same as Figure 3.10, but for $R = 3.0$ AU.

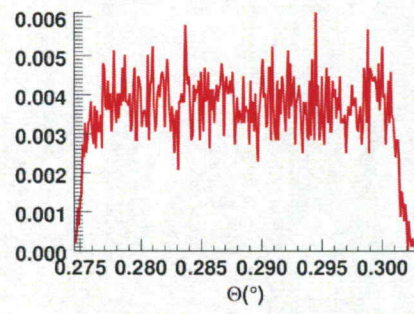


Figure 3.15: The distribution of the angular displacement of electron in Parker field.

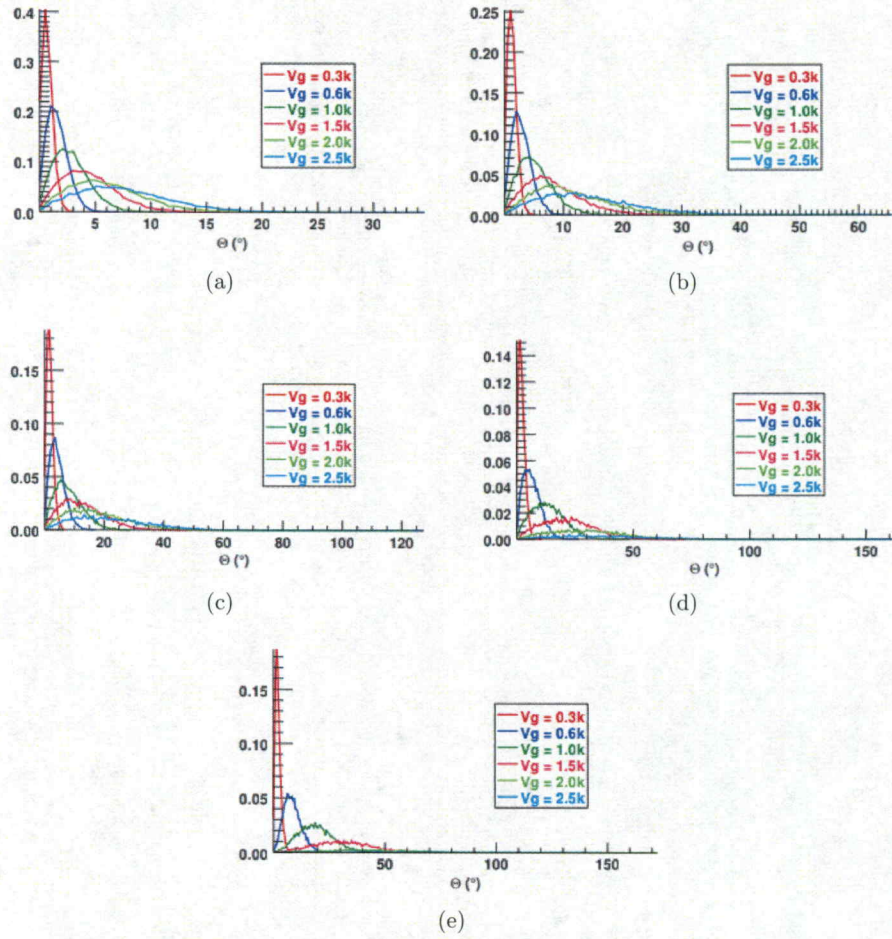


Figure 3.16: Same as Figure 3.15, but for electrons in meandering fields. (a) $R = 0.2$, (b) $R = 0.5$, (c) $R = 1.0$, (d) $R = 2.0$, (e) $R = 3.0$ AU. Example of electron trajectories are shown in Figure 3.4.

CHAPTER 4

HATHAWAY'S MODEL

4.1 Introduction

As it is mentioned in Chapter 3, Giacalone (2001) modeled the supergranular flow by only considering divergence-free advecting flow. However, inside supergranules, hot gas rises in the center, moving horizontally to the borders and sinks in the border; the horizontal speed in the center is the maximum and at the border is zero, see Section 1.2. This flow is not a divergence-free flow. Even though the Giacalone (2001) model is divergence-free, we can assume that the areas with lower horizontal speed as the supergranules border and we can estimate the size of supergranules.

By comparing the size of supergranules in the photospheric maps of Giacalone (2001), Figure 3.1c, and the typical supergranules size, 30 Mm or 2.5° , it is clear that the sizes are significantly larger than supergranule cell sizes. This is expected because the number of spherical harmonic modes in Giacalone (2001) does not exceed 100. On the other hand, the maps in Giacalone (2001), Figure 3.1, clearly shows that the values of latitudinal and longitudinal velocities are too high, especially in the latitudinal direction. As it was mentioned in Chapter 3, there isn't any mechanism on the photosphere that induces such high advecting velocities except granules. The

meridional flows are 20 m/s and the other contribution to latitudinal advecting flow is from the latitudinal component of the supergranular flows. Moreover, the observations show that the maximum horizontal velocity in the supergranules is 500 m/s. In the azimuthal direction the photospheric velocities are also too high; there is not any mechanism that can cause such high speeds except granules. Moreover, the granules do not have any effects on the movement of the open magnetic flux tubes as is discussed in Chapter 5.

Hathaway (1987) introduced a model to simulate the advecting flows on the photosphere and it was developed by Hathaway (1988), Hathaway (1992), Hathaway et al. (2000), Hathaway et al. (2010), Hathaway (2012) and Hathaway et al. (2015). In this chapter, we adopt a modified version of Hathaway's model. We describe Hathaway's velocity spectrum and the changes made to improve the velocity spectrum from Hathaway (1988) to Hathaway et al. (2015) in Section 4.2. In Section 4.3, the generated surface flow maps, generated magnetic field lines, the motion of the footpoints on the source surface and the trajectory of the solar energetic particles will be discussed. Finally, in Section 4.3.5, the conclusion of this model will be discussed.

4.2 Model Description

Hathaway (1988) introduced a vector velocity field to model the advecting flows on the surface of the photosphere. This velocity field has 3 components, radial flow (upward and downward w.r.t. to the photosphere), poloidal flow (latitudinal) and toroidal flow (longitudinal).

In order to define a velocity spectrum on a sphere, spherical harmonic functions can be used as the basis. The normality of the spherical harmonic functions gives the ability to separate each surface flow depending on the characteristics of the flow. For each surface flow, we can assign a set of modes, for instance, axisymmetric flows (solar rotation, differential rotation and meridional flows) can be described by a set of $m = 0$ modes and non-axisymmetric flows by a set of $m \geq 1$ modes (supergranular, granular and giant cells).

$$V_r(\theta, \phi) = \sum_{l=1}^{L_{max}} \sum_{m=-l}^l R_l^m Y_l^m(\theta, \phi) \quad (4.1a)$$

$$V_\theta(\theta, \phi) = \sum_{l=1}^{L_{max}} \sum_{m=-l}^l \left[S_l^m \frac{\partial Y_l^m(\theta, \phi)}{\partial \theta} + T_l^m \frac{1}{\sin(\theta)} \frac{\partial Y_l^m(\theta, \phi)}{\partial \phi} \right] \quad (4.1b)$$

$$V_\phi(\theta, \phi) = \sum_{l=1}^{L_{max}} \sum_{m=-l}^l \left[S_l^m \frac{\partial Y_l^m(\theta, \phi)}{\partial \phi} - T_l^m \frac{1}{\sin(\theta)} \frac{\partial Y_l^m(\theta, \phi)}{\partial \theta} \right] \quad (4.1c)$$

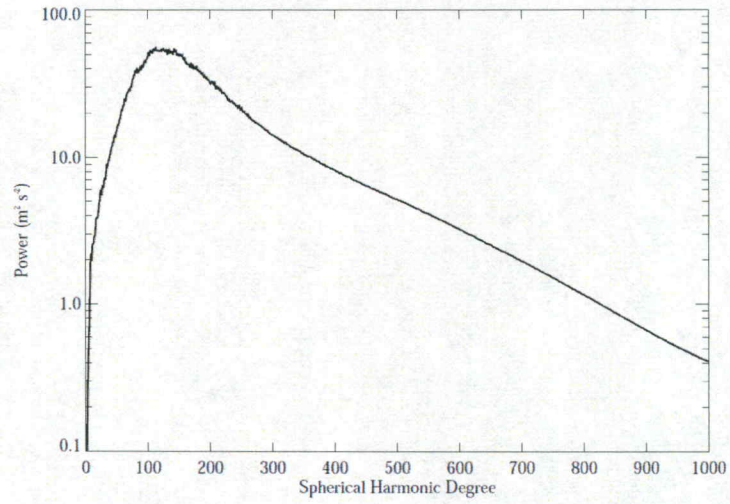
where θ is the colatitude and ϕ is the longitude. R_l^m , T_l^m and S_l^m are complex spectral coefficients for radial, toroidal and poloidal flow components, respectively. Note that the poloidal and toroidal equations are coupled.

Hathaway (1988) collected numerous data sets of full-disk Doppler images from Global Oscillation Network Group (GONG) and the Solar Oscillator Imager (SOI) on the Solar and Heliospheric Observatory (SOHO) which were used to estimate the spectral coefficients R_l^m , T_l^m and S_l^m . Moreover, Hathaway (1988) constructed simulated Doppler images from the estimated spectral coefficients using Equation 5.1. Hathaway (1988) included solar rotation, differential rotation, meridional flows, giant

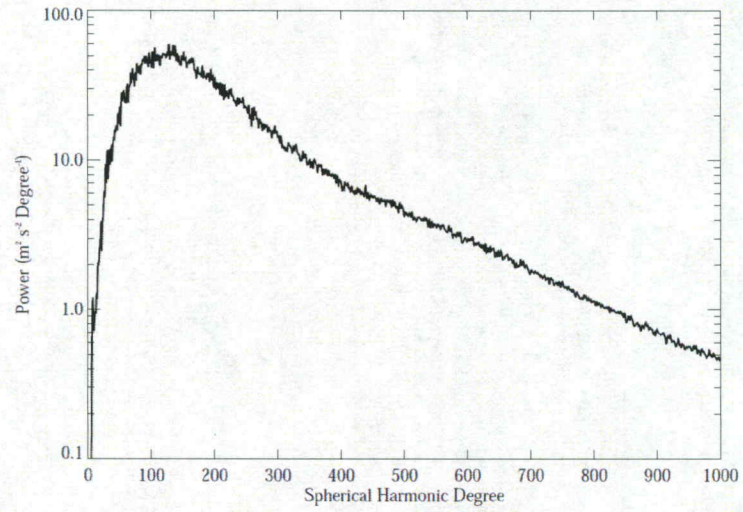
cells and supergranule cells in the flow spectrum. The rigid rotation was corresponding to spherical mode $(l, m) = (1, 0)$ with average velocity 1569.6 m/s, differential rotation was corresponding to $(l, m) = (3, 0)$ and $(5, 0)$ and meridional flows were corresponding to $(l, m) = (2, 0)$ and $(4, 0)$. Note that meridional flows are streaming from the equator to poles. For non-axisymmetric flows such as giant cells and supergranule cells, a broader spectrum was needed. Giant cells were corresponding to the modes $l = 1 - 24$ which peaked at $l \sim 12$. The Modes for supergranules were corresponding to $l = 70$ to 230 in which the peak was at $l \sim 150$. However, Hathaway (1988), ignored the tilt angle of the Sun's rotation axis toward and away from the observer.

Hathaway (1992) added the tilt angle correction and supergranules corresponding modes were extended to $l_{max} = 512$ which peaked at $l \sim 100$. Hathaway et al. (2000) extracted the spectral coefficients from Michelson Doppler Imager (MDI) on the SOHO by the same analysis. The included modes were increased to 1000 modes. The average power spectrum of new obtained spectral coefficients, ($l = 1$ to 1000) was generated and compared with the average observed power spectrum obtained from MDI data, Figure 4.1.

As can be seen, there is a peak at $l = 120$ which belongs to supergranule cells. Hathaway et al. (2000) expected to see a peak for mesogranule cells at $l \sim 600$ and another peak for Giant cells at $l < 30$. However, there are no such peaks in the power spectrum, Figure 4.1. Hathaway et al. (2000) concluded that mesogranules and giant cells do not have distinct modes, unlike supergranules, but this will not deny their



(a)



(b)

Figure 4.1: The power spectrum of (a) the observed by MDI data, (b) the simulated power spectrum by the extracted spectral coefficients.

existence. Hathaway et al. (2000) also concluded that the modes corresponding to granule convecting cells have to be at $l > 1000$.

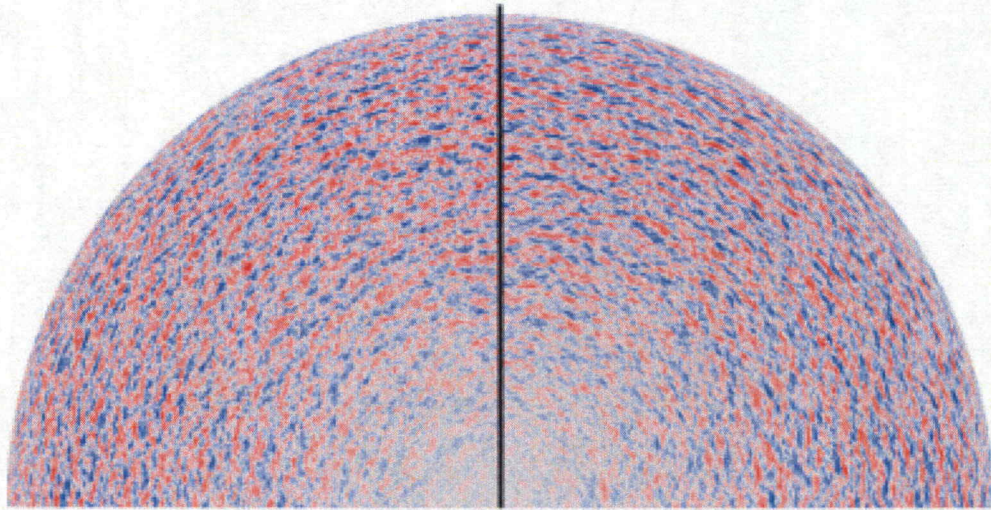


Figure 4.2: The Doppler image of the line of sight. Right: The simulated Doppler image from updated spectral coefficients. Left: The observed Doppler image by MDI, Hathaway et al. (2010)

Hathaway et al. (2002), discovered that the typical non-axisymmetric flow velocities on the photosphere are 300 m/s which are mostly due to supergranular flows and Hathaway et al. (2010), again, analyzed MDI data, obtained the granular flow spectrum which was peaked at $l \sim 4000$. Hathaway et al. (2010) created the Doppler image of the line of sight by applying the updated spectral coefficients, R_l^m , T_l^m and S_l^m . Figure 4.2 shows the comparison between the simulated and the MDI Doppler image of the line of sight. The right side is the simulated Doppler image and the left side is observed Doppler image by MDI. As can be seen, the two sides are remarkably similar and indistinguishable.

A time-dependent vector velocity field can be modeled by making the spectral coefficients, time dependent. Hathaway et al. (2010) assumed that differential rota-

tion and meridional flows advect the non-axisymmetric flows such as supergranules, granules, and giant cells. By this assumption, the advection equation can be solved for each spherical harmonic mode to find the time evolution of spectral coefficients, R_l^m , S_l^m and T_l^m .

$$\frac{\partial w}{\partial t} = -\frac{V(\theta)}{r} \frac{\partial w}{\partial \theta} - \frac{U(\theta)}{r \sin \theta} \frac{\partial w}{\partial \phi} \quad (4.2)$$

where w represents the velocity components $w \in (V_r, V_\theta, V_\phi)$, $V(\theta) = -V_0 \cos(\theta) \sin(\theta)$ represents meridional flow and

$$U(\theta) = r \sin(\theta) \Omega(\theta)$$

denotes differential rotation where $\Omega(\theta) = \Omega_0 + \Omega_2 \cos^2(\theta) + \Omega_4 \cos^4 \theta$. As was mentioned above, w is a set of spherical harmonics with individual spectral coefficients for each mode. Moreover, the equations for the components V_θ and V_ϕ , Equation 5.1 b and c, are coupled. Using the orthogonality of spherical harmonics, equations are multiplied by the complex conjugate of spherical harmonics and integrated over in space to separate modes and equations. Unfortunately, because the Equation 5.1 b and c contain $1/\sin \theta$ and also the first derivative of θ , some of the integrals do not vanish and making it impossible to find the spectral coefficients, S_l^m and T_l^m . In this research, instead, we change the photospheric maps every 24 hours. This can be plausible since we only include the supergranule modes, $l \leq 512$, with a lifetime of one day and do not include granules with an average lifetime of 10 minutes; the maps are also slow varying in time.

Hathaway et al. (2015) analyzed the full-disk Doppler images observed by Helioseismic and Magnetic Imager (HMI) on the Solar Dynamic Observatory (SDO). HMI data also showed that the supergranular flows peaked at $l \sim 120$, size = 35 Mm, and granular flows peaked at $l \sim 3500$, size = 1.2 Mm.

In this study, we are only interested in horizontal flows on the photosphere that is responsible for the random walk of the footpoint so we ignore the radial flows, Equation 5.1a. We are also interested in photospheric convective flows that can displace the open magnetic flux tubes, $l \leq 512$, therefore we ignore granule and mesogranule cells. We received a new set of spectral coefficients from David Hathaway in a private communication that was developed in 2016 and has not been published. In the 2016 model, the modes are from $l = 1$ to 512 which includes supergranules, giant cells, differential rotation, meridional flows.

As mentioned above, in order to include the time evolution of the supergranules, 300 different maps are created and the map is replaced every 24 hours. Note that the solar wind carries the information from the source surface and is traveling with a speed of 500 km/s (in this section we considered the solar wind to be 500 km/s) so it takes 3.5 days for the solar wind to reach 1 AU. 150 maps are assigned for the layers of the solar wind from the source surface to 42 AU at $t = 0$ and the remaining 150 maps are added one by one after every 24 hours, the lifetime of the supergranules. In the current chapter, the source surface is placed, at $10 R_{sun}$ and the photospheric maps are linearly expanded to the source surface. Finally, in this section, all parameters such as B_0 and solar wind speed are adopted from Section 2.1.

4.3 Results and Discussion

4.3.1 Flow Pattern on the source surface

At first, we investigate the flow pattern on the source surface. In the Giacalone (2001) model, see Chapter 3, the number of spherical harmonic modes are 50, there is no concern for the resolution of the map but in the Hathaway's velocity spectrum, $l_{max} = 512$, therefore, we need to estimate the suitable resolution to ensure that the maps present all the structures on the source surface. In this model, the smallest structures are supergranules with a typical size of 30 Mm, 2.5° . The resolution of the maps is chosen to be 0.1° both in the longitudinal and latitudinal directions. Although this resolution is high enough for $l_{max} = 512$, to test our estimations, higher resolution maps, $\sim 0.001^\circ$, are created and compared to make sure that the surface velocity changes monotonically between grid points. Figure 4.3a and b illustrate the magnitude of horizontal velocities, V_θ and V_ϕ , respectively and panel c shows the magnitude of total fluctuating flow $V_g = \sqrt{(V_\theta^2 + V_\phi^2)}$. The modes are from $l = 1$ to 512 representing differential rotation, meridional flows, giant cells and supergranule cells. The color bar on the left top shows the magnitude of V_θ , V_ϕ and V_g . In panels a and b, the color bar range from -500 to $+500$ m/s and in panel c, ranges from 0 to 1000 m/s. As it can be seen in Figure 4.3, the flow speed near poles reaches extremely high values. To avoid the singularity, we limit our simulation to latitudes below $\pm 80^\circ$.

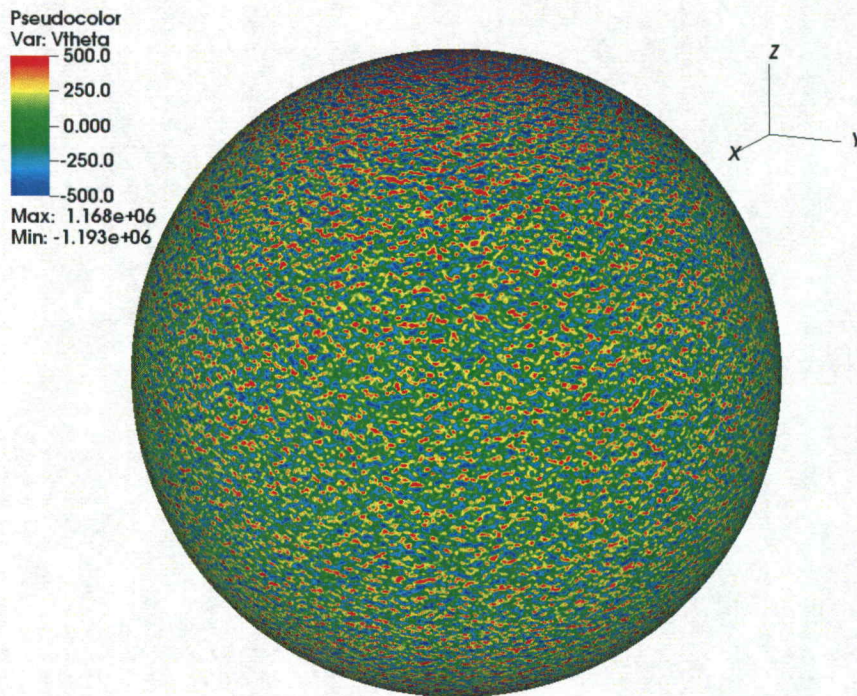


Figure 4.3: (a) V_{θ}

4.3.2 Footpoint motion on the source surface

Next, we investigate the footpoints' motion on the source surface. Note that the term "trajectory of the footpoints" that has been used in Chapter 3 has a different meaning, therefore, in this chapter and chapter 5 the term "Footpoint motion" is used. The footpoints are expected to random walk on the source surface. In this model, the first map is generated at $t = 0$ and we follow the footpoints backward in time.

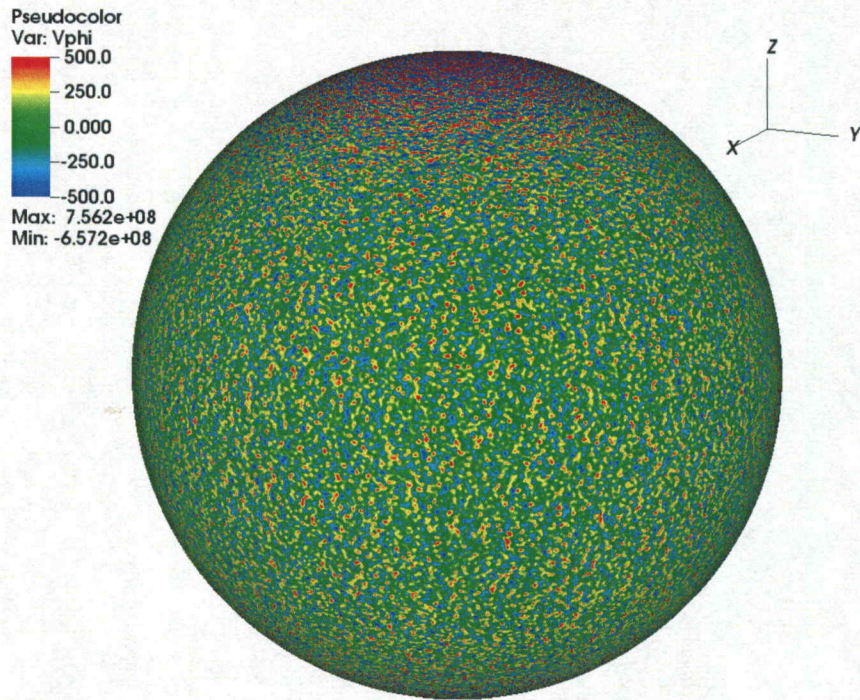


Figure 4.3: (b) V_ϕ

In order to see how the footpoints of the field line from the source surface to the 10 AU changes, we calculate the time it takes for the solar wind to reach 10 AU. In this simulation, $V_{sw} = 500\text{km/s}$ which means solar wind travels 35 days to reach 10 AU. The footpoints are followed from $t = 0\text{s}$ to -35 days. After each day, \sim lifetime of the supergranules, the map is updated to a new map. The footpoints are chosen with different initial latitudes and longitudes. The starting points are chosen

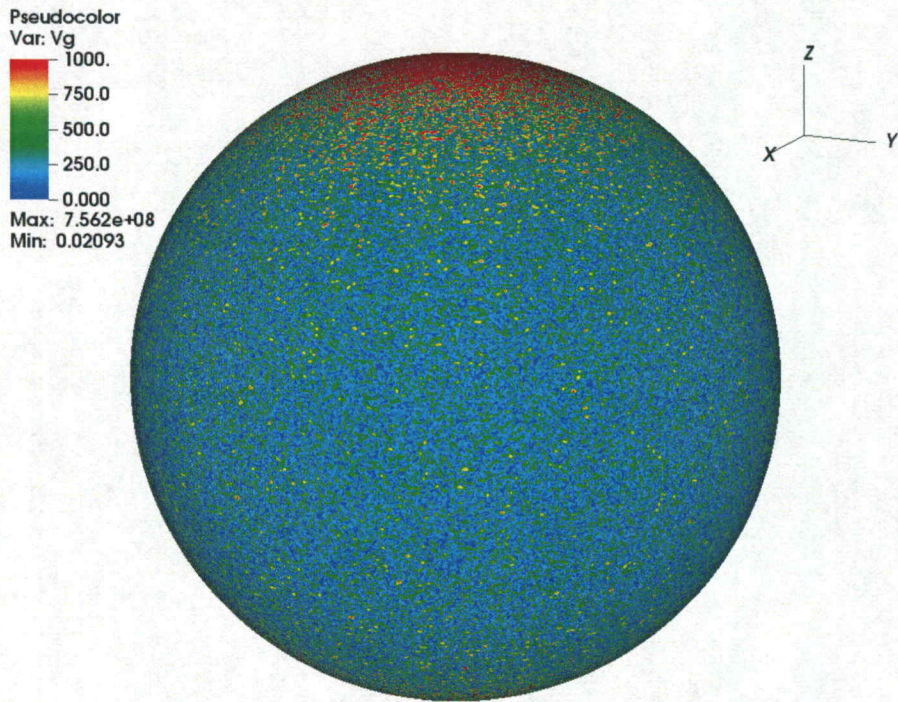


Figure 4.3: (c) V_g . The magnitude of the horizontal velocities on the source surface: (a) V_θ , (b) V_ϕ and (c) $V_g = \sqrt{V_\theta^2 + V_\phi^2}$. The color bar for panel (a) and (b) are from -500 to 500 m/s and 0 to 1000 m/s for panel (c).

for co-latitudes 45, 65, 85 and 90°. In each latitude, 12 equally separated longitude are chosen. Figure 4.4a and Figure 4.4b show the random walk of the footpoint for latitude 45° and in the ecliptic plane, respectively. In each panel, the footpoints trajectories are rotated to start from the same longitude. Moreover, the motion due to solar rotation is omitted to show only the random walk of the footpoints. Each color

corresponds to a different longitude. As expected, the random walk of a footpoint is quite slow and the displacement is mere $\pm 3^\circ$ in both latitudinal and longitudinal direction after 35 days. X-axis is longitude and Y-axis is latitude on the source surface.

4.3.3 Interplanetary Magnetic Field

Next, we examine how the magnetic field lines differ from the previous scheme, Giacalone (2001) model. We linearly expand the Hathaway velocity spectrum to the source surface at $10 R_{sun}$; change the source surface map every 24 hours. The magnetic field lines are followed from the source surface to 7 AU, Figure 4.5a and b, then to 15 AU, Figure 4.5c and d. The field lines in panel a and c, originate from latitude 45° and panel c and d from the ecliptic plane. Moreover, the field lines in all panels are equally separated in longitude. In panel a and b, each dashed line is a Parker field line that originated from the starting point of the same color meandering field line.

Figure 4.5a and b show that the meandering field lines are very Parker-like but quite far from the original Parker field line. At latitude 45° , the field lines look very smooth with no fluctuation, however, the scales of the axes are quite big and the fluctuations are not clear on this large scale.

In panel c and d, all field lines at the same latitudes are azimuthally rotated to start from the same longitude, $\phi = 0$. This rotation allows us to compare the difference between the field lines and to ensure that there is no symmetry. The dashed

green line is the Parker field line that emerges from $\phi = 0$. Panel c and d indicate that the separation between field lines is of the order of multiple AU.

Next, we compare the magnetic field generated by Hathaway's spectrum to the observed data collected by Advanced Composition Explorer (ACE). The magnetic field components (B_r, B_θ, B_ϕ) are calculated for 36000 random points in the GSE coordinates at 1 AU. Figure 4.6 demonstrates the location of the spacecraft and the unit vectors of the GSE coordinates. Then, the histogram of the spiral angle $\psi = \tan^{-1}(B_\phi/B_r)$ is obtained, Figure 4.8a. The blue histogram shows ψ of the meandering field and the green line corresponds to the Parker field. Note that in this model, the magnetic field in uni-polar and the current sheet is not added. Moreover, the solar wind speed is considered to be 400 km/s.

To compare the simulation with observations, the ACE magnetic field data on various dates during the solar cycle are obtained in GSE coordinates. The dates are selected according to Figure 4.7. Figure 4.8 illustrates the ψ angle obtained from one-second average data from ACE spacecraft at solar maximum from January 22 to February 17 of 2000, panel b, and solar minimum from January 1 to January 27, 2009.

In the GSE coordinates, in case of Parker field, $\psi = 133^\circ$ for positive polarity and 313° for negative polarity. Note that ψ depends on the solar wind speed; in GSE coordinates, as solar wind speed increases, ψ increases as well. Figure 4.8 b and c, clearly indicate two peaks around typical Parker field ψ for positive and negative polarity. By comparing the data from simulation and observation, the simulated histograms have a considerable similarity.

4.3.4 Trajectory of solar energetic protons

To investigate the trajectory of the solar energetic particles (SEPs), 300 source surface maps are generated. The SEPs are injected at the source surface, $10 R_{sun}$, when $t = 0$, map 150 is on the source surface and map 149 to map 1 are set for the time before $t = 0$. Note that the solar wind carries the footpoint data, and the particles at 1 AU see the solar wind that left the Sun 3.5 days ago. 150 maps are assigned to provide the information from the source surface to 43 AU. The maps 151 to 300 are applied in the forward direction in time as follows: After each day, the map on the source surface is updated and the layers of the maps are pushed outward. Map 151 replace map 150 and map 150 replace 149 and this goes on as the time passes.

100 MeV protons are injected on the source surface at various latitudes and longitudes with random initial pitch angles and followed for 4 days. Figure 4.9 shows 3D plots of two different proton trajectories that originated from latitude 45° with different longitudes, panel a and b, and in the ecliptic plane, panel c and d. The green dashed line is the Parker field line that emerged from the same starting point.

The majority of the solar energetic protons reaching 1 AU in approximately 20 minutes and go beyond; even in some cases reach 3 AU. However, after passing 1 AU for the first time, they begin to reverse multiple times. In many cases, they even go back to the Sun, Figure 4.9c and d. In some cases, protons reverse back and forth to the extent that they are not even able to reach 1 AU in 4 days.

Even though the field lines are Parker-like on large scales, there are lots of fluctuations and the direction of the local meandering magnetic field can be consider-

ably different. Moreover, at these energies, drifts are significant and the SEPs jump to another field line immediately and the neighboring field lines can have the opposite direction.

The variation of the pitch angle vs. travel time w.r.t. to local meandering and local Parker field is obtained to estimate the number of times that the particle reverse. Figure 4.10a and b show the variation of the pitch angle w.r.t. local Parker field, solid blue line, and meandering field, solid red line, from $t = 0$ to 25 minutes; panel c and d show the variation from $t = 0$ to 2 hours.

Protons in panels a and c are injected at latitude 45° and b and d in the ecliptic plane. It seems that solar energetic protons quickly focus and follow the meandering field line, reaching 1 AU in 20 minutes, on average. Note that, the pitch angle is w.r.t. to the local field and does not indicate that the particles stay on the same field line. In fact, we expect that energetic particles immediately jump to another field line due to curvature and Grad-B drifts. A better way to estimate the number of reversing times is to obtain the pitch angle w.r.t. to the local Parker field, the solid blue line in Figure 4.10. The pitch angle w.r.t. local Parker clearly proves that energetic protons are reversing countless times in just two hours. Again, we emphasize that this graph does not show that the SEPs follow the original field lines as mentioned in Kelly et al. (2012).

Finally, the variation of the kinetic energy of protons in 4 days is shown in Figure 4.11. The energy in the scatter-free Parker field is approximately constant, it drops $\leq 0.01\%$. In case of the meandering field, it drops 40% after 4 days.

4.3.5 Conclusion

In this chapter, we use a more realistic photospheric velocity spectrum and generate the meandering magnetic field line. The model is adapted from Hathaway 2016 private communication. The magnetic field lines are Parker-like, however, the fluctuations are quite strong locally. The drifts cause the protons to jump to another field line immediately and the new field line can be in a totally different direction which in turn leads to multiple reversing of the solar energetic particles. In our simulation, it seems that in this model, solar energetic particles are trapped between the Sun and 3 AU. In conclusion, the trajectory of the particles shows that these fluctuation velocities are too high that do not match the observations.

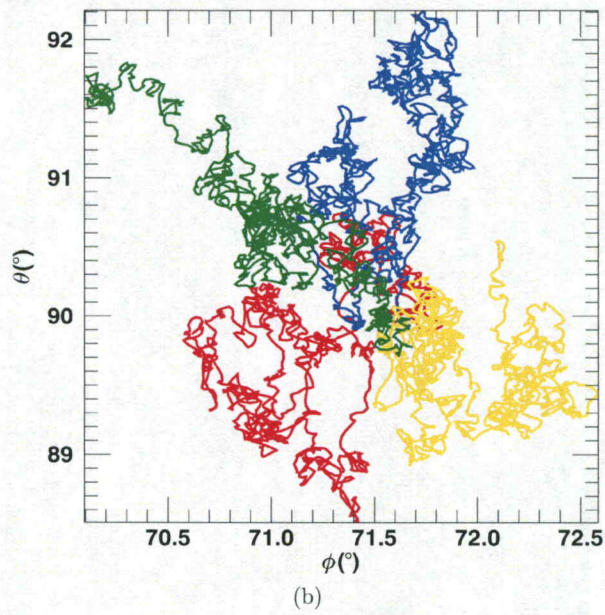
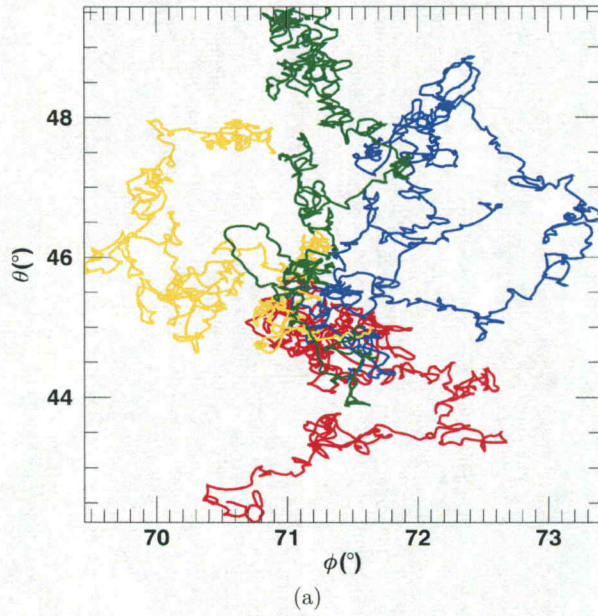


Figure 4.4: The random walk of the footpoints in Hathaway in (a) latitude 45° and (b) ecliptic plane. Different colors are corresponding to different longitudes that are rotated to start from $\phi = 0$.

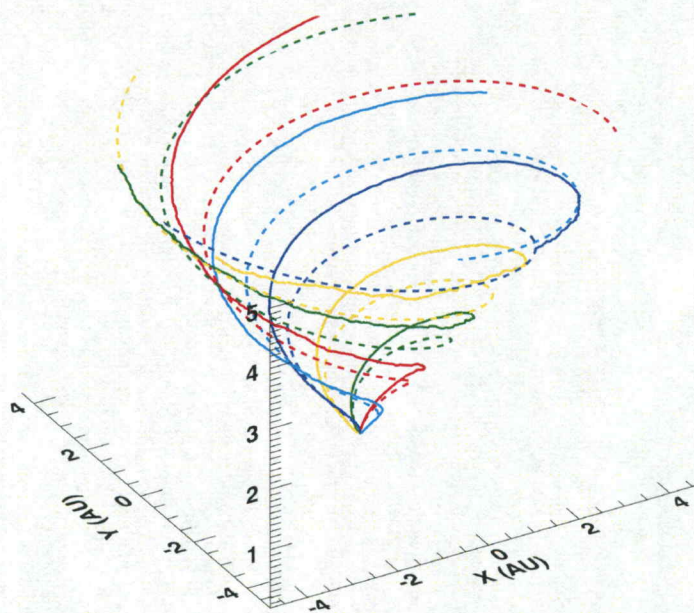


Figure 4.5: (a)

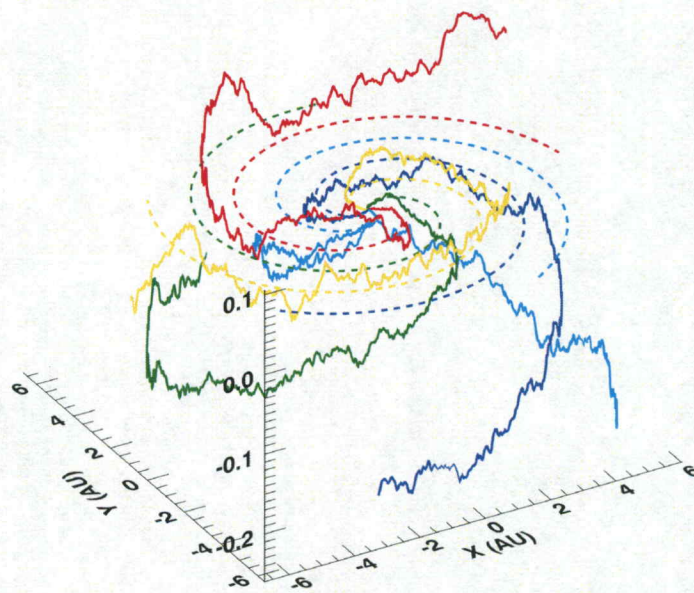


Figure 4.5: (b)

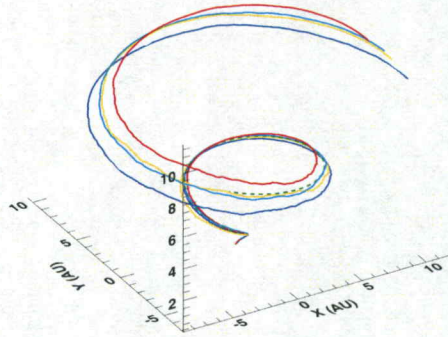


Figure 4.5: (c)

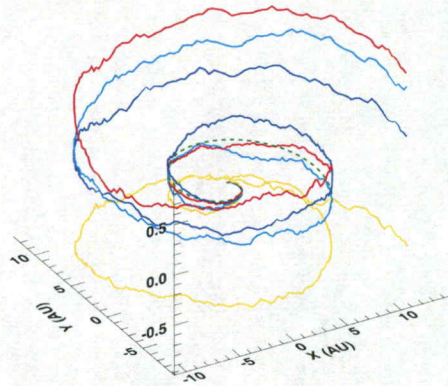


Figure 4.5: (d)

Figure 4.5: The meandering magnetic field lines obtained by adopting the Hathaway 2016 velocity spectrum. The field lines are followed from the source surface to 6 AU in panel (a) and (b) and 15 AU in panel (c) and (d). In panel (a) and (c), the field lines start from latitude 45° and in panel (b) and (d) from the ecliptic plane. Solid lines are the meandering field lines. In panel (a) and (b), the dashed lines are the Parker field lines originated from the same starting point of the same color meandering field line. In Panel (c) and (d), all magnetic field lines are rotated azimuthally to start from the $\phi = 0$ and the green dashed line is the Parker field line starts from $\phi = 0$.

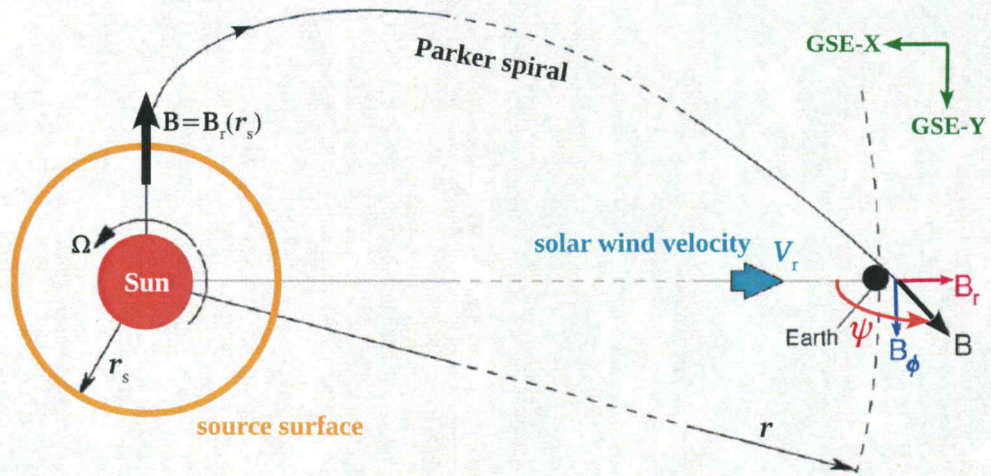


Figure 4.6: $\psi = \frac{B_\phi}{B_r}$ in GSE coordinates, Li et al. (2016).

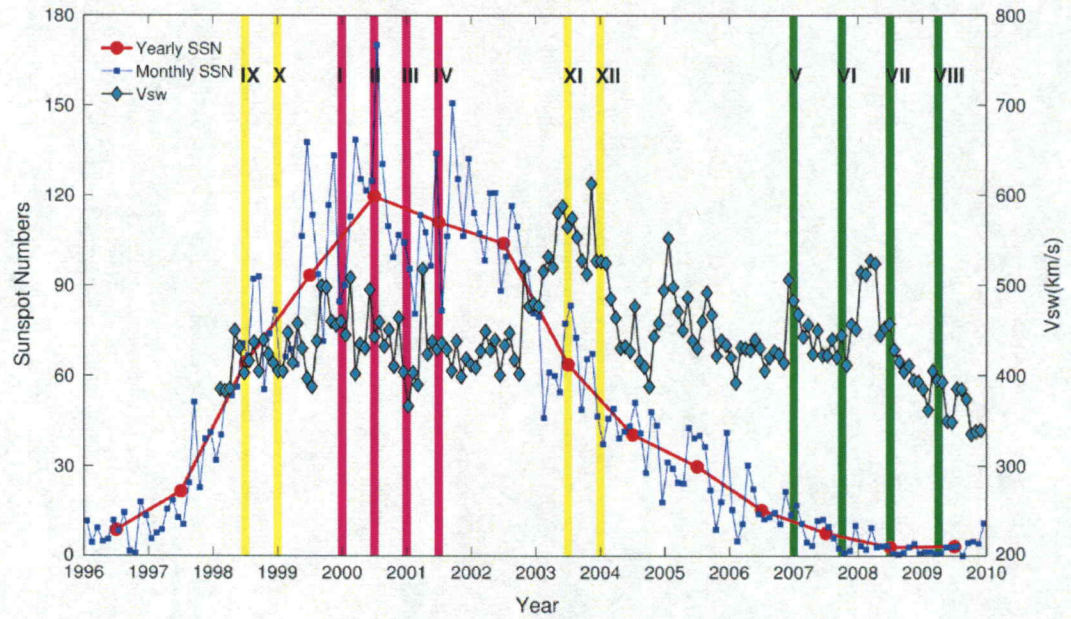
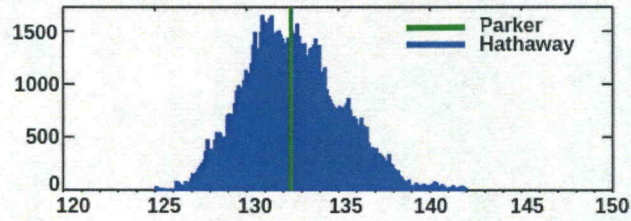
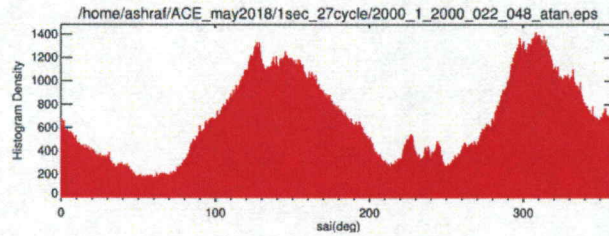


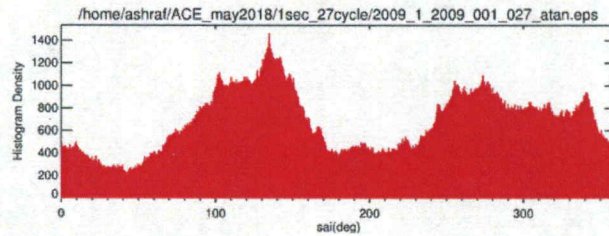
Figure 4.7: Sunspot activity from 1996 - 2010. 2000 is the solar maximum and 2009 is the solar minimum. Xu et al. (2015)



(a)



(b)



(c)

Figure 4.8: The histogram of the ψ , the angle between the B_r and B_ϕ in GSE coordinates at the ecliptic plane at 1 AU: (a) Simulated by Hathaway's Model. The blue is the ψ angle of the meandering field and the green corresponds to Parker. (b) The one-second average data solar maximum from ACE spacecraft for cycle January 22 to February 17 of 2000 (c) The one-second average data solar minimum from ACE spacecraft for cycle January 1 to January 27, 2009. Solar wind velocity in (a) is chosen to be 500 km/s.

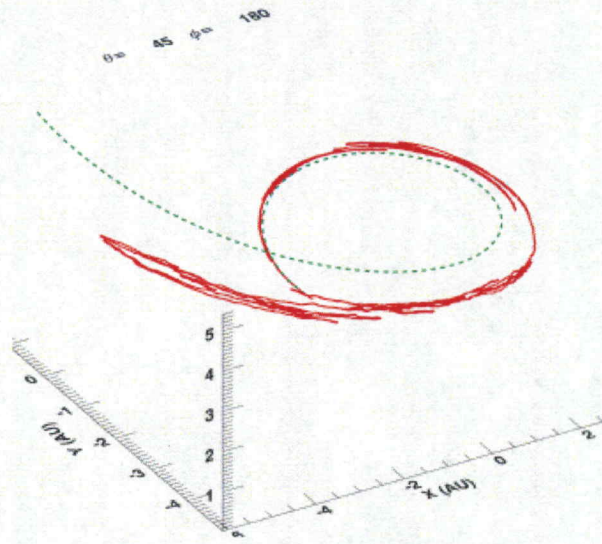


Figure 4.9: (a)

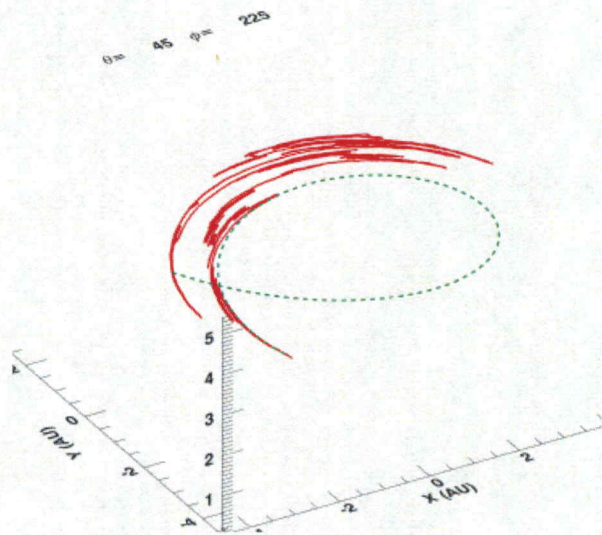


Figure 4.9: (b)

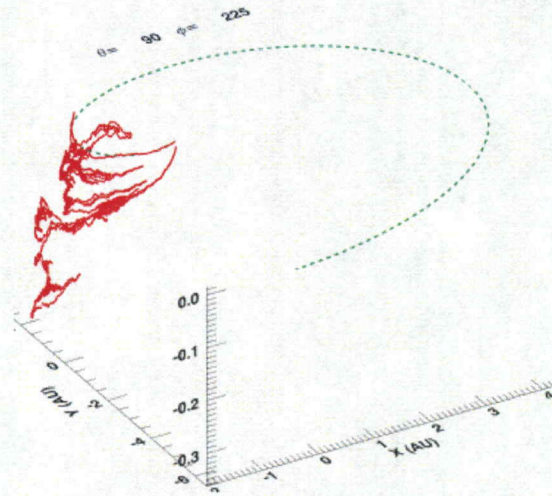


Figure 4.9: (c)

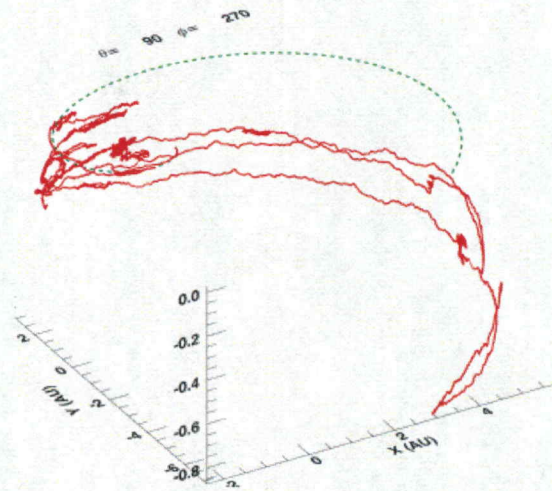


Figure 4.9: (d)

Figure 4.9: Two examples of the 100 MeV protons 3D trajectories in the meandering magnetic field in latitude 45, panel (a) and (b), and ecliptic plane, panel (c) and (d). The protons are followed for 4 days. The red solid line is the trajectory of the solar energetic protons and the green dashed line is the original Parker field line.

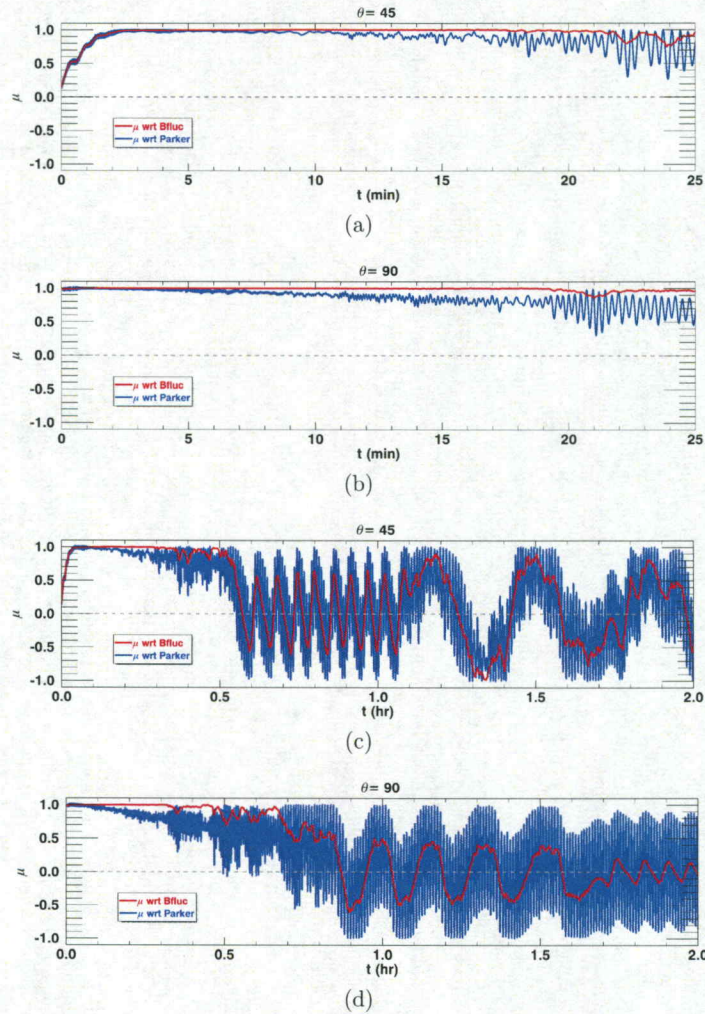


Figure 4.10: The variation of the cosine of pitch angle, μ , in 25 minutes, panel (a) and (b), and 2 hours, panel (c) and (d). The proton in (a) and (c) is injected in latitude 45 and the proton in (b) and (d) is injected in the ecliptic plane. The red line is the cosine of pitch angle w.r.t. to the local meandering field and the blue line is w.r.t. the local Parker field.

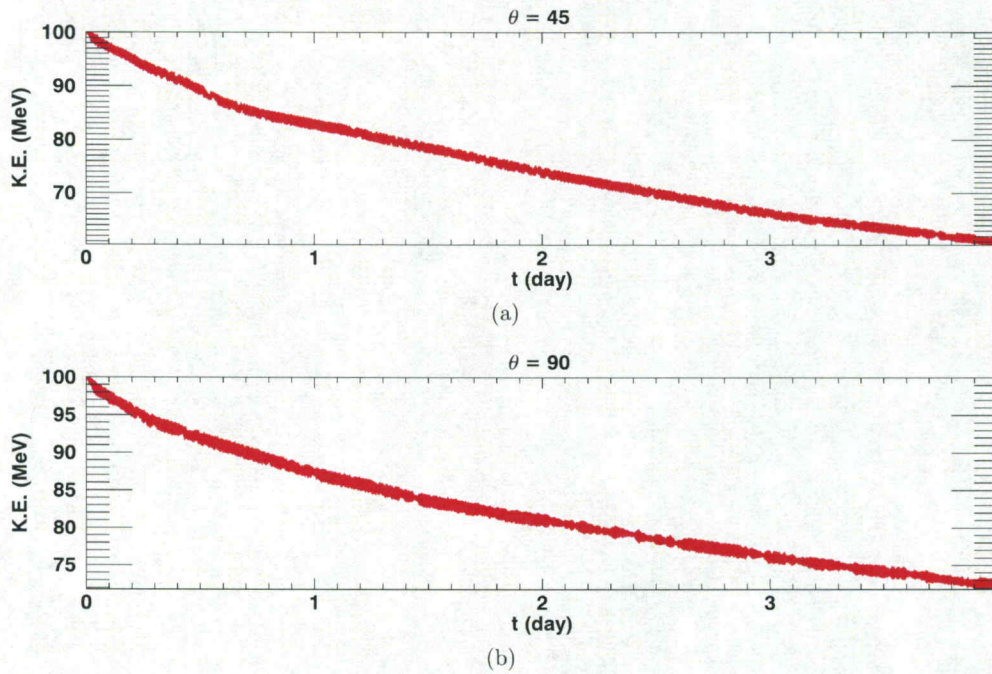


Figure 4.11: The variation of the kinetic energy of two individual protons in a meandering field for 4 days. The top panel is injected at latitude 45 and bottom panel in the ecliptic plane. The initial energy 100 MeV.

CHAPTER 5

MEANDERING MAGNETIC FIELD DEVELOPED FROM THE EXPANSION OF OPEN MAGNETIC FLUX TUBES EMERGING FROM THE BORDERS OF THE SUPERGRANULES

As mentioned in Section 1.2, the open magnetic flux tubes emerge from the photosphere. The horizontal advecting flows move from the center to the border which leads to the concentration of the open magnetic flux tube's footpoints near the borders of the supergranules. As these magnetic flux tubes expand in the lower inner corona; they cover the entire source surface. In this chapter, we discuss two new models that we developed to approach the footpoint motion. We adopt Hathaway 2016 photospheric velocity model, Chapter 4. In these two models, we determine the borders of the supergranules and extrapolate it to the source surface. In Section 5.1, we filter out the center of the supergranules and extrapolate the remainder of the map into the source surface. In Section 5.2, we obtain the distribution of the velocity spectrum on the estimated borders; regenerate the same velocity distribution on the source surface. In both models, the magnetic field and the motions of the footpoints are investigated, however, only in the first model, Section 5.1, the trajectory of the solar energetic particles are examined.

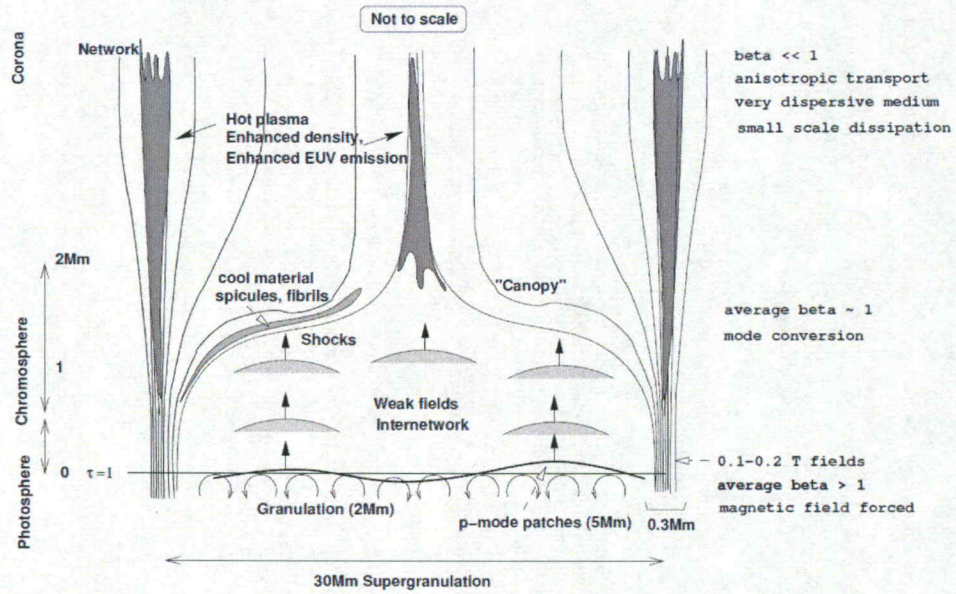


Figure 5.1: The open magnetic field lines coming from the boundaries of supergranules only, Judge (2006)

5.1 Extrapolating the borders of the supergranules to the surface

5.1.1 Model

The first task is to determine the borders of the supergranules on the photosphere. At first, we assumed that 5% of the photosphere's surface is covered by the borders of the supergranules. By further investigation, we find that the width of the borders of the supergranules is about 0.3 Mm which means that the borders cover roughly 1% of the surface of the photosphere, Judge (2006). We extract 5% and 1% area that has the lowest horizontal speed, $V_g = \sqrt{V_\theta^2 + V_\phi^2}$. From the velocity distribution of Hathaway, 5% and 1% of the area of the photosphere corresponds to

$V_g \leq 90.0$ and ≤ 40.0 m/s, respectively. We denote the maximum of V_g within inside the boundaries, V_{limit} . In addition, we estimate the lowest resolution necessary for the map to ensure that the borders are not missed in the investigation. By comparing the width of the border, 0.3 Mm, to the Sun's perimeter, the resolution has to be at least 0.03° . The maps in this section has the resolution of 0.01° .

Next, we exclude grid points that have higher horizontal velocity than V_{limit} from the map and obtain the map of the borders of the supergranules. By changing the scale of the surface flow velocity map, the location of the borders of the supergranules is estimated. The color bar scale in Figure 5.2 is changed to identify the boundaries locations on the map. The dark blue areas can be regarded as borders of the supergranules.

Figure 5.3 compares the observed magnetic field concentrations on the borders of supergranules, Rincon and Rieutord (2018), to the extracted borders from the simulated maps. Panel a shows the concentration of magnetic flux tubes on the border of the supergranules. In panel b, $5^\circ \times 5^\circ$ simulated photospheric flow velocity map with resolution of 0.001° are presented. The color bars in panel b and c are changed to be able to visualize the boundaries of the supergranules. Panel c, zoomed in to estimate boundary location and panel d, shows the vector velocity map of the same border. Note that the width of the image in panel a is $0.03^\circ \sim 0.3$ Mm which is the width of the supergranules boundary, and the width in panel b is 5° . Even though panel b has a larger scale, only the concentrations of the magnetic field flux tubes are the important factor. In this regard, (a) and (b) are similar. As it can be seen in Figure 5.3d, the horizontal velocity vectors are directed to the boundaries of

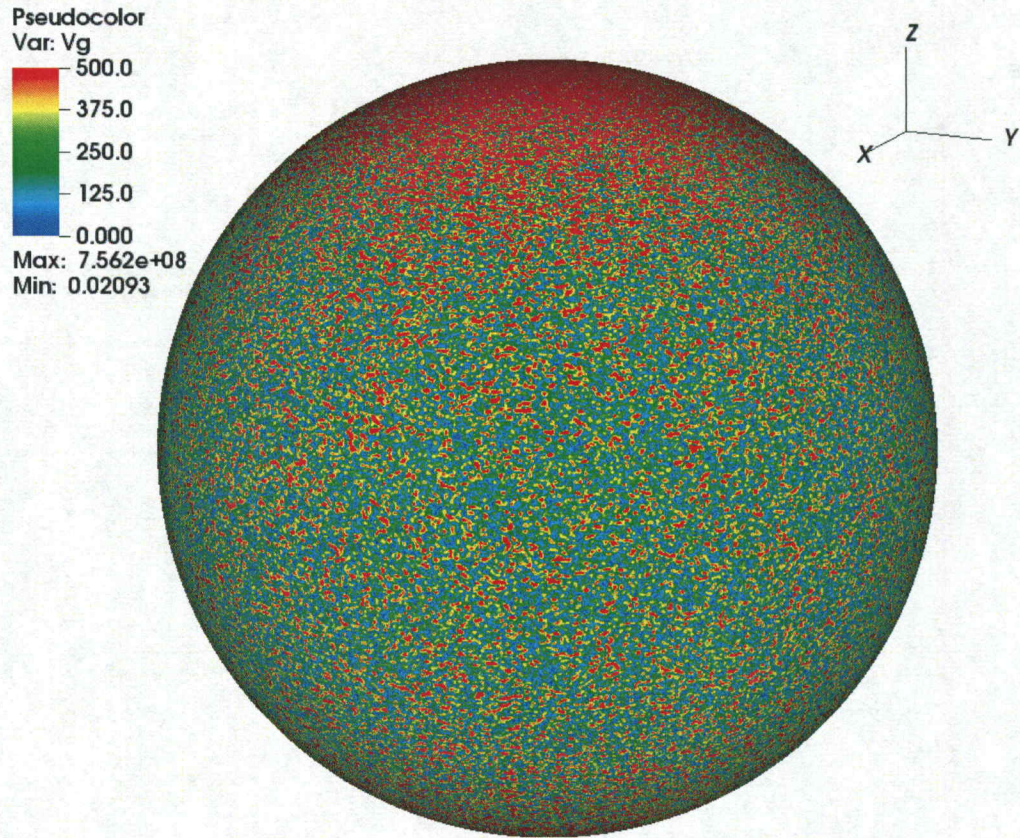


Figure 5.2: The horizontal flow velocity map, $V_g = \text{sqr}t(V_\theta^2 + V_\phi^2)$, on the photosphere. The color bar is changed to show estimated boundaries of the supergranules. The dark blue areas can be considered as the borders of supergranules or magnetic concentrations on the surface of the photosphere.

the supergranules. Although this vector velocity field looks like a completely well-behaved velocity map, unfortunately, this is not the case on all boundaries; in some

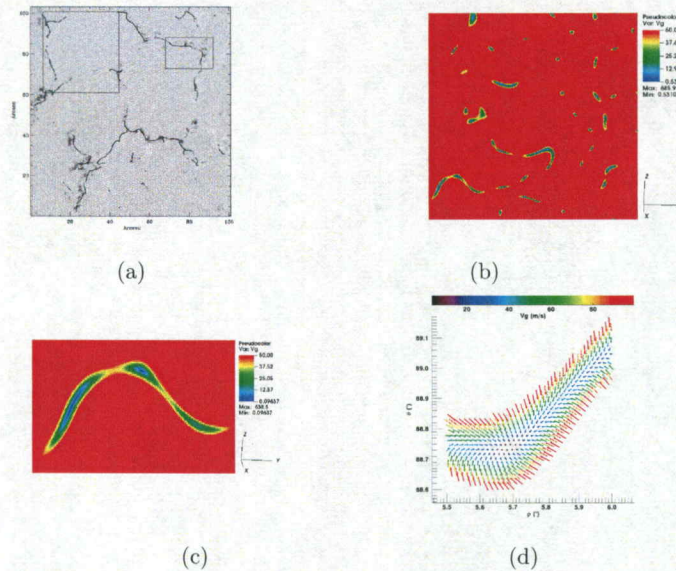


Figure 5.3: Comparison of the (b) simulated supergranule boundaries to (a) observed magnetic flux tube concentration on the supergranules border. The color bars on the left side of (b) and (c) show the magnitude of V_g . The dark blue areas present supergranules boundaries. (c) zoomed in on the of the border on the left bottom of (b). (d) shows the flow velocity direction on the border. The colors of the vectors present the magnitude of V_g . The resolution of the simulated maps is 0.001° .

boundaries, the flow velocities have the opposite direction, flowing outward from the boundaries of the supergranules.

Each point on the source surface is interpolated from multiple points on the photosphere and we need enough points to be able to do the extrapolation. The boundaries of the supergranules are randomly distributed and each boundary may be on top of one or multiple grid points, depending on the area of the border. In order to decide the number of the neighboring grid points that should be included in the interpolation procedure, we select 30 locations on the map that are evenly separated

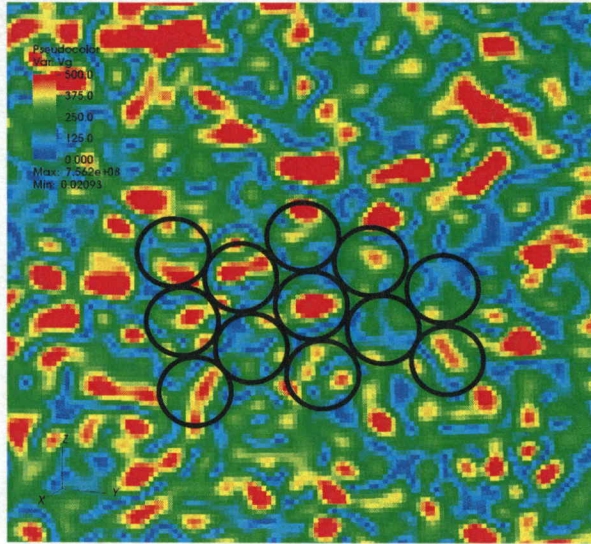


Figure 5.4: A zoomed-in image of Figure 5.3. The dark blue areas can be regarded as the supergranules boundaries. The black circles are the typical size of the supergranules. The figure is not to scale.

in both latitude and longitude. On each chosen location, the number of the grid points on top of the borders' map that are inside a circle of 1, 2 and 3 times of the supergranule's radius ($R_{SG} \sim 1.25^\circ$) are determined. Figure 5.4 shows the maximum and minimum of the . Next, the minimum and the maximum number of these grid points are recorded. The same procedure is repeated for all 300 maps. Figure 5.5 shows the minimum and the maximum of the number of grid points 1 supergranule's radius. located on the borders in the area inside a circle within 1.25° . The number of the minimum and maximum points is averaged over 300 maps. Figure 5.5 shows that we need to count at least 65 closest neighboring points, and it is safer to take at least 265. The same is done for the area enclosed inside 2 and 3 times of the supergranule's border.

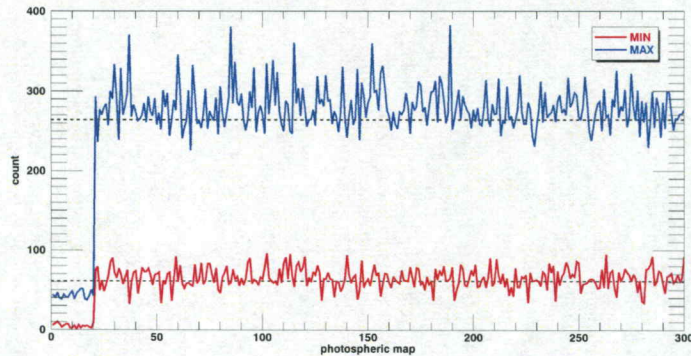


Figure 5.5: The average minimum number and maximum number of the grid points that are located on top of the supergranules boundaries, enclosed in R_{SG} , (1.25° , a typical size of supergranule). Minimum (red) and maximum (blue) number of the grid points enclosed in one supergranule's border out of 30 location on each map. The average of maximum number of the grid points on 300 maps are 265 and average minimum is 65 points.

The extrapolation method that is used in this section is as follows: We expand the borders' map, linearly from the photosphere to the source surface, $10 R_{sun}$. On the source surface, we apply a method called spherical scatter interpolation. This method is applicable for randomly scattered data points; interpolates the quantities between these scattered points using the nearest neighboring points, called Kriging or Gaussian process regression, Williams (1997).

At first, a few maps are interpolated using 65 and 265 neighboring points. The results are practically the same. Therefore, we choose 65 neighboring points that decrease the interpolation time by a factor of 200. The extrapolated map is shown in Figure 5.6. As can be seen, the velocity map on the source surface is almost uniform and there is no large horizontal flow velocity. Again, 300 maps are generated to cover the interplanetary space from the Sun to 43 AU and from $t = 0$ to $t = 150$ days.

The source surface map is changed every 24 hours, the lifetime of the supergranules, exactly as explained in Chapter 4.

5.1.2 Results and Discussion

5.1.2.1 Flow pattern on the source surface

The extrapolated flow velocity map on the source surface is presented in Figure 5.6. As mentioned in the previous section, the source surface is assumed to be at 10 solar radii and covers all latitudes below $\pm 85^\circ$. The flow velocity map on the source surface consists of two components: V_θ , V_ϕ and the magnitude of the random motion is given by $V_g = \sqrt{(V_\theta^2 + V_\phi^2)}$. Figure 5.6 shows the V_g . The color bar ranges from 0 to 41 m/s. As can be seen from the figure, the flow speed does not have very high values near the poles since in the photospheric map the higher flow velocities have already been filtered out.

5.1.2.2 Footpoint motion on the source surface

Next, we investigate the footpoint motion on the source surface to check how the footpoints move and to examine if each footpoint shows the random walk we were expecting. In this model, again, the first interpolated map is generated at $t = 0$ and we follow the footpoints backward in time from $t = 0$ to -30 days, exactly the same as in Chapter 4. After each day, the lifetime of supergranules, the map is updated to a new map. $V_{limit} = 40$ m/s corresponds to the case that boundaries of the supergranules are covering 1% of the photosphere. Figure 5.7 shows the motion of the footpoints at latitude 45° and in the ecliptic plane. Furthermore, the footpoint

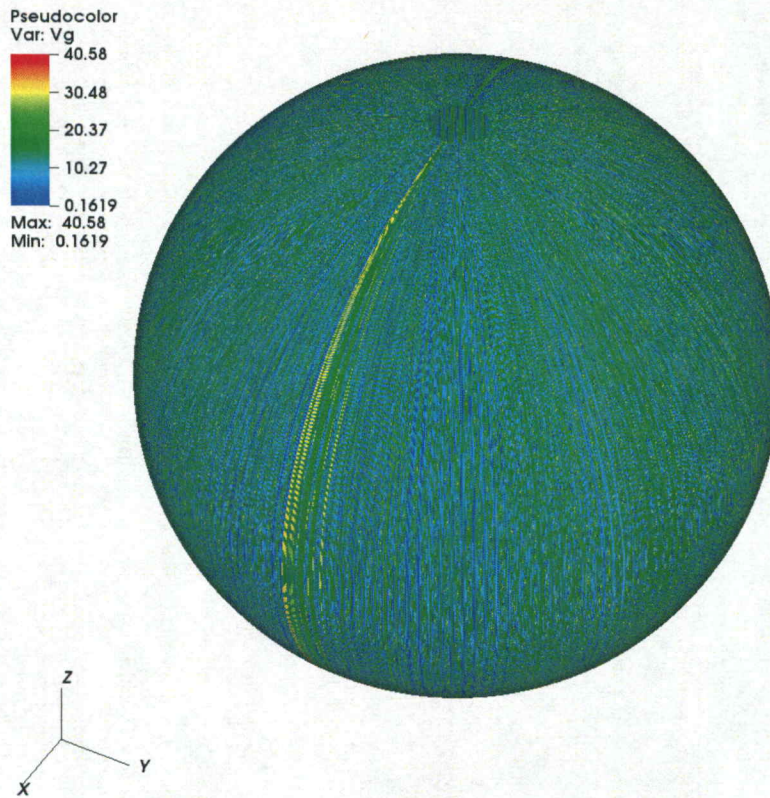


Figure 5.6: The horizontal flow velocity map on the source surface in extrapolated model. $V_g = \sqrt{V_\theta^2 + V_\phi^2}$. Color bar for panel is from 0 to 41 m/s.

trajectories are rotated to start from the same longitude. Moreover, the motion due to solar rotation is omitted to show only the motion of the footpoints. Each color corresponds to a different longitude. The motion of the footpoints is even slower than Hathawy's model, Chapter 4, and the displacements are only in $\pm 1^\circ$ range in both latitudinal and longitudinal directions after 30 days. This displacement is plausible

since $V_{limit} = 40$ m/s. It is evident that, unlike other models, footpoints tend to move in one direction. This is justifiable since the velocity on the source surface is slowly varying (Figure 5.6).

5.1.3 Interplanetary Magnetic Field

In this section, we apply the 300 extrapolated flow velocity maps. The resolution of the source surface maps is reduced to 0.5° in both latitudinal and longitudinal directions. A higher resolution map required a huge memory that slows down the simulation code; the existing clusters do not have enough memory to process high-resolution maps in our test particle simulations. Note that the statement is made only about the test particle simulations. Even though the magnetic field generator is a hundred times faster, the reduced resolution maps are applied to generate the magnetic field to be consistent with test particle simulation. Because, the magnitude of flow velocity on the source surface is roughly uniform, reducing the velocity map resolution does not lose considerable information. The source surface maps are also changed every day, the same way implemented in Chapter 4. The solar wind speed is 500 km/s, $B_0 = 1.78 \times 10^{-4}$ T and $\Omega = 2.86 \times 10^{-6}$ rad/s, the same as Chapter 4.

The magnetic field lines are followed from the source surface to 8.5 AU, shown in Figure 5.8. The top row is (a) 3D (b) XY (c) XZ projection of four field lines originated from latitude 5° and four equally separated longitudes. The bottom row is the same as the top row for the ecliptic plane. The solid field lines are the meandering field and the dashed field lines are the corresponding Parker field that is originated from the same color starting point.

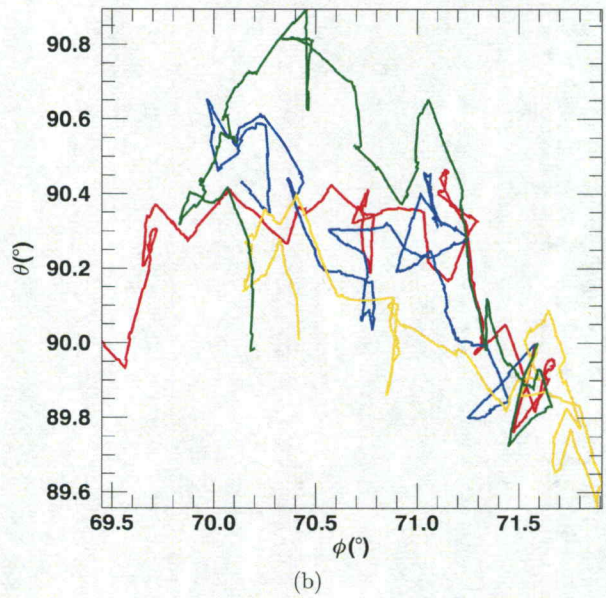
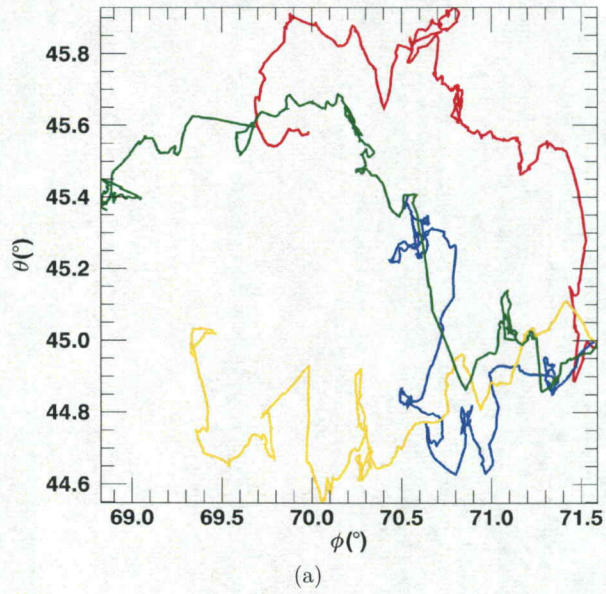


Figure 5.7: Motion of the footpoints in the interpolated map in (a): latitude 45° and (b): the ecliptic plane. Each color corresponds to different longitude that is rotated to start from the same ϕ .

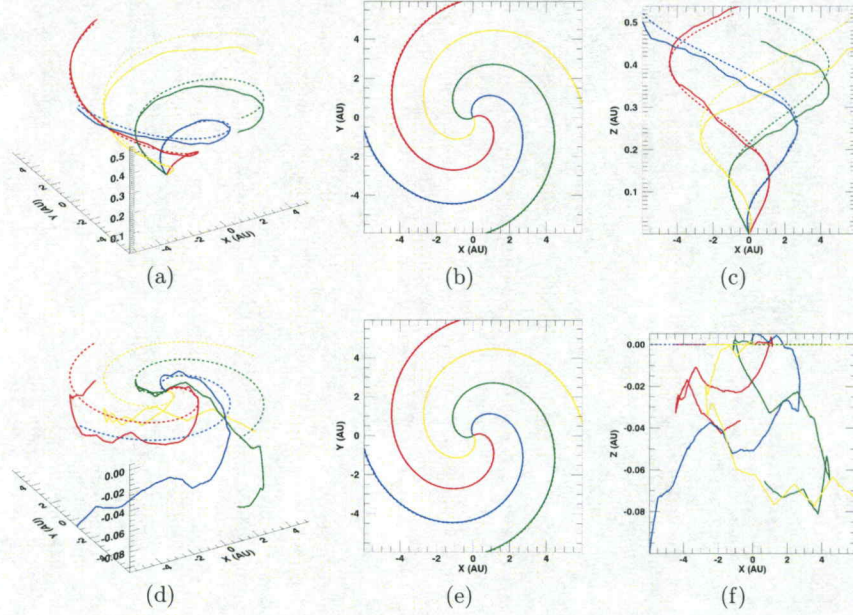


Figure 5.8: (c) The magnetic field in the interpolated map. The meandering magnetic field lines in the interpolated model. $V_{limit} = 40.0 m/s$ which is the equivalent that the borders are covering 1%. Solid lines are the meandering field lines and dashed lines are the Parker field lines. Panel (a) and (d) are 3D field lines, panel (b) and (e) projection in the XY projection and panel (c) and (f) are the projections in XZ plane. The field lines are traced to $R = 8.5$ AU. In all figures, the same color field lines (Parker or the meandering field lines) start from the same locations.

It is evident that the meandering field lines are very Parker-like and close to original Parker, as it is anticipated since the flow velocities on the source surface are small, $V_{limit} = 40$ m/s. Note that the meandering field lines in higher latitudes such as co-latitude 45° , appear to be the same as the Parker field lines. However, fluctuations can be visible in a closer view of the graph, Figure 5.8 a, b and c.

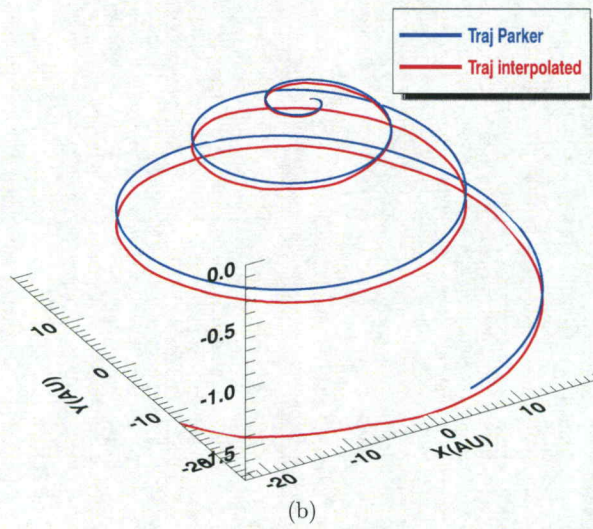
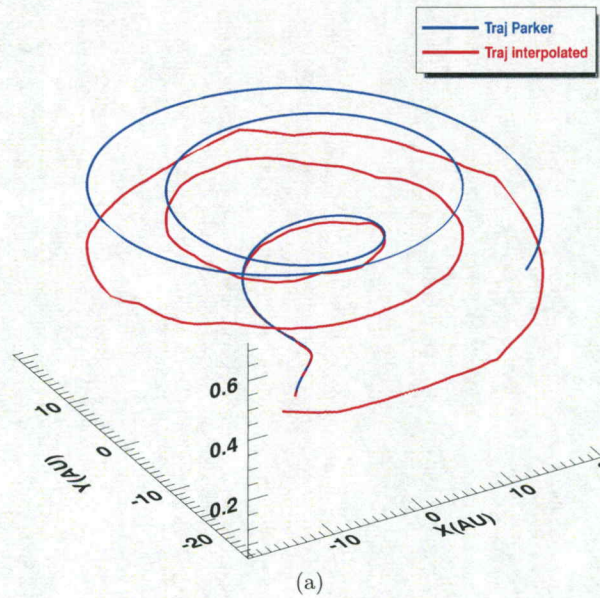


Figure 5.9: Comparison of the trajectory of solar energetic protons in Parker magnetic field, blue solid line, and the meandering magnetic field, red solid line. (a) Latitude 5° . (b) The ecliptic Plane.

5.1.3.1 Trajectory of the solar energetic protons

Next, we inject solar energetic protons in the meandering magnetic field. Since the footpoint flow velocity on the source surface is ≤ 40 m/s, we compare them with the trajectory of the same protons in the Parker field. 100 MeV protons with random initial pitch angles are injected at several latitudes and longitudes. In this section, we present trajectories of two protons at latitude 5° and in the ecliptic plane, Figure 5.9. The red solid lines are the trajectories of the energetic protons in the meandering field and solid blue lines are the trajectories of the energetic protons in the Parker field. As can be seen, the trajectories are similar but can be clearly separated. In both panels a and b, the protons are displaced in the negative Z-direction due to the drift. As it was mentioned by Dalla et al. (2013), the drifts are significant for high energetic protons.

5.1.3.2 Conclusion

Open magnetic flux tubes expand into interplanetary space. They concentrate near the boundaries of the supergranules. In this model, the boundaries of supergranules are extracted from the photospheric flow velocity maps. The maximum flow velocities on the boundaries of the supergranules are obtained, $V_{limit} = 40.0$ m/s. The maps and the open magnetic flux tubes are expanded to the source surface at 10 solar radii, using the Kriging method. Again, the footpoint motion on the source surface is plotted. The interplanetary magnetic field lines are Parker-like and closer to Parker than magnetic field lines generated by Hathaway's flow velocity spectrum,

with smaller fluctuations. The trajectories of several 100 MeV protons in the meandering magnetic field are compared to the trajectory of the same protons in the Parker field. Overall, the trajectories in the Parker field and the meandering field look similar. However, they can be clearly separated.

5.2 Adding memory to the footpoints motion

As mentioned in Section 5.1, the extrapolation method is a time consuming simulation model. In an attempt to reduce the simulation time, we discuss an alternative method.

5.2.1 Model Description

Instead of finding and generating the flow velocity map, we can use the flow velocity distribution on the supergranule boundaries, assuming the flow velocity distribution at the source surface to be the same, to obtain flow velocity map on the source surface. Figure 5.10a, b and c show the velocity distribution of V_g , V_ϕ and V_θ using the Hathaway's flow velocity map, Chapter 4, respectively. In Section 5.1, V_{limit} is determined to be 40 m/s. The same distribution was generated on the source surface, however, the footpoints displaced slightly and the magnetic field did not meander and the trajectories of the energetic particles were not affected as well. Instead, memory is given to the footpoints velocity as follows: An initial velocity is drawn from a distribution the same as V_g distribution on the boundaries of the supergranules, in a random direction. Next, in each time step, the magnitude of the footpoints' velocities are chosen from the same distributions but the direction is changed. The new

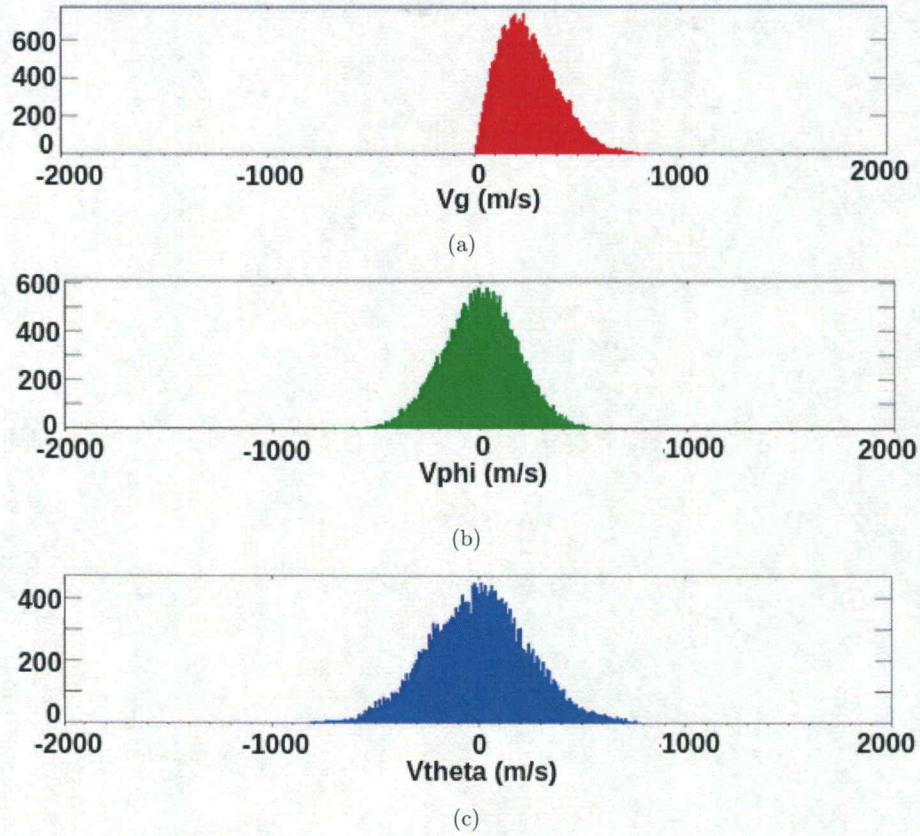


Figure 5.10: The distribution of the horizontal flow velocity in Hathaway 2016 map.

direction is deviated from the previous velocity vector by an angle α_n . The angle α_n is chosen from a normal distribution with a zero mean value, $\mu = 0$. The standard deviation is a free parameter that determines the extent of the footpoints' motion on the source surface, Figure 5.11.

α_0 is the initial direction of the footpoint velocity, randomly chosen, V_0 is the magnitude of the initial footpoint velocity. Next step, we choose an angle α_1 w.r.t.

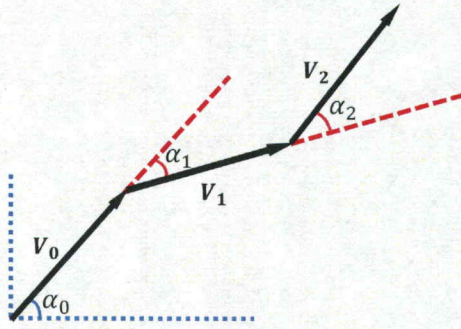


Figure 5.11: The model to select the footpoint's next velocity. α_0 is the initial direction of the footpoint velocity, randomly chosen, V_0 is the magnitude of the initial footpoint velocity. Next step, we choose an angle α_1 w.r.t. \mathbf{V}_0 from a normal distribution and decides \mathbf{V}_1 and the same goes for \mathbf{V}_2 .

\mathbf{V}_0 from a normal distribution and determine \mathbf{V}_1 and the same procedure continues.

V_θ and V_ϕ can be found as:

$$V_\theta^n = V_n \sin\left(\sum_{n=0}^n \alpha_n\right) \quad (5.1a)$$

$$V_\phi^n = V_n \cos\left(\sum_{n=0}^n \alpha_n\right) \quad (5.1b)$$

where V_n is drawn from the V_g distribution on the boundaries of the super-granules, α_n is the deviation from V_{n-1} , obtained from the normal distribution with the standard deviation, σ . Note that $V_n \leq V_{limit}$.

5.2.2 Results and Discussion

5.2.2.1 Footpoints motion on the source surface

We investigate how the footpoints move in this model. In particular, we examine if the footpoints actually random walk. In this model, again, we start from $t = 0$ and go backward in time, however, the sequence of velocities does not change after 24 hours. Due to the nature of this model, it is not necessary to change the flow maps in 24 hours. The footpoint are followed for 43 days and the results are shown in Figure 5.12. In addition to $V_{limit} = 40$ m/s, the case of $V_{limit} = 100$ m/s is also investigated to examine the impact of V_{limit} on the footpoint motion. Five distributions with standard deviation 0.010, 0.025, 0.050, 0.075 and 0.100 radian are used. Each color corresponds to a distribution with one standard deviation as listed above. Panel a and b shows the motion of the four footpoints initiated from the same latitude and longitude. In panel a, V_{limit} is chosen to be 40 m/s, 100 m/s in panel b. Panel c and d are the same for the ecliptic plane. Each color corresponds to one standard deviation. As can be seen, the footpoints random walk on the source surface. As the standard deviation decreases, the footpoints travel a longer distance from the initial location. The free parameter, σ , can be changed to obtain an optimized value that can explain the observation at 1 AU and beyond. Note that as the V_{limit} increases, the footpoints random walk the same way, however, the displacement extends from $\pm 2^\circ$ to $\pm 4^\circ$.

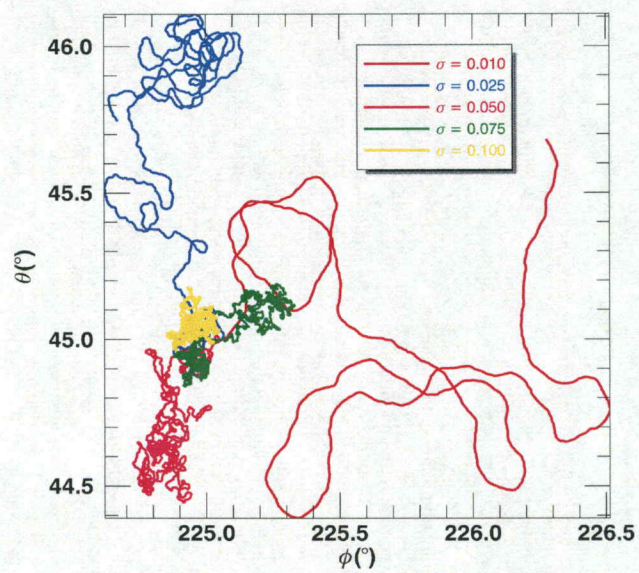


Figure 5.12: (a)

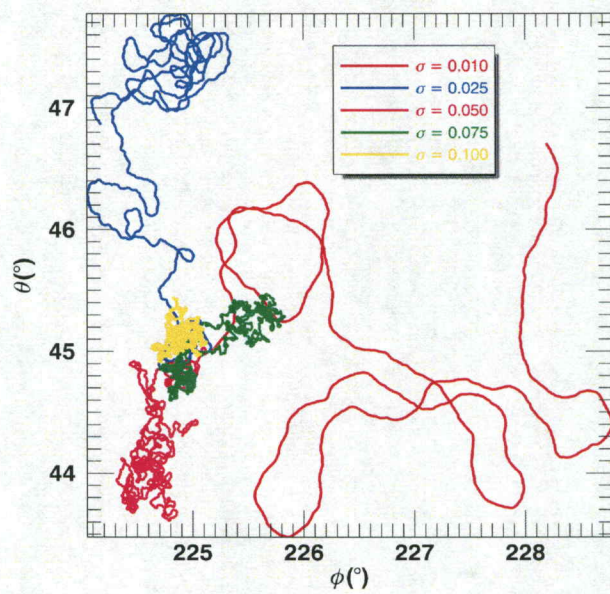


Figure 5.12: (b)

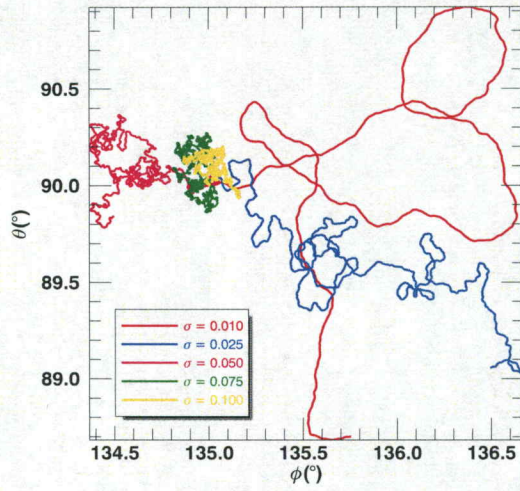


Figure 5.12: (c)

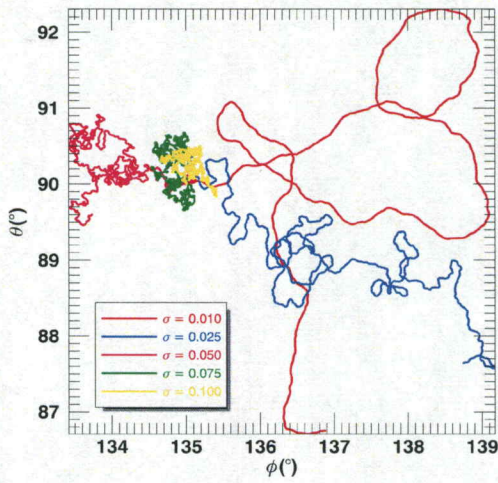


Figure 5.12: (d)

Figure 5.12: Footpoints motion on the source surface in latitude 45° , (a) and (b), and ecliptic plane, (c) and (d). Colors correspond to various σ that originates from the same footpoint (a) and (c): $V_{limit} = 40 \text{ m/s}$. (b) and (d): $V_{limit} = 100 \text{ m/s}$.

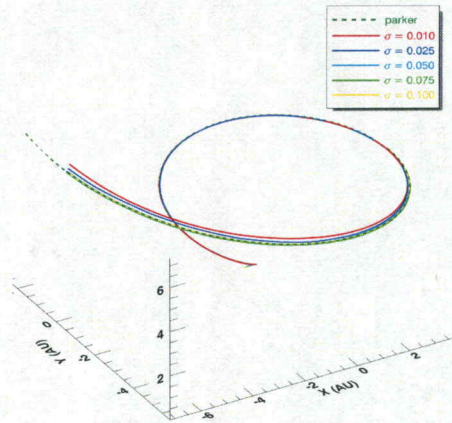


Figure 5.13: (a)

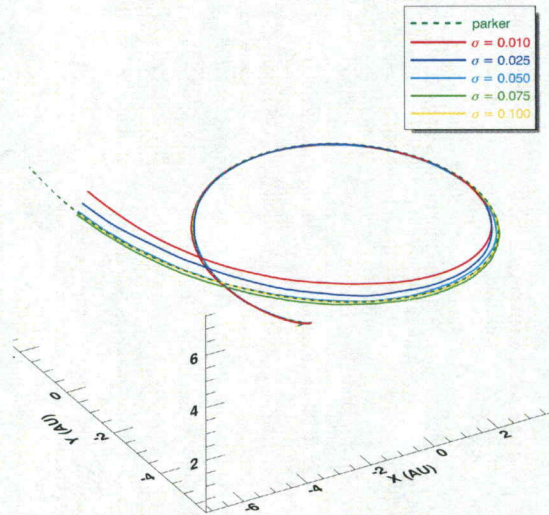


Figure 5.13: (b)

5.2.2.2 Interplanetary Magnetic Field

Next, we examine how magnetic field lines behave on the basis of this model.

Again, the solar wind speed is considered 500.0 km/s , $B_0 = 1.78 \times 10^{-4} \text{ T}$ and

$\Omega = 2.86 \times 10^{-6} \text{ rad/s}$.

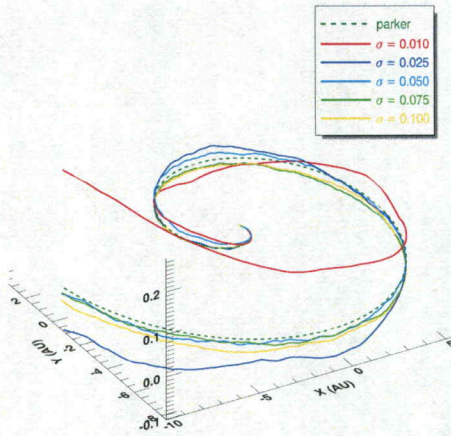


Figure 5.13: (c)

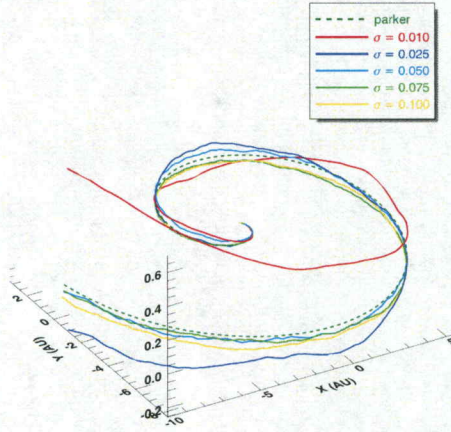


Figure 5.13: (d)

Figure 5.13: Magnetic field lines originates from latitude 45° , (a) and (b), and ecliptic plane, (c) and (d). Colors correspond to various σ that originates from the same footprint (a) and (c): $V_{limit} = 40 \text{ m/s}$. (b) and (d): $V_{limit} = 100 \text{ m/s}$. Dashed green line is the Parker field line emerges from the same footprint.

The magnetic field lines are followed from the source surface to 10 AU. A 3D graph of the magnetic field lines at the same longitude and latitude with five different distributions with the standard deviation 0.010, 0.025, 0.050, 0.075 and 0.100 radian are shown in Figure 5.13 at latitude 45° , a and b, and in the ecliptic plane in panel c and d. Note that σ is the standard deviation of the distribution that the angle α is drawn. Panel a and c and d are corresponding to $V_{limit} = 40$ m/s and panel b, d and e are corresponding to $V_{limit} = 100$ m/s. The dashed green line is the Parker field line that originates from the same starting point.

Again, the meandering field lines are Parker-like, as anticipated since the flow velocities on the source surface are small, $V_{limit} = 40$ m/s and 100 m/s. Note that the meandering field lines at higher latitudes such as co-latitude 45° , are very close to Parker field lines, fluctuations are only visible if we blow up the graph.

5.2.3 Conclusion

In this section, a new method is introduced to simulate the random walk of the footpoints on the source surface. First, the distribution of the footpoints within supergranule boundaries is obtained. In every step, the magnitude of all footpoint velocities on the source surface is chosen from the same distribution. In addition, the direction of the footpoint velocities are decided by the following procedure: In the first step, we choose a random direction, then in each step, the velocity vector deviates from the previous time by a small angle that is drawn from a normal distribution. The standard deviation of the distribution is a free parameter that decides how the footpoints move on the source surface. Five distributions with $\sigma = 0.010, 0.025,$

0.050, 0.075 and 0.100 radian are implemented and the motion of the footpoints and meandering interplanetary magnetic field lines are investigated. In future study, we will investigate the trajectory of the solar energetic particles in the proposed model. In conclusion, we developed an alternative method to simulate the random walk of the footpoints. A comparison of the path length distributions at 1 AU to the observation can lead to a better understanding of the source surface of the interplanetary magnetic field.

5.3 Comparison of all three models of footpoint motion

Finally, we compare all three models introduced in Chapter 4, Section 5.1 and Section 5.2. The footpoint random walk on the source surface and the magnetic field lines in three models, extrapolation, Hathaway and memory model with $\sigma = 0.010$, 0.025 and 0.050 radian are compared in Figure 5.14 and Figure 5.15.

Figure 5.14 illustrates the motion of a footpoint in the extrapolated map, blue, the Hathaway map, red, and memory method, magenta with $\sigma = 0.010$, light green $\sigma = 0.025$ and sky blue, $\sigma = 0.050$ radian. As can be seen, the footpoint on the Hathaway map fluctuates more than the other two methods. It also clearly shows that by varying the σ and V_{limit} , we can obtain a large range of footpoint motion.

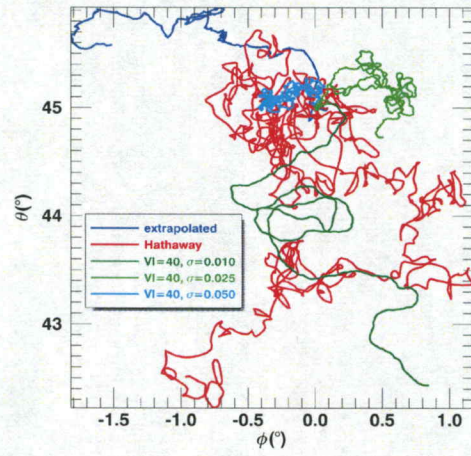


Figure 5.14: Comparison of the motion of the footpoints in all three new method introduced in this study.

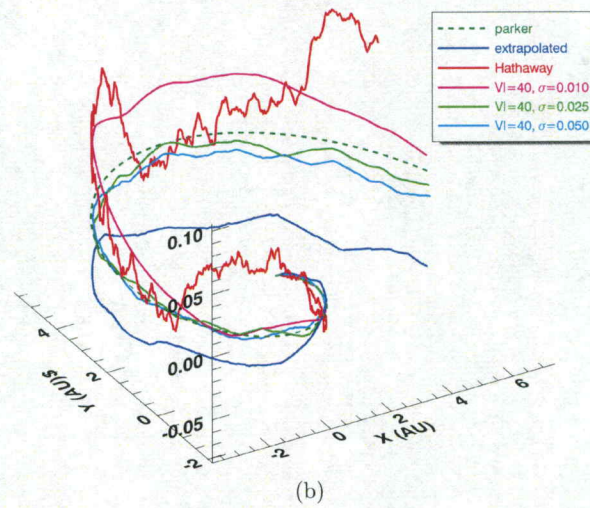
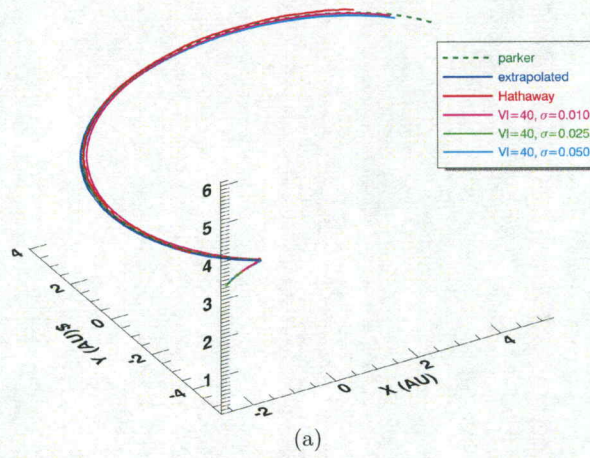


Figure 5.15: Comparing the magnetic field lines in all three models in (a)latitude 45° and (b) ecliptic plane.

CHAPTER 6

CONCLUSION

Solar energetic particle (SEP) events are classified as gradual or impulsive. Gradual SEP events are associated with CMEs and particles are accelerated at the CME-driven shocks. In these events, particles are accelerated in a spatially extended region and over a longer period of time. In comparison, impulsive events are associated with solar flares and are often spatially confined and the acceleration occurs within a short period of time.

Understanding solar wind magnetic field topology is essential to understand the observations of solar energetic particle events. The often referred to Parker field was first proposed by Parker (1958) when he constructed an isothermal hydrodynamic solar wind model. In a reference frame co-rotating with the Sun, the solar wind emanating from the inner boundary (at several R_s) has a constant outward radial velocity and a purely radial magnetic field. The Parker field topology has been tested by many observations and for long-term averages of the magnetic field. It provides a reasonable picture even though the solar wind speed can vary dramatically from one period to another.

In a Parker spiral, footpoints of the interplanetary magnetic field are fixed points in the co-rotating frame. However, the photosphere is not static and shows various flow velocities, from small-scale to large-scale fluctuation. Large-scale flow fluctuations are due to axisymmetric flows such as meridional flows and differential rotation, and non-axisymmetric flows such as supergranular and giant cell flows. Small-scale flows such as granular flows are non-axisymmetric that have higher velocity (equal to solar rotation). Even though the footpoints of the interplanetary magnetic field lines are on the source surface, the open magnetic field flux tubes emerge from the boundaries of the supergranules. In the photosphere, these boundaries are displaced after supergranule cells decay and are reborn in a different location. The boundaries can also move due to other photospheric flows such as giant cells and meridional flows. Despite having large horizontal flow velocities, granule cells do not govern the interplanetary magnetic fields and instead, they are responsible for closed magnetic flux tubes that emerge from the boundaries of the granules.

In this study, we examine solar energetic electrons and protons transport in multiple meandering magnetic field models, ignore pitch angle scattering, thus staying within the regime of “scattering-free” transport. We assume SEPs to be test particles and directly solve the Lorentz equation.

In chapter 2, we first generate the Parker magnetic field and injected both solar energetic protons and electrons with initial kinetic energies of 1 to 100 MeV. We follow 1000 particles for 12 hours and obtain the same drift as Marsh et al. (2013). Next, we model the horizontal flow maps by using the granular flow velocity. The magnitude of the footpoint velocities are drawn from a random distribution V_θ and

$V_\phi \leq 2$ km/s. The interplanetary magnetic field lines are Parker-like with strong fluctuations that deviate from the Parker field model. Since this method generates the magnetic field numerically, a 3D spherical mesh is generated and we record the magnetic field on all nodes. The magnetic field inside a cell is obtained by linear interpolation of 8 vertices of the cells. Several 100 MeV protons are injected on the source surface. The particles are followed for days and they could not propagate without yielding significant propagation, staying source surface. We conclude that the fluctuations are too strong to allow the particles travel to 1 AU and beyond.

In chapter 3, we investigate the Giacalone (2001) model which was widely adopted for meandering interplanetary magnetic field modeling in previous studies. The meandering magnetic field is assumed to be an average Parker field plus a fluctuating field due to the supergranular flows in the photosphere. The fluctuating velocities are obtained from a stream function which is the sum of N modes of spherical harmonics, with a time-dependent amplitude and a random phase. Furthermore, the amplitude has a linear dependency on the rms speed of fluctuations, V_{rms} . In Giacalone (2001), $V_{rms} = 0.6$ km/s, however in later studies, Pei et al. (2006) and Kelly et al. (2012), higher V_{rms} such as 2.0 and 4.0 km/s were used.

The horizontal flow velocity maps of V_θ , V_ϕ and $V_g = \sqrt{V_\theta^2 + V_\phi^2}$ and the vector velocity map on the source surface are obtained for $V_{rms} = 0.6$ km/s. In Giacalone (2001) model, the source surface has higher flow velocities in the latitudinal direction. In the photosphere, there is not any mechanism except meridional flows and θ -component of supergranular flow to generate such large flow velocities.

Using Giacalone (2001) model, we obtain several meandering magnetic field lines originated in the the ecliptic plane, and solar energetic electrons trajectories injected in the ecliptic plane and footpoint trajectories on the source surface. The magnetic field lines meander and the deviation from the Parker field is significant. The electron trajectories show strong angular displacement from the starting point.

We then investigate the solar energetic electron path length distributions in Parker field and the meandering field. The path length of the Parker magnetic field line and the path length distribution of ten thousand 100 MeV electrons with random initial pitch angle in the Parker magnetic field with various solar wind speed, 350 km/s to 800km/s, are obtained. In the case of Parker field, the path length distributions of the solar energetic electrons are clearly different from the field. Next, we examine the path length distribution of the electrons in the meandering field. First, we compare the path length distribution of 100 MeV electrons and protons for the case of $V_{rms} = 0.6$ km/s. Although electrons and protons are different in their drift speed and gyro-radii, the path length distributions are almost identical for $V_{rms} = 0.3$ to 2.5 km/s at radial distances $R = 0.2$ to 1 AU. Next, we examine the variation of path length distributions w.r.t. energy. The path length distribution of 10000 electrons with initial kinetic energies, 1, 10 and 100 MeV shows weak dependence on the initial kinetic energy.

We compare the path length distribution of 10000 magnetic field lines and 10000 solar energetic electrons for various rms speed of fluctuation, $V_{rms} = 0.3, 0.6, 1.0, 1.5, 2.0, 2.5$ km/s, for various distances from the Sun, $R = 0.2, 0.5, 1.0, 2.0$ and 3.0 AU. Our conclusions about the electrons path length distributions as follows:

1. The current hypothesis in understanding the propagation of energetic electrons in the solar wind is to assume that electrons are tied to the IMF. Consequently, the particle path length should be very similar to that of the magnetic field line path length. However, our simulations clearly show that the path length distributions of the fields and electrons are different. In particular, standard deviations can differ significantly. While the path length distributions for the field and electrons are different, the path length distributions for electrons of different energies are almost identical.

2. Depending on the heliocentric distance R and the value of V_{rms} , the path length distributions of electrons and magnetic field lines sometimes can be approximated by a Gaussian distribution. In particular, at 1 AU, a Gaussian distribution describes well both the field line path length and the electron path length. The mean and standard deviation increase with V_{rms} . Our results for the electron path length distribution at $R < 1$ AU can be useful in understanding future Solar Probe Plus observations. We note that for smaller R , the “scatter-free” approximation is more accurate.

3. By comparing the mean and the standard deviation of the electron path length distributions from our simulation to that from observations Zhao et al. (2019), we suggest that the upper limit of V_{rms} is ~ 1.0 km/s. Higher values as 4 km/s or larger as discussed in Pei et al. (2006) will lead to very large electron path length, inconsistent with observations by Zhao et al. (2019). Note that the presence of scattering will lead to even larger path length. Therefore, our upper limit of V_{rms} of ~ 1.0 km/s is likely conservative. In a future work, we will investigate how including pitch angle scattering will affect the path length distribution.

In chapter 4, we use a more realistic photospheric velocity spectrum to generate meandering magnetic field lines. The model is adapted from Hathaway 2016 (private communication). The magnetic field lines are Parker-like, however, the fluctuations are quite strong locally. The drifts cause the protons to jump to adjacent field lines immediately and the new field line can be in a totally different direction which in turn leads to multiple reversals of the solar energetic particles trajectories. In our simulation, it seems that in this model, solar energetic particles are trapped between the Sun and 3 AU. In conclusion, the trajectory of the particles shows that these fluctuation velocities are too high and can be ruled out by observations.

In chapter 5, we study the expansion of magnetic flux tubes from the photosphere to the source surface at $10R_{sun}$. We follow two different scenarios to obtain the source surface map. Open magnetic flux tubes expand into the interplanetary space. They concentrate near the boundaries of the supergranules.

In section 5.1, the boundaries of supergranules are extracted from the photospheric flow velocity maps. The maximum flow velocities on the boundaries of the supergranules are obtained, $V_{limit} = 40.0$ m/s. The maps and the open magnetic flux tubes are projected to the source surface at 10 solar radii, using the Kriging method. The footpoints' motion on the source surface is plotted. The interplanetary magnetic field lines are Parker-like and closer to Parker than magnetic field lines generated by Hathaway's flow velocity spectrum, with smaller fluctuations. The trajectories of several 100 MeV protons in the meandering magnetic field are compared to the trajectory of the same protons in the Parker field. The trajectories in the Parker

field and the meandering field are similar. However, they can be clearly discerned on smaller scales.

In section 5.2, a new method is introduced to simulate the random walk of the footpoints on the source surface. First, the distribution of the footpoints within supergranule boundaries is obtained. In every time step, the magnitude of all footpoint velocities on the source surface are chosen from the same distribution. In addition, the direction of the footpoint velocities are decided by the following procedure: in the first step, we choose a random direction, then in each step, the velocity vector deviates from the previous time by a small angle that is drawn from a normal distribution. The standard deviation of the distribution is a free parameter that decides how the footpoints move on the source surface. Five distributions with $\sigma = 0.010, 0.025, 0.050, 0.075$ and 0.100 radian are examined and the motion of the footpoints and meandering interplanetary magnetic field lines are investigated. In a future study, we will investigate the trajectory of the solar energetic particles in the proposed model. A comparison of the path length distributions at 1 AU to the observation can lead to a better understanding of the source surface of the interplanetary magnetic field. Finally, we compare all three models introduced in Chapter 4, Section 5.1 and Section 5.2.

In conclusion, in all four models, as discussed in chapters 3, 4 and 5, we find that the footpoint's fluctuating velocity on the source surface can not be large and is most likely ≤ 300 m/s. Consequently, the interplanetary magnetic field is also Parker-like and the field lines stay close to the initial Parker field lines. Even though the magnetic field is close to a Parker field, the SEP trajectories show strong deviations

from the Parker field. Comparing path length distributions of the energetic particles and field lines clearly proves that solar energetic particles are not tied to the field lines and often jump to adjacent field lines.

REFERENCES

- (2009). Heliophysics: Plasma physics of the local cosmos.
- Beck, J. G., Duvall, T. L., J., Scherrer, P. H., and Hocksema, J. T. (1998). The Detection of Giant Velocity Cells on the Sun. In Korzennik, S., editor, *Structure and Dynamics of the Interior of the Sun and Sun-like Stars*, volume 418 of *ESA Special Publication*, page 725.
- Beckers, J. M. and Morrison, R. A. (1970). The Interpretation of Velocity Filtergrams. III: Velocities Inside Solar Granules. *Solar Physics*, 14(2):280–293.
- Bumba, V. and Howard, R. (1965). Large-Scale Distribution of Solar Magnetic Fields. *ApJ*, 141:1502.
- Cane, H. V., McGuire, R. E., and von Rosenvinge, T. T. (1986). Two Classes of Solar Energetic Particle Events Associated with Impulsive and Long-Duration Soft X-Ray Flares. *ApJ*, 301:448.
- Chabert, P., Arancibia Monreal, J., Bredin, J., Popelier, L., Aanesland, A., Lafleur, T., Takahashi, K., Charles, C., Boswell, R. W., Böhm, C., Perrin, J., Aanesland, A., Meige, A., Chabert, P., Mikellides, I. G., Goebel, D. M., Snyder, J. S., Katz, I., Herman, D. a., Wang, C. C., Roy, S., Takahashi, K., Charles, C., Boswell, R. W., Kaneko, T., Hatakeyama, R., Lejeune, A., Bourgeois, G., Mazouffre, S., Glass, F., Howard, J., Blackwell, B., Fruchtman, A., Charles, C., Yasaka, Y., Fukuyama, A., Hatta, A., Itatani, R., Boeuf, J. P., Garrigues, L., Mikellides, I. G., Katz, I., Goebel, D. M., Polk, J. E., Jameson, K. K., Blackwell, D. D., Walker, D. N., Messer, S. J., Amatucci, W. E., Takao, Y., Kataharada, H., Miyamoto, T., Masui, H., Yamamoto, N., Nakashima, H., Tsuji, A., Yasaka, Y., Takeno, H., Plasma, A., Co, T., and Wirz, R. (2009). Discharge Plasma Processes of Ring-Cusp Ion Thrusters. *California Institute of Technology*, 14(7):2652–2658.
- Dalla, S., Marsh, M. S., Kelly, J., and Laitinen, T. (2013). Solar energetic particle drifts in the Parker spiral. *Journal of Geophysical Research (Space Physics)*, 118(10):5979–5985.
- Fisk, L. A. and Jokipii, J. R. (1999). Mechanisms for latitudinal transport of energetic particles in the heliosphere. *Space Science Reviews*, 89:115–124.
- Forsyth, R. J., Balogh, A., Smith, E. J., Erdös, G., and McComas, D. J. (1996). The underlying parker spiral structure in the ulysses magnetic field observations, 1990–1994. *Journal of Geophysical Research: Space Physics*, 101(A1):395–403.
- Giacalone, J. (2001). The latitudinal transport of energetic particles associated with corotating interaction regions. *J. Geophys. Res.*, 106(A8):15881–15888.

- Gizon, L. and Duvall, T. L. (2004). Solar-cycle variations in the spectrum of supergranulation. In Stepanov, A. V., Benevolenskaya, E. E., and Kosovichev, A. G., editors, *Multi-Wavelength Investigations of Solar Activity*, volume 223 of *IAU Symposium*, pages 41–44.
- Gombosi, T. I. (2004). *Physics of the Space Environment*.
- Hathaway, D. H. (1987). Spherical Harmonic Analysis of Steady Photospheric Flows. *Solar Physics*, 108(1):1–20.
- Hathaway, D. H. (1988). Simulating Photospheric Doppler Velocity Fields. *Solar Physics*, 117(2):329–341.
- Hathaway, D. H. (1992). Spherical Harmonic Analysis of Steady Photospheric Flows - Part Two. *Solar Physics*, 137(1):15–32.
- Hathaway, D. H. (2012). Supergranules as Probes of Solar Convection Zone Dynamics. *ApJ*, 749(1):L13.
- Hathaway, D. H., Beck, J. G., Bogart, R. S., Bachmann, K. T., Khatri, G., Betitto, J. M., Han, S., and Raymond, J. (2000). The Photospheric Convection Spectrum. In *AAS/Solar Physics Division Meeting #31*, volume 31 of *AAS/Solar Physics Division Meeting*, page 05.04.
- Hathaway, D. H., Beck, J. G., Han, S., and Raymond, J. (2002). Radial Flows in Supergranules. *Solar Physics*, 205(1):25–38.
- Hathaway, D. H., Teil, T., Norton, A. A., and Kitiashvili, I. (2015). THE SUN'S PHOTOSPHERIC CONVECTION SPECTRUM. *The Astrophysical Journal*, 811(2):105.
- Hathaway, D. H., Williams, P. E., Dela Rosa, K., and Cuntz, M. (2010). The Advection of Supergranules by the Sun's Axisymmetric Flows. *ApJ*, 725(1):1082–1090.
- Jokipii, J. R., Kóta, J., Giacalone, J., Horbury, T. S., and Smith, E. J. (1995). Interpretation and consequences of large-scale magnetic variances observed at high heliographic latitude. *Geophysical Research Letters*, 22(23):3385–3388.
- Jokipii, J. R. and Parker, E. N. (1968). Random Walk of Magnetic Lines of Force in Astrophysics. *Physical Review Letters*, 21(1):44–47.
- Judge, P. (2006). Observations of the Solar Chromosphere. In Leibacher, J., Stein, R. F., and Uitenbroek, H., editors, *Solar MHD Theory and Observations: A High Spatial Resolution Perspective*, volume 354 of *Astronomical Society of the Pacific Conference Series*, page 259.
- Kallenrode, M.-B. (1998). *Space Physics*.

- Kelly, J., Dalla, S., and Laitinen, T. (2012). CROSS-FIELD TRANSPORT OF SOLAR ENERGETIC PARTICLES IN a LARGE-SCALE FLUCTUATING MAGNETIC FIELD. *The Astrophysical Journal*, 750(1):47.
- Li, B., Cairns, I., Gosling, J. T., Lobzin, V., Steward, G., Neudegg, D., and Owens, M. (2016). Mapping Magnetic Field Lines between the Sun and Earth. In *41st COSPAR Scientific Assembly*, volume 41, pages D2.2–10–16.
- Marsh, M. S., Dalla, S., Kelly, J., and Laitinen, T. (2013). Drift-induced Perpendicular Transport of Solar Energetic Particles. *ApJ*, 774(1):4.
- Parker, E. N. (1958). Dynamics of the Interplanetary Gas and Magnetic Fields. *ApJ*, 128:664.
- Pei, C., Jokipii, J. R., and Giacalone, J. (2006). Effect of a random magnetic field on the onset times of solar particle events. *The Astrophysical Journal*, 641(2):1222–1226.
- Rieutord, M. and Rincon, F. (2010). The sun’s supergranulation. *Living Reviews in Solar Physics*, 7(1):2.
- Rincon, F. and Rieutord, M. (2018). The sun’s supergranulation. *Living Reviews in Solar Physics*, 15(1):6.
- Shapiro, S. S. and Wilk, M. B. (1965). An analysis of variance test for normality (complete samples). *Biometrika*, 52(3/4):591–611.
- Title, A. M., Tarbell, T. D., Simon, G. W., Acton, L., Duncan, D., Ferguson, S., Finch, M., Frank, Z., Kelly, G., Lindgren, R., Morrill, M., Pope, T., Reeves, R., Rehse, R., Shine, R., Topka, K., Harvey, J., Leibacher, J., Livingston, W., and November, L. (1986). White-light movies of the solar photosphere from the soup instrument on spacelab 2. *Advances in Space Research*, 6(8):253–262.
- Wang, H. (1989). Do mesogranules exist? *Solar Physics*, 123(1):21–32.
- Wang, L., Lin, R. P., Li, G., and Krucker, S. (2006). A Study of Pitch Angle Distributions for Six Solar Impulsive Electron Events. In *AGU Fall Meeting Abstracts*, volume 2006, pages SH43B–1530.
- Williams, C. K. I. (1997). Prediction with gaussian processes: From linear regression to linear prediction and beyond. In *Learning and Inference in Graphical Models*, pages 599–621. Kluwer.
- Xu, F., Li, G., Zhao, L., Zhang, Y., Khabarova, O., Miao, B., and le Roux, J. (2015). ANGULAR DISTRIBUTION OF SOLAR WIND MAGNETIC FIELD VECTOR AT 1 AU. *The Astrophysical Journal*, 801(1):58.
- Zhao, L., Li, G., Zhang, M., Wang, L., Moradi, A., and Effenberger, F. (2019). Statistical analysis of interplanetary magnetic field path lengths from solar energetic electron events observed by WIND. *The Astrophysical Journal*, 878(2):107.